Understanding the Plasma and Improving Extraction of the ISIS Penning H^- Ion Source

Scott Robert Lawrie

Trinity College

University of Oxford

A thesis submitted for the degree of

Doctor of Philosophy

Trinity Term, 2017

Abstract

A Penning-type surface-plasma negative hydrogen (H^-) ion source has been delivering beam at the ISIS pulsed spallation neutron and muon facility for over thirty years. It is one of the most powerful and well-renowned H^- sources in the world. Although long-term experience has allowed the source to be operated reliably and set up in a repeatable way, it is treated as something of a 'black box': the detailed plasma physics of *why* it works has always been unclear.

A vacuum Vessel for Extraction and Source Plasma Analyses (VESPA) has been developed to understand the ISIS ion source plasma and improve the beam extracted from it. The VESPA ion source is operated in a completely new regime whereby the analysing sector dipole magnet housed inside a refrigerated 'cold box', presently used on ISIS, is replaced by an on-axis extraction system. The new extraction system incorporates a novel einzel lens with an elliptical aperture. This is the first demonstration of an elliptical einzel being used to focus an asymmetric H^- ion beam.

With the dipole magnet removed, the ion source has been shown to produce 85 mA of H^- beam current at normal settings; of which 80 mA is transported through the new einzel lens system, with a normalised RMS emittance of 0.2 π mm mrad. Optical emission spectroscopy measurements have shown a plasma density of 10^{19} m^{-3}, an H_2 dissociation rate of 70%, an almost constant electron temperature of 3.5 eV and an atomic temperature which linearly increases above the electron temperature.

In support of these principal measurements, rigorous particle tracking, electrostatic and thermal simulations were performed. In addition, a suite of new equipment was manufactured by the author. This includes a fast pressure gauge, a temperature controller, a high voltage einzel lens circuit, a fast beam chopper and a caesium detection system.

Acknowledgements

There are many people who have contributed to my successful completion of this thesis. Firstly, I would like to thank my supervisor Dan Faircloth, whose boundless enthusiasm and interest are excellent motivators to do good work. We'd spend many hours discussing every detailed nuance of the fabulously complicated and famously fickle beasts known as ion sources. Trying to come up with reasons why the thing was (or wasn't!) behaving as it should was great fun and we'd leave whiteboards covered in our musings. Dan is also my line-manager at the Rutherford Appleton Lab (RAL), and has given great career and management advice throughout the many years we have worked together. He has opened many doors for me, including arranging this joint RAL-Oxford DPhil project and I wouldn't be anywhere near my current level without Dan, so eternal thanks to you.

Due to my somewhat abnormal route into this DPhil, I also had Alan Letchford (at RAL) and Andrei Seryi (in Oxford) as co-supervisors, who contributed significantly and guided me admirably throughout. Alan is a world-class expert in linacs and ion sources, who is always the one with probing, insightful questions and ideas on any subject. His ability to cut straight to the heart of the problem is nothing short of brilliant. Similarly, Andrei is a man of many talents who has worked on several different accelerator projects, so has the important ability to make one think outside the box. Thanks to you both for all of your assistance and expertise.

My friends and colleagues at RAL are too numerous to name in full, so my heartfelt thanks go to a select few. My technicians, Mark Whitehead and Trevor Wood were always on hand to build, fix and test things. They also gave expert practical advice from the point of view of real accelerator operators, ensuring I didn't have delusions of grandeur. Mike Perkins and John MacGregor were invaluable in the build of the VESPA, particularly the high voltage and timing equipment, without whom the project would never even have left the ground. John Thomason and Ben

Pine gave invaluable advice on how to complete this thesis – how John found the time to cast his eagle eyes over it I don't know, but I am so thankful he did! Providing the substantial equipment budget was extremely generous, too, thank you.

My parents, sisters and in-laws have always been a great source of comfort and support. Although they didn't always understand what magic I was performing at RAL, they always believed in me and encouraged great things. I hope this makes them proud. Equally, my late grandfather Robert and his best friend Gordon were my original inspiration for a career in physics. My thoughts are with you.

Finally and most importantly, I would like to thank my wife Sam and my daughters Addison and Beatrice. My three beautiful girls are the reason I wake in the morning and strive to do important things such as this. Hearing Addison talk about VESPA and telling me to be careful not to get zapped lights up my heart. And Sam: you're so patient, kind and loving. I owe everything to you. I love you.

Contents

List of Figures

List of Tables

Chapter 1

Introduction

Particle accelerators were initially developed as tools to study nuclear and particle physics. To explore higher energy physics processes, ever larger machines were built in order to accelerate and collide electrons, protons and heavy ions closer to the speed of light. The very first accelerators used high voltage electrostatic acceleration, but the scale and difficulty handling extremely high voltages led to the development of radio-frequency (RF) accelerating cavities. Magnetic fields in the form of cyclotron accelerators were introduced to re-circulate the particles back to the RF accelerating field and hence use the same cavity to add more and more energy. Tapering the cyclotron magnet poles allowed for weak beam focussing, however the large steel yokes in cyclotrons became impractically heavy at high energies and relativistic effects became difficult to deal with. Therefore new accelerators in the form of the isochronous cyclotron, the synchrocyclotron and eventually the synchrotron took over. Quadrupole and other higher order multipole magnets were developed to focus the particle beams strongly and add subtle effects such as chromaticity correction. Superconducting materials were introduced to achieve higher magnetic fields and higher Q-factor RF cavities than traditional steel and copper magnets and cavities could produce. Ever more advanced technology is continuing to be developed to increase the power and efficiency of particle accelerators, as well as make them more compact and reliable [1].

Accelerators can now be made compact and inexpensive enough to operate in hospitals for cancer therapy; shipping ports for cargo scanning; even waste processing plants for the decomposition of pollutants. Large materials science facilities using accelerator-produced neutron or x-ray beams are heavily sought after to study and develop new material technologies such as touch-screen displays, batteries and photovoltaic cells. In fact over 24,000 accelerators are in operation world-wide, of which only a handful are pursuing the highest energies for sub-atomic physics research [2].

No matter what scale, cost or technology is involved, though, the one thing that unites all accelerators is the *particle source*. This is the component at the very start of an accelerator from which the particle beam originates; its performance has a very strong influence on the performance of the entire accelerator complex. The work in this thesis describes methods to modernise one particular variety of particle source called a Penning-type surface-plasma negative hydrogen (H^-) ion source.

H^- ion sources are important for modern high power hadron accelerators. Creating a beam of negatively charged particles and converting them into positive charges at injection can improve total luminosity. This *charge exchange* injection can also be used to double the beam energy of an electrostatic accelerator or to inject a high power neutral beam into modern inertial confinement fusion reactors. Although solving many problems in high power machines, H^- ion sources are themselves very difficult both to understand theoretically and to construct and operate. Therefore H^- ion source research and development is still a very active field.

The chapters in this thesis are laid out in the following way. Chapter 2 explains in detail why H^- ions are needed at a wide variety of facilities, before Chapter 3 details the various ways they are produced, both theoretically and in practice. A new research and development tool called the Vessel for Extraction and Source Plasma Analyses (VESPA), on which the work described in this thesis has been performed, is then introduced in Chapter 4. Using the VESPA, the first detailed optical spectroscopy measurements of a Penning ion source plasma are presented in Chapter 5. The plasma parameters calculated from the spectroscopy results helped inform and improve high accuracy particle tracking simulations in Chapter 6, which also details the electrostatic and thermal simulations needed to inform the design and implementation of a novel, compact beam extraction and chopping system. Chapter 7 describes the beam measurements made on both the baseline and newly designed extraction systems. Chapter 8 discusses the implications of removing the caesium trap and the possible effects this has to long-term operation, before conclusions of the overall work are drawn in Chapter 9.

Work published previously by the author forms the basis of this thesis. The VESPA was introduced in [3, 4, 5]. Preliminary optical spectroscopy and beam measurements were published in [6, 7]. Detailed beam extraction measurements and long-term implications have not been published prior to this thesis.

Chapter 2

Applications of H^- Beams

2.1 Tandem Accelerators

One of the oldest and simplest accelerators, the tandem uses electrostatic fields to accelerate negative ions up to a large positive *terminal* voltage. At the terminal, the electrons are stripped using a foil, leaving positive ions. The positive ions are then repelled by the terminal volts and re-accelerated back to the laboratory ground potential. By using negative ions in this manner, the final beam energy is equal to twice the terminal voltage and can be easily injected into the next part of the accelerator at ground potential. Although old technology, tandems are still in widespread use world-wide, particularly in low energy nuclear and condensed matter physics experiments where the 'Pelletron' is the most widely distributed commercial variant [8]. In addition, Siemens are developing an extremely compact tandem accelerator for medical radioisotope production, which uses a negative hydrogen (H^-) ion source [9]. The schematic operation of tandems and other accelerators which use H^- ions is shown in Fig. 2.1.

2.2 Neutral Beams for Fusion

Modern neutral beam injectors for magnetic confinement *tokamak* fusion devices use H^- ions. Large beams of high power neutral atoms are needed to heat the plasma in the centre of the reactor, as well as to inject the fuel, such as deuterium. The injected beam must be uncharged so it can penetrate the strong plasma confinement magnetic fields. An initially charged particle beam with a current of several tens of Ampères is accelerated to MeV-level energies and then neutralised. In older facilities, such as the Joint European Torus (JET), several medium-current proton sources are combined to create a broad 90 keV proton or 125 keV deuterium beam. Future applications,

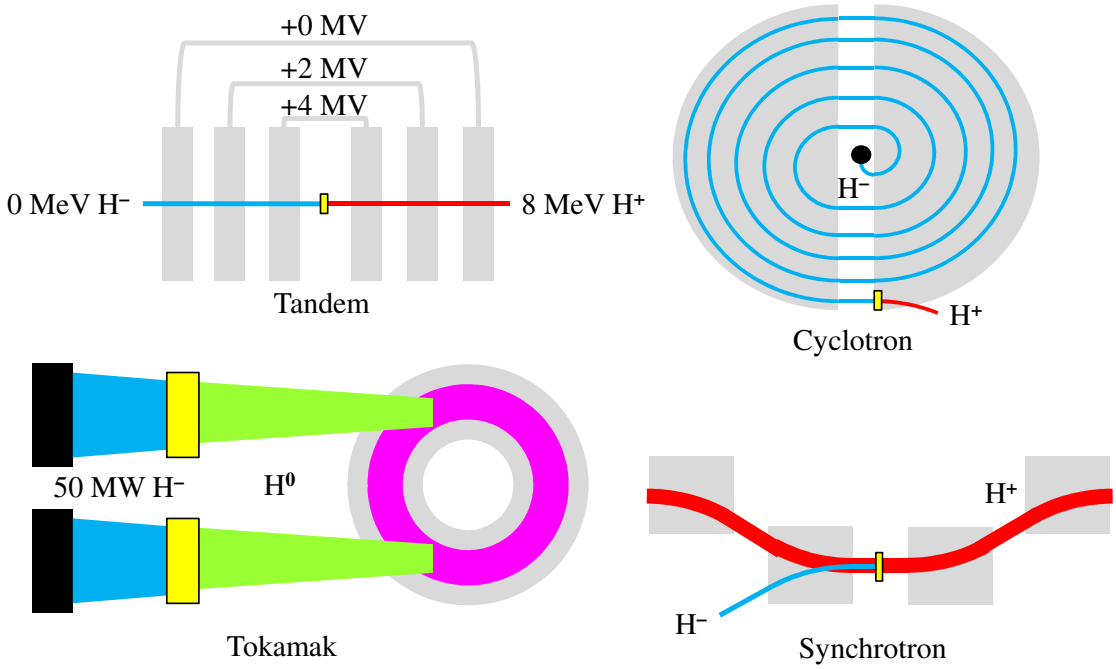

Figure 2.1: Principle uses of H^- ions. In all cases, a negative ion beam (blue) passes through a foil, laser or gas stripper (yellow) to remove one or more electrons.

such as the International Thermonuclear Experimental Reactor (ITER), will have greater neutral beam heating requirements. ITER will use several neutral beams, each with over 16 MW of power, to heat the plasma. In addition to having a higher current, the neutral beam energy will be increased ten-fold in ITER to 1 MeV such that the beam can penetrate deeply into the tokamak plasma. The cross section for a proton to capture an electron (thus forming a neutral atom) decreases with proton energy, so a 1 MeV proton injector on ITER is inefficient. On the other hand, the second electron on an H^- ion is easily removed and the ionisation cross section is fairly energy-independent. Therefore, high power neutral beam injectors for future fusion applications invariably use H^- beams to achieve an order of magnitude higher heating power than older proton sources [10].

2.3 High Power Proton Drivers

Many modern proton accelerator facilities utilise charge exchange to facilitate easier injection or extraction of the beam. This involves the injection of H^- ions, which are converted to protons using an electron-stripping foil.

2.3.1 Cyclotrons

Cyclotrons inject and accelerate H^- ions, then when the beam has reached its maximum orbital radius, a carefully positioned foil removes the two electrons. The bare proton is deflected in the opposite sense to the H^- in the fixed magnetic field and is thus deflected out of the final orbit, for clean, low loss extraction from the cyclotron.

2.3.2 Synchrotrons and Accumulator Rings

Synchrotrons and accumulator rings convert H^- ions to protons immediately on injection either inside a dipole magnet or, more commonly, between two 'bump' dipoles. This process enables Liouville's particle volume density conservation law to be circumvented [11] as it is no longer a time-reversible process due to the particle nature changing. The emittance of the injected and accumulated beams is conserved[1], meaning a large number of turns of injected beam can be accumulated without the beam expanding beyond the acceptance of the ring. If protons were injected instead, Louville's theorem would require the emittance to grow, meaning only a few turns could be injected, depending on the machine acceptance. As a by-product, injection itself is made simpler using this method as there is no need for a pulsed or reversible injection magnet as the injected H^- and circulating protons are deflected in opposite directions in the magnet, thus they naturally converge on the nominal orbit. Typically, the orbit is 'bumped' out to the stripping foil during injection so the accumulated (and, in the case of a synchrotron, accelerated) proton beam avoids the foil, reducing overall heat load. The orbital bump also allows 'painting' of the injected H^- beam over a distributed area on the foil, reducing localised hot spots on the foil.

Charge exchange injection is not trivial due to the difficulties handling micron-thickness stripping foils, pulsing bump magnets and creating the H^- ion beam itself. However the trouble is worth it due to the possibility of a large[2] number of injected turns of beam which can be accumulated in the ring. More turns at injection means a higher number of stored particles, or a higher circulating current. If one thinks of an accelerator as a simple electrical system with power $P = IV$, then a high power[3] can be achieved by delivering a higher current I, which is typically considerably less expensive than building a larger accelerator to achieve a higher beam energy, or voltage V. As the name suggests, high power proton drivers (HPPDs) require high

[1] Apart from a small increase due to scattering on the foil
[2] hundreds or even thousands
[3] in the megawatt range

power proton beams to drive the system that follows. There are various uses for HPPDs:

Proton Colliders: H^- injection into an HPPD is preferred as it results in a higher number of particles available per collision at the interaction point. CERN are building the (H^-) Linac4 [12] to replace the (proton) Linac2 to increase the luminosity of the large hadron collider (LHC).

Future Particle Physics Experiments: Muon colliders or high power directed neutrino beams (themselves generated from a circulating muon beam) may be used in higher energy particle physics experiments [13]. High fluxes of muons will be created at a dedicated high power target connected to an HPPD.

Spallation Neutron Sources: Neutrons can be used in fundamental materials investigations, driven from HPPDs at much lower energy than in colliders. The data capture rate is directly proportional to available neutron flux; in turn proportional to the available proton power on the spallation target.

2.4 Neutron Facilities

Neutrons inbound on a sample material may diffract off its component atoms. Depending on the sample preparation, the atomic and micro-structure of a wide range of materials can be investigated using neutron diffraction, spectrometry, reflectometry and imaging. Example materials studies are:

- Crystal lattices; for example metal alloys or solid catalysts
- Amorphous solids; for example liquid crystals or glasses
- Collections of individual molecules; for example proteins or surfactants
- Interfaces; for example boundary interactions between a gas and a liquid

Either x-rays or neutrons can be used to perform these kinds of diffraction experiments. However neutrons have three major advantages over x-rays. Firstly, neutrons are more penetrating than x-rays because they interact with the nucleus, not the electron orbitals. This means large, thick bodies, such as solid metal girders, can be probed to large depths. This is as opposed to x-rays which can only penetrate a few millimetres into metals, dependent on their energy.

Secondly, since neutrons scatter off the nucleus, the nuclear scattering cross section is important to take into account. The cross section varies significantly for different elements and even the isotopes of each element, which enables isotopic selection of materials under study. This is as opposed to x-ray diffraction which depends on the cross section for scattering off the atomic electrons. Hence x-ray diffraction is more effective for heavier elements with many electrons. Trying to study light elements such as hydrogen — or materials with significant hydrogen fractions, such as water and most large organic molecules — requires very high x-ray fluxes to give a good signal to noise ratio. These large fluxes usually destroy the organic molecule under test, so it must be continually replaced. On the other hand, neutron diffraction off hydrogen is very effective, so investigations on organic molecules can be performed with many orders of magnitude smaller neutron fluxes, thus preserving the sample material. Thirdly, neutrons carry a magnetic moment (i.e. a nuclear spin). Therefore neutrons can be used to investigate the magnetic properties of materials, such as superconductors, which x-rays cannot readily distinguish.

It is clear that neutrons are valuable tools in the investigation of matter for economic, societal and, indeed, pure scientific knowledge [14]. However, creating a neutron beam is far from trivial. As an example, an electron beam is very easy to generate: a heated filament held at a few volts creates copious electrons in a small area with a low emittance. Proton beams are also reasonably straightforward to create, simply requiring the ionisation of hydrogen gas in a plasma at a few tens or hundreds of volts. However neutrons can only be extracted from an atomic nucleus, which requires many millions of electron-volts to break apart. Therefore powerful neutron sources are almost by definition housed in large, nuclear-licensed facilities.

2.4.1 Reactor Sources

Nuclear reactors are the most straightforward method of creating neutron beams. Uranium-235 occasionally undergoes a spontaneous fission reaction; from which daughter nuclei are released, along with two or three neutrons. The daughter nuclei have ample kinetic energy to generate heat in the reactor, which can be used for power via a heat exchanger; whilst the neutrons go on to induce more fission reactions in other nuclei. The neutron flux is carefully moderated from an average of 2.5 neutrons per reaction to precisely one; thus preventing a runaway chain reaction.

Some reactors are used for research rather than power generation, whereby the fission neutrons are allowed to escape and be used for a variety of purposes, whereas the heat from the daughter nuclei is an un-wanted waste product. Although high fluxes of neutrons are available from reactors [15, 16], they do not have a time structure, which may be useful in some neutron studies. The process also comes with the perceived risks involved with all fission reactors. Reactor sources are generally rather old and more are reaching the end of their lives than are being built [17].

2.4.2 Spallation Sources

Spallation neutron sources use similar nuclear processes involved in reactors to generate neutrons, but the 'fuel' can be any heavy element[4], which need not be fissile. A high energy proton beam impacting a heavy metal *target*[5] can cause the target nuclei to break apart and release neutrons in a process called *spallation*. Spallation neutrons can be used to breed fissile uranium-233 from fertile thorium-232 in an Accelerator-Driven Sub-critical Reactor (ADSR), whereby criticality accidents can never happen since the process ceases if ever the accelerator fails [18]. Besides nuclear power generation, spallation neutrons can be used directly for materials studies already discussed. The benefit of accelerator-driven neutron sources is that the neutron flux can be pulsed, with a well defined temporal structure, depending on the type of particle accelerator used. A short-pulse neutron source is advantageous when time-resolved or high Q-range measurements are required. Such an example is the ISIS facility.

2.5 The ISIS Spallation Neutron and Muon Source

The ISIS pulsed spallation neutron and muon source, based at the Rutherford Appleton Laboratory (RAL) in the UK, was the first high power, short-pulse accelerator-driven spallation neutron source ever built. Having been producing neutrons since 1984, it has built up considerable expertise in neutron target and instrument design, as well as how to operate an accelerator-based user facility reliably. Even now, it is still one of only a few spallation neutron facilities in the world and is the only one with two neutron target stations. The layout of ISIS is shown in Fig. 2.2.

[4]The heavier the element, the more neutrons are available per atom

[5]Typically lead-bismuth, tungsten or mercury

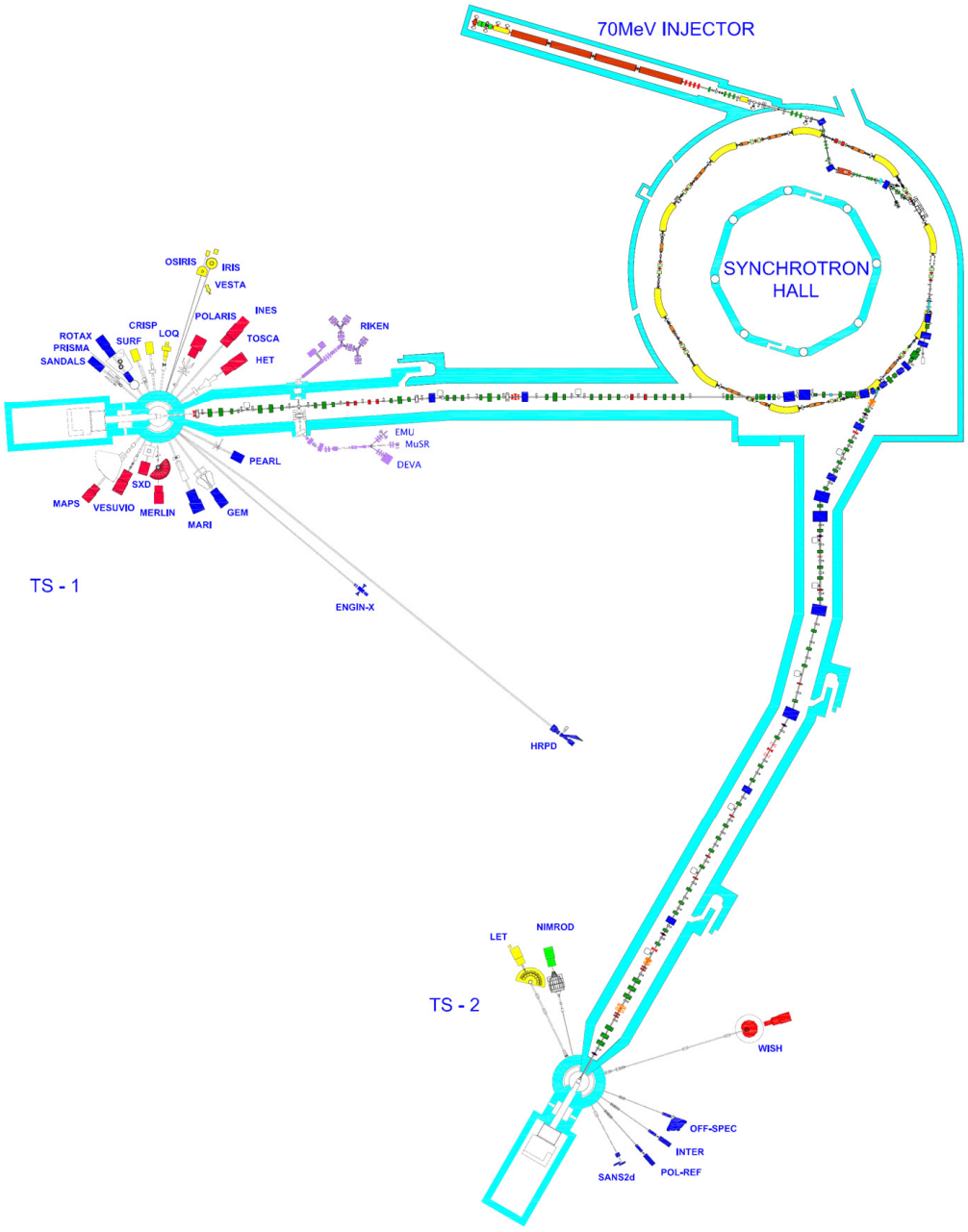

Figure 2.2: The ISIS pulsed spallation neutron and muon facility.

2.5.1 Neutron Target Stations

ISIS uses solid tungsten metal targets. Through years of operational experience, it has been shown that the correct material choice is important not only for neutron production, but also for reliable long-term operation. For example, ISIS originally used a uranium target due to its high neutron yield, but the mechanically brittle uranium could not endure the thermal shock of prolonged periods of pulsed beam operation, so had to be replaced regularly. Next a pure tungsten target was used as it is more mechanically robust. However the radioactive fission products from tungsten reacted badly with cooling water so the target has evolved into the tantalum-clad tungsten brick used today, since tantalum is more inert and safe next to water.

The original target station (TS1) was designed to house a uranium target so needed high levels of shielding. Also, being the first neutron source of its type, and designed before the era of high precision computer-aided design (CAD), the mechanical layout was designed to ensure the principle worked, rather than being optimal. With the experience from operating TS1 and the modern CAD and simulation software available, a second target station (TS2) was designed for much more optimal and efficient neutron production: TS2 takes less proton beam power than TS1, but has a higher relative neutron flux[6]. Therefore the science output is very competitive to other facilities, despite being an order of magnitude lower in beam power. The two target stations are fed by the same proton synchrotron.

2.5.2 Synchrotron

A rapid-cycling proton synchrotron (RCS) is used at ISIS to accelerate a 70 MeV injected beam to 800 MeV. The synchrotron operates at 50 Hz; meaning the entire process of creating beam, injecting it into the RCS, accelerating up to final energy, kicking out of the ring to the targets, and recording neutron diffraction data in the instruments happens 50 times every second. This is a very fast cycle, which means that although the final beam energy is not as high as, for example, the LHC, creating accelerator components which can all operate together reliably for decades at such high duty cycles and powers is impressive.

The RCS is a 163 m circumference, ten super-period ring with ten swept-frequency radio-frequency (RF) accelerating cavities operating in the low MHz range. A *White*

[6]Around six times higher neutron intensity per pulse.

Circuit[7] is used as an energy-recovery system to ramp the dipoles up and down efficiently by transferring energy back and forth between the dipoles and parallel inductors ('chokes') and capacitors [20]. Septum and fast kicker magnets are used to inject the beam and extract to the two target stations. TS1 operates at 40 Hz and TS2 at 10 Hz. To achieve this, for every five proton pulses produced by the RCS, four are directed to TS1 and one goes to TS2. With an average circulating current of 220 μA and an energy of 800 MeV, the proton beam has a power of 176 kW. When TS2 came online in 2008, it would have taken 20% of the beam power away from TS1. To ensure the same level of neutron science is possible from TS1, the total RCS beam power therefore had to be increased by 20%. This required the installation of four 'second harmonic' RF cavities in the ring to increase the area in longitudinal phase space available to store beam. At the same time, more current needed to be delivered to the synchrotron by the injector, placing higher demand on the H^- ion source.

2.5.3 Injector

Beam is delivered to the RCS by a 70 MeV H^- linear accelerator (linac). The main accelerating portion of the linac consists of four 12 metre-long normal-conducting drift-tube linac (DTL) *tanks* operating at 202.5 MHz. Tank1 accelerates a 665 keV beam to 10 MeV and the following three tanks each add 20 MeV, for a total of 70 MeV. When ISIS was originally constructed, a Cockcroft-Walton voltage multiplier stack was used to accelerate the 665 keV beam which fed the linac. Before TS2 was constructed, the Cockcroft-Walton was replaced with a modern, reliable, efficient *low energy beam transport* (LEBT) and *radio-frequency quadrupole* (RFQ). The LEBT delivers a 35 keV H^- beam to the RFQ, which accelerates it to 665 keV; focusses it under the influence of strong space-charge forces, and longitudinally bunches an initially constant-current beam pulse such that it can be inserted into the RF phase structure of Tank1. Along with the RFQ and second-harmonic RCS cavity installations, a program of ion source R&D was undertaken to meet the requirements of higher total beam power for TS2 operation. Future ISIS upgrades require an even better performance from the ion source, which is the subject of this thesis. However, before discussing the details of the ISIS H^- ion source, the next chapter will outline the general characteristics and operational principles of all H^- ion sources.

[7] named after its inventor, M. G. White [19].

Chapter 3

H^- Production

3.1 Basic Plasma Properties

A plasma is sometimes referred to as the 'fourth state of matter'. Although solids, liquids and gases are the more well known states terrestrially, plasma is by far the most common state of matter in the universe, making up stars and the interstellar medium. Terrestrial plasmas include lightning, fluorescent lamps and arc-welding torches; as well as the more technological plasmas found in high power laser ablation, semiconductor ion implantation, inertial confinement fusion and, indeed, ion sources. If one takes a neutral gas and heats it up sufficiently, then the constituent atoms and molecules will dissociate, leaving a collection of charged electrons and ions: a plasma. A gas will usually be in thermal equilibrium, whereby the particles have had sufficient time to collide multiple times and distribute their velocities uniformly in Maxwell-Boltzmann distribution (MBD)

$$f(v_x, v_y, v_z) = n\left(\frac{m}{2\pi kT}\right)^{3/2} \exp\left(-\frac{m(v_x^2 + v_y^2 + v_z^2)}{2kT}\right) \tag{3.1.1}$$

where n, m and (v_x, v_y, v_z) are the particle density, mass and velocity components, k is the Boltzmann constant and T is the temperature. However ion source plasmas are typically short lived, have strong wall interactions and have shocks from the igniting power supply. Therefore, these plasmas are usually far from thermal equilibrium — the electrons, ions and neutral particles have different velocity distributions, which don't typically follow MBDs. Nevertheless, the mean velocity, $\bar{v}$ and kinetic energy, E_K associated with an MBD are widely used to estimate the properties of an ion source plasma:

$$\bar{v} = \sqrt{\frac{8kT}{\pi m}} \quad ; \qquad E_K = \left\langle \frac{1}{2}mv^2 \right\rangle = \frac{3}{2}kT \quad . \tag{3.1.2}$$

The boundary between a hot gas and a true plasma is somewhat vague, since there are many factors involved, such as the particle densities and temperatures, ionization degree, collision rates and confinement effects. Therefore a set of criteria is defined which must be fulfilled if a collection of particles may be referred to as a plasma [21]:

1. the plasma volume must be much larger than one Debye length
2. the particle density inside a Debye sphere must be large
3. the plasma frequency must be larger than the collision frequency

For a plasma with electron number density n_e and permittivity ϵ_0, the Debye length

$$\lambda_D = \sqrt{\frac{\epsilon_0 kT}{n_e e^2}} \tag{3.1.3}$$

is the mean distance over which charge perturbations can exist. A plasma is quasineutral, meaning the total number of positive and negative charges is equal. Any local imbalance in the electric field will quickly attract charges of the opposite polarity, thus removing the charge imbalance. However if, for example, a probe held at positive voltage is inserted into the plasma, it will tend to attract electrons but repel positive ions. This local charge imbalance only exists for a short distance — the Debye length — outside which the charges distribute themselves so as to screen the probe from the bulk plasma. For a collection of particles to be called a plasma, it must be overall quasineutral, therefore charge imbalances should be confined to relatively small regions inside the plasma. That is, the overall plasma size

$$L \gg \lambda_D \tag{3.1.4}$$

which is the first plasma criterion, stated above. The total number of particles within a *Debye sphere* of radius λ_D is approximately

$$\Lambda_p = \frac{4}{3}\pi\lambda_D^3 n_e = \frac{4}{3}\pi\left(\frac{\epsilon_0 kT}{n_e^{1/3} e^2}\right)^{3/2} \tag{3.1.5}$$

which is also known as the *plasma parameter*. The plasma parameter can vary over a wide range, so a subtly different parameter known as the *Coulomb logarithm*, $\ln\Lambda$ is often used instead, where $\ln\Lambda \simeq \ln\Lambda_p$. To screen a charge imbalance successfully, a great many particles are required so that microscopic fluctuations in the field are negligible and the plasma acts as a collective ensemble rather than being dominated by individual particles. Therefore $\Lambda \gg 1$ or, using Eq. 3.1.5

$$\lambda_D \gg {n_e}^{-1/3} \tag{3.1.6}$$

which is the second plasma criterion.

3.1.1 Collision and Oscillation Frequencies in Plasmas

The Coulomb logarithm is used in equations 3.1.12 for calculating various collision rates between particle species in the plasma. The collision frequency of electrons on neutral gas particles can be written as

$$\langle \nu_{en} \rangle = n_n \sigma_{en} \langle v_e \rangle \tag{3.1.7}$$

where σ_{en} is the collision cross section. For a typical Penning ion source[1] plasma with $T_e = 2$ eV, which is what will be discussed in this thesis, σ_{en} is approximately 1×10^{-19} m^2 [23]. Using Eq. 3.1.2, the electron velocity is around 1×10^6 ms^{-1}. With a typical neutral gas density $n_n = 1 \times 10^{21}$ m^{-3}, this leads to $\nu_{en} = 100$ MHz. Regarding collision processes, it is also convenient to introduce the mean free path

$$\lambda_f = \frac{1}{n_n \sigma_{en}} \tag{3.1.8}$$

which for the given example corresponds to a mean free path of 10 mm: on the order of typical Penning ion source dimensions. Local charge fluctuations can occur, causing microscopic electric fields which attract nearby particles, thus cancelling the fluctuation. Electrons react faster to field fluctuations than heavy ions, so they oscillate across the fluctuation many times before the ions begin to move. The electron oscillation frequency, or *plasma frequency*, is given by

$$\nu_p = \frac{1}{2\pi} \sqrt{\frac{n_e e^2}{\epsilon_0 m_e}} \tag{3.1.9}$$

and the corresponding *ion plasma frequency* of ions with charge Z is

$$\nu_{pi} = \frac{1}{2\pi} \sqrt{\frac{n_i (Ze)^2}{\epsilon_0 m_i}} \tag{3.1.10}$$

Both the electron and light ion plasma oscillation frequencies are in the GHz range so are significantly higher than the neutral collision frequency mentioned above. This means that a plasma is dominated by collective charge screening behaviour, rather than by collisions as a neutral gas would be. In fact

$$\nu_p > \nu_{en} \tag{3.1.11}$$

[1]Nobel-prize-winner Hans Dehmelt [22] coined the term 'Penning Trap' in appreciation of Frans Penning whose idea it was to superimpose electric and magnetic fields to store charged particles.

is the third criterion to define a plasma. Coulomb collisions among electrons and ions also occur [24], where $M = m_{i,1}m_{i,2}/(m_{i,1} + m_{i,2})$ is the reduced mass of two different ion species:

$$\begin{aligned} \langle \nu_{ei} \rangle &= \frac{\sqrt{2} n_i Z^2 e^4 \ln \Lambda}{12\pi^{3/2}\epsilon_0^2 \sqrt{m_e}(kT_e)^{3/2}} \\ \langle \nu_{ii} \rangle &= \langle \nu_{ei} \rangle Z^2 \sqrt{\frac{m_e}{2M}} \left(\frac{T_e}{T_i}\right)^{3/2} \\ \langle \nu_{ee} \rangle &\approx \langle \nu_{ei} \rangle \frac{n_e}{n_i Z^2} \end{aligned} \tag{3.1.12}$$

If a plasma is confined with magnetic fields, then the final major oscillation frequency is that of the charged particles orbiting magnetic field lines. Using the Lorentz force law and Netwon's second law, particles in a uniform magnetic field B describe helical paths, travelling with a uniform velocity $v_\parallel$ parallel to the field line and orbiting with a velocity $v_\perp$ around the field line. The *Larmor radius* of the orbiting particle is

$$r_L = \frac{2\pi v_\perp}{\Omega} \tag{3.1.13}$$

where

$$\Omega = \frac{eB}{2\pi m} \tag{3.1.14}$$

is the *Larmor*, *cyclotron* or *gyro* frequency. In a 0.25 T magnetic field, the Larmor radius is typically on the order of μm for electrons and mm for light ions such as hydrogen. The pulsed-arc-type Penning ion source studied in this thesis utilises caesium as well as hydrogen. Heavy Cs ions also have an associated cyclotron frequency, but they cannot complete full orbits as the Larmor radius is on the order of cm: larger than the source dimensions.

The range of frequencies possible in a typical Penning ion source is listed in table 3.1. In general, there are four broad frequency ranges which can be seen in an ion source: the plasma and cyclotron frequencies are in the GHz; collisions of electrons with other particles are in the high tens of MHz; hydrogen cyclotron and collision frequencies are in the low MHz; and effects due to caesium are in the tens of kHz range. Note that from Eq. 3.1.12, the collision frequencies strongly depend on particle temperatures; so if the temperature doubles, the frequency decreases by 66%. These frequency bands will be compared with real measurements of the noise seen on the pulsed arc in Section 4.3.

Table 3.1: Major frequency components in a Penning plasma with $n_n = 1 \times 10^{21}$ m^{-3}, $n_e = n_{H^+} = 1 \times 10^{19}$ m^{-3}, $n_{Cs^+} = 1 \times 10^{18}$ m^{-3}, $B = 0.25$ T, $T_e = 2$ eV, $T_i = 2$ eV and 1% ionisation fraction

Parameter	Description	Frequency
Plasma Frequency		
ν_p	(Electron) Plasma Frequency	30 GHz
ν_{pH^+}	Hydrogen Ion Plasma Frequency	650 MHz
ν_{pCs^+}	Caesium Ion Plasma Frequency	20 MHz
Cyclotron Frequency		
Ω_e	Electron Cyclotron Frequency	7 GHz
Ω_{H^+}	Hydrogen Ion Cyclotron Frequency	4 MHz
Ω_{Cs^+}	Caesium Ion Cyclotron Frequency	30 kHz
Collision Frequency		
$\langle\nu_{en}\rangle$	Electron-Neutral Collision Rate	100 MHz
$\langle\nu_{ei}\rangle$	Electron-Ion Collision Rate	75 MHz
$\langle\nu_{ee}\rangle$	Electron-Electron Collision Rate	75 MHz
$\langle\nu_{ii}\rangle^{HH}$	Hydrogen-Hydrogen Ion Collision Rate	1.7 MHz
$\langle\nu_{ii}\rangle^{HCs}$	Hydrogen-Caesium Ion Collision Rate	1.2 MHz
$\langle\nu_{ii}\rangle^{CsCs}$	Caesium-Caesium Ion Collision Rate	150 kHz

3.1.2 Beam Extraction

As shown in Fig. 3.1, ion sources can be generally divided into two components: the plasma chamber and the extraction system. Plasma particles evacuate the plasma chamber through an emission or *outlet* aperture in the *plasma electrode*. They then experience an accelerating force from an *extraction electrode*, also known as a 'puller', which forms the particles into a beam. In the case of a negative ion source, the puller is biased positive relative to the ion source; which means negative ions and electrons are accelerated out of the plasma, whereas positive ions are repelled back into the plasma. As described in Section 4.2.1, it is actually more convenient to have the puller at laboratory ground potential and instead bias the ion source negative, achieving the same result. The function of the extraction system is to prepare a high quality (i.e. low emittance) beam of sufficient current for the accelerator application.

3.1.2.1 Extractable Current Density

The maximum extractable beam current depends on the space-charge limit and the production limit. The space-charge limit arises from the charge of recently-extracted ions shielding the plasma from the electric field of the puller, preventing any more

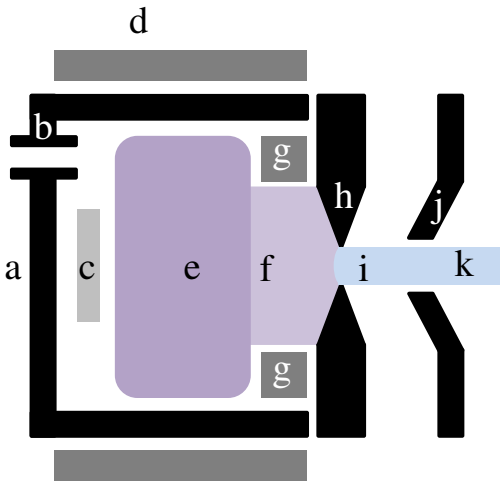

Figure 3.1: Schematic diagram of a typical ion source. A plasma chamber (a) encloses a region of space where a plasma is to be formed. Gas is injected into the chamber via a tube (b) and is ionised by some power source (c). The power source may be a filament or heated cathode, a radio-frequency antenna, an external source of electrons or some other method. The resulting plasma is confined by a magnetic field generated by permanent or electromagnets (d) mounted externally to the chamber. In the case of a negative ion source, the plasma is divided into a hot driver region (e) and a cool H^- production region (f) via a magnetic filter field generated by another set of magnets (g). The plasma chamber is closed by an electrically biased plasma electrode (h) which reduces the current of electrons co-extracted with the desired H^- ions through the outlet aperture (i). After leaving the aperture, the ions enter the extraction system whereby they are accelerated by a high voltage puller electrode (j) and formed into a focussed beam (k).

ions escaping. This maximum extractable current density, J is described by the Child-Langmuir law [25, 26]:

$$J = \frac{4}{9}\epsilon_0\sqrt{\frac{2Ze}{m}}\frac{V^{3/2}}{d^2} \tag{3.1.15}$$

where ϵ_0 is the vacuum permittivity, Ze and m are the ion charge and mass, V is the extraction voltage and d is the separation between the plasma and puller electrodes. If the area of the outlet aperture is A, then the total extractable beam current, $I = JA$. For a fixed extraction geometry, the constants in Eq. 3.1.15 can be isolated to give a fixed quantity known as the *perveance* of the extraction system, which – converting to practical units – is:

$$P = 1.728\frac{A}{d^2} \quad [\text{mA kV}^{-3/2}] \tag{3.1.16}$$

meaning $I = PV^{3/2}$. For the ISIS Penning source geometry, $P = 1.96$ mA kV$^{-3/2}$. The actual measured beam-perveance

$$P_B = \frac{I}{V^{3/2}} \tag{3.1.17}$$

can then be compared with the theoretical P to judge the efficiency of the beam extraction set point. The other factor affecting the maximum extractable current is the production limit. If the plasma density is not sufficiently high to produce the desired ion species, then the emission current density will be limited, no matter how high the extraction voltage in Eq. 3.1.15. The total beam current will follow the Child-Langmuir $V^{3/2}$ curve up to some voltage, then saturate away from it. In this case, the only way to produce a higher beam current is to increase the plasma density.

3.1.2.2 Emittance

Total current is only one aspect of beam extraction. If the beam is too large and divergent, then some proportion of the current will not be transported through the rest of the accelerator, reducing efficiency. The 'transportability' of a particle beam is quantified by its *emittance*: the lower the better. Emittance is the total volume in the six-dimensional *phase space* of positions and momenta $f(x, y, x, P_x, P_y, P_z)$ and is generally a fixed quantity after extraction from the ion source. Similarly, the volume in phase space available to fit the beam into is known as the accelerator *acceptance*. Including the momenta makes the emittance/acceptance a more complete analysis than simply real-space 'size'. For example a beam may be physically small enough to fit into the entrance of a pipe. However that beam may be very divergent so could collimate and be lost further inside the pipe. In that case, the beam does *not* fit into the pipe acceptance. In a beam transport system, particles are moved around in phase space with, for example, the beam envelope getting smaller transversely but larger longitudinally; however the total volume (i.e. emittance) of the 6D hyper-ellipsoid remains constant. The process of manipulating the phase space volume such that it fits into the accelerator acceptance is called *matching*.

For a CW beam near an ion source, transverse and longitudinal dynamics are independent, so it suffices to concentrate on the transverse phase spaces (x, P_x) and (y, P_y). Moreover, assuming the momentum is significantly larger in the z-direction than in the x- or y-directions, then transverse deviation angles, x' and y' may be considered:

$$x' = \frac{P_x}{P_z} \qquad \text{and} \qquad y' = \frac{P_y}{P_z} \tag{3.1.18}$$

which is beneficial, since angles are generally much easier to measure than small momenta. An *emittance scan* thus requires a beam to be sampled in transverse position, making beamlets which are then sampled in angle. Each position and angle sample comprises a pixel in phase space with a measured current density amplitude, $I(x, x')$. Scanning over a range of positions and angles builds up a complete (x, x') or (y, y') plot, with higher intensities generally centred at $x = x' = y = y' = 0$ for a Gaussian-like beam. Performing a statistical summation of the second moment of the particle distribution gives the RMS emittance [27]

$$\epsilon_{RMS} = \sqrt{< x^2 >< x'^2 > - < xx' >^2}, \tag{3.1.19}$$

$$\text{with } < x^2 >= \frac{\sum x^2\, I(x,x')}{\sum I(x,x')},\ < x'^2 >= \frac{\sum x'^2\, I(x,x')}{\sum I(x,x')} \text{ and } < xx' >= \frac{\sum x\, x'\, I(x,x')}{\sum I(x,x')}.$$

Note that, measured in terms of angles, the absolute emittance in Eq. 3.1.19 decreases as the longitudinal momentum increases along the accelerator. To take this effect into account, the energy-normalised emittance is often used when comparing beam transport in different accelerators:

$$\epsilon_{RMS}^{norm.} = \beta^*\, \gamma^*\, \epsilon_{RMS} \tag{3.1.20}$$

where β^* and γ^* are the relativistic factors. An emittance plot generally takes the form of an ellipse in phase space. The RMS emittance corresponds to an ellipse with an area $A = \pi\epsilon_{RMS}$ and shape defined by

$$\epsilon_{RMS} = \gamma x^2 + 2\alpha x x' + \beta x'^2 \tag{3.1.21}$$

with the constraint

$$\beta\gamma - \alpha^2 = 1 \tag{3.1.22}$$

The parameters α, β and γ are known as the Courant-Snyder *Twiss Parameters* and determine the shape of the ellipse. The Twiss parameters can be determined statistically like the RMS emittance by

$$\begin{aligned} \alpha &= -\frac{< xx' >}{\epsilon} \\ \beta &= \frac{< x^2 >}{\epsilon} \\ \gamma &= \frac{< x'^2 >}{\epsilon}\,. \end{aligned} \tag{3.1.23}$$

The emittance determines the overall quality of a particle beam: the lower the better. However to achieve a match into the accelerator acceptance, the beam's phase space

ellipse must be oriented correctly, which makes the Twiss parameters equally important. The parameter α gives an impression of the overall beam divergence, where negative and positive values imply a divergent or convergent beam, respectively. The parameter β, along with the emittance, gives an impression of the size of the beam.

The normalised emittance is a fixed quantity throughout the accelerator after extraction from the ion source, as long as all beam optical transformations are linear. If the beam experiences non-linear space-charge forces or is close to the edges of electrostatic lenses, then additional transverse energy may be imparted on outlying particles, increasing the overall emittance. These effects are most strongly felt near the ion source, so a well designed extraction system is imperative to preserve the emittance.

3.2 The Typical Ion Source

3.2.1 Plasma Confinement

The purpose of an ion source is to provide ions to an external experiment or accelerator complex. Therefore the plasma must be confined long enough for sufficient numbers of collisions to occur, such that a desirable extracted beam current is produced. As shown in Fig. 3.1, plasmas are generated in a dedicated volume of space called a *plasma chamber*, which is evacuated with vacuum pumps through the *outlet aperture* from which the ion beam emerges. The medium to be ionised is injected into the evacuated chamber usually in the form of a gas, before being ionised. The mean free path of collisions is usually the same order of magnitude as the plasma volume dimensions. Therefore only one or two collisions are likely to take place before the particle is lost to the walls of the plasma chamber. Since the area of the outlet aperture is a small fraction of the total plasma chamber surface, only a low proportion of ionised particles would find their way out of the plasma to be formed into a beam. If multiple collisions are required to create the desired species of particle, then the likelihood of that happening within a few mean free path lengths falls off dramatically.

Therefore, plasmas are confined with magnetic fields such that particle loss to the walls is minimised and multiple collisions are possible before the particles escape the outlet aperture. Charged particles are trapped by magnetic fields in two ways. Firstly, Eq. 3.1.13 shows that charged particles orbit around magnetic field lines at the Larmor radius dependent on their energy. Low energy electrons spiral tightly

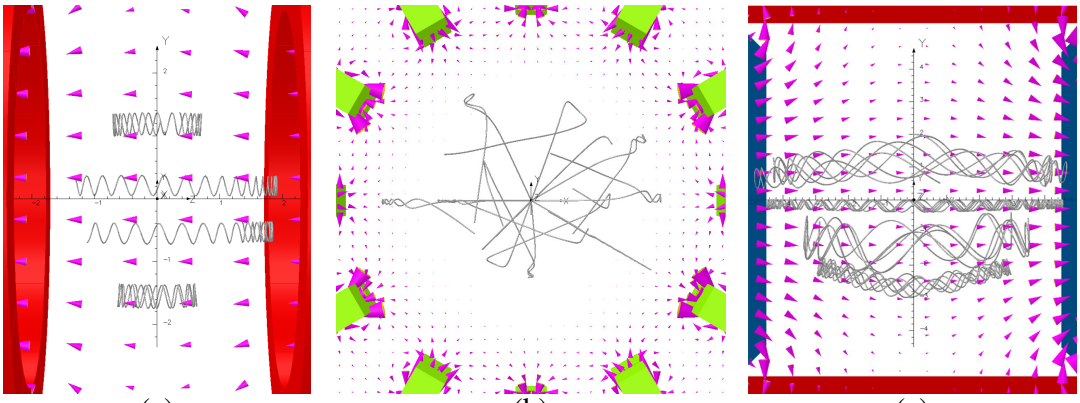

Figure 3.2: Solenoid (a), bucket (b) and dipole (c) magnetic confinement schemes. The magnetic field lines are shown as pink arrows whose size represents the field strength. Grey curved lines denote example particle trajectories.

around field lines and are said to be *magnetised*. Secondly, if a particle spiralling along a field line approaches a slowly increasing magnetic field, its transverse orbital velocity increases. Magnetic fields cannot change total kinetic energy, so conservation of energy requires the particle's parallel velocity to decrease. At some stage the field is strong enough to bring the parallel velocity to zero and the particle is reflected back by the *magnetic miror*. Generally, then, a charged particle plasma will be confined inside a magnetic 'bottle' and the plasma volume expands to fill the bottle dependent on how quickly the magnetic field increases at the edges.

Three broad arrangements are used to take advantage of these magnetic confinement techniques, as summarised in Fig. 3.2. The *bucket* chamber consists of several permanent magnets arranged with alternating poles facing into the plasma chamber. This creates a strong *multicusp* field localised near the magnets, which falls off to zero in the centre of the plasma. The larger the number of magnets, the larger is the field-free region, and hence the larger the size of the plasma. Solenoids may be used for confinement, whereby the magnetic mirror is parallel to the overall ion source and beam axis. Electron cyclotron resonance (ECR) ion sources [28] use a solenoidal field arrangement, often in combination with a simple hexapole cusp field. Finally a simple dipole field may be used to constrain transverse motion, whilst an electric field is used in place of a magnetic mirror to confine longitudinally. This last magnetic arrangement is that used in the Penning ion source discussed in this thesis.

3.3 Negative Ion Source

A negative ion is formed when an extra electron is added to the outer orbital of a neutral atom. It is much more difficult to add an extra electron stably than it is to remove one to form a positive ion. For example, a hydrogen molecule requires 4.52 eV to dissociate into two neutral atoms [29] and the binding energy of the single electron of a hydrogen atom is 13.6 eV. On the other hand the electron binding energy or *affinity* of a negative hydrogen ion is only 0.75 eV [30]. Therefore, although an H^- ion is stable and will not spontaneously decay, it is very fragile and needs to be removed from the destructive processes in the vicinity of a plasma as quickly as possible.

3.3.1 Volume Production

There are two main production processes for H^- ions: volume and surface production. Volume production occurs in the main plasma volume of an ion source and relies on the collision rates and energies discussed in Section 3.1.1 to be well controlled such that production rates exceed destruction rates. Molecules can vibrate and rotate around the centre of mass, but only at quantised energies labelled ν and j, respectively. When vibration and rotation occur together, the overall oscillation may be called *ro-vibration*. The dominant volume production process is by dissociative attachment of a slow electron to a ro-vibrationally excited hydrogen molecule [31]. This is a two step process, with a peak in the cross section for a $\nu > 4$:

$$\begin{aligned} e(E_K > 20 \text{ eV}) + H_2(\nu = 0) &\rightarrow H_2(\nu > 4) + e \\ e(E_K < 2 \text{ eV}) + H_2(\nu > 4) &\rightarrow H^- + H \end{aligned} \tag{3.3.1}$$

In order to reconcile the need to have two separate populations of electrons (high energy to excite the molecules and low energy to create the H^- ions), ion sources which use this technique usually have a magnetic *filter field*. This is a magnetic mirror to fast electrons but allows neutral atoms and molecules, as well as slow electrons, to diffuse past, thus forming the right conditions for enhanced volume H^- production near the outlet aperture.

3.3.2 Surface Production

A positive ion or neutral atom near a metal surface has its electron affinity level shifted and broadened [32]. If the affinity comes below the Fermi level of the metal, there is a finite chance of an electron quantum tunnelling across the potential barrier

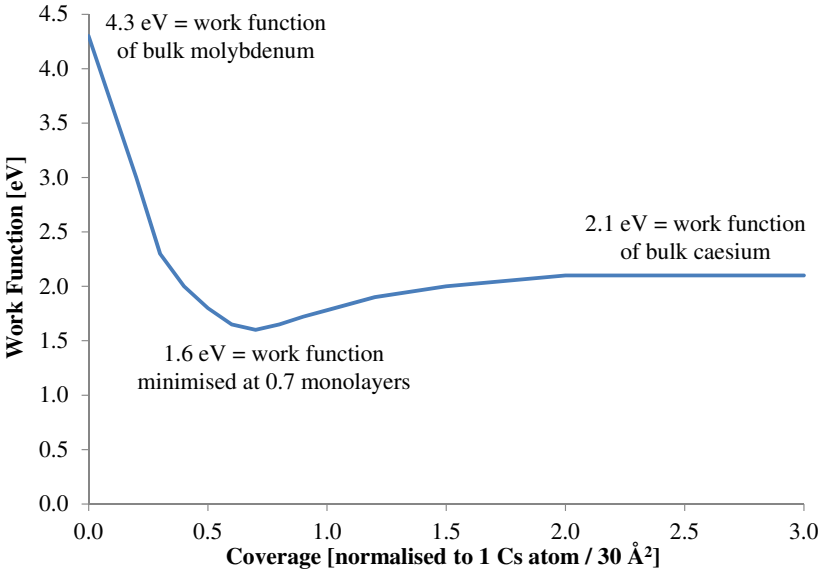

Figure 3.3: Minimising the work function of a cathode substrate by adsorbing a thin layer of caesium. Reproduced from reference [34].

to be captured, forming a negative ion. Positive ions can be attracted to a low work function cathode material and reflected back into the plasma after picking up two electrons. Similarly, neutral atoms adsorbed on the surface may be sputtered away, again taking an electron with them in the process. Surface H^- processes depend on the velocity of incoming sputtering particles and the work function of the metal surface. Therefore caesium – the element with the lowest work function at 2.14 eV [33] – is often added to reduce the cathode work function as much as possible.

The commonly held belief, demonstrated in Fig. 3.3 is that the work function has a mimimum below that of both the cathode and of caesium itself. This minimum occurs when a coverage factor of 0.6 monolayers of caesium (the *adsorbate*) is added on top of an already low work-function material (the *substrate*) such as molybdenum [35]. The reason this minimum occurs can be summarised by the following process [34]: Adding a single adsorbant onto the substrate causes a local increase in the valence electron charge density due to the polarisation of the electron clouds into dipoles. An increased valence density means more electrons are available to be freed from the surface and hence a reduction of the work function. Adding additional caesium atoms decreases the distance between neighbouring adsorbants, meaning the local dipole fields begin to overlap and weak covalent bonds begin to form. At this point the valence electron charge density maximises and the work function is minimised. With higher surface coverage, the covalent bonds begin to form a uniform crystalline

structure; the increased electron charge density is counteracted by the proximity of adsorbed positive ions and the work function slowly rises to that of bulk caesium. The exact values of the minimised work function and the optimum coverage factor depend on the substrate crystal orientation, smoothness, purity, cleanliness and temperature [36]. Recent results have shown that this minimised work function phenomenon doesn't actually hold true in the presence of a plasma [37], but the 'caesium effect' discovered by the Russians [38] is certainly real and higher H^- beam currents are produced in caesiated ion sources.

Maintaining the work function is thus of paramount importance in a surface-production ion source. High power plasmas may heat the surfaces of the plasma chamber, evaporating adsorbed caesium. Caesium may also be sputtered off the surfaces by fast or heavy plasma particles. To counter these two *desorptsion* processes, caesium vapour is usually injected continually from an external reservoir. This being the case, optimal conditions for efficient H^- production are arrived at over time in a surface ion source, rather than simply 'dialling in' a known set of operational parameters on start-up like in a volume source.

Caesium usage brings another problem in that it enhances spark rates on the high voltage electrodes close to the ion source. This is again because of the low work function of caesium: field emission rates are increased, thus adding extra particles to possible avalanche breakdowns. As caesium is usually added continually to the ion source, neutral caesium can escape the plasma and coat nearby surfaces rather rapidly. Therefore as well as arriving at optimal H^- production rates, sparking needs to be carefully controlled. Finally, caesium is highly reactive so must be handled carefully in the ion source build and refurbishment procedures. The search is on for alternatives to caesium, such as lanthanum-hexaboride or negative-affinity diamond-like carbon [39, 40, 41], but until these technologies have matured, the added complications of using caesium are a small price to pay for the orders of magnitude higher H^- output from surface-production ion sources.

Table 3.2: Recent performance of major H^- ion sources used in operational accelerator facilities. The beam duty cycle is the product of beam pulse length and pulse repetition frequency.

Ion Source	Technology	Caesium	Beam Duty Cycle	Beam Current	Lifetime
D-Pace	Filament-Driven	No	100%	10 mA	3 weeks
RADIS	External Planar RF Antenna	No	100%	1 mA	n/a
PKU	Microwave ECR	No	100%	25 mA	n/a
Linac4	External Helical RF Antenna	Yes	0.03%	45 mA	7 weeks
SNS	Internal Helical RF Antenna	Yes	6%	50 mA	6 weeks
J-PARC	Internal Helical RF Antenna	Yes	1.25%	33 mA	6 weeks
LANSCE	Filament-Driven Surface Converter	Yes	5%	18 mA	5 weeks
FNAL	Magnetron	Yes	0.23%	90 mA	9 months
ISIS	Penning	Yes	1.5%	55 mA	4 weeks

3.4 Operational H^- Ion Sources

There are a great many H^- ion sources in both operational facilities and in test stands, plus there are large negative ion sources for fusion applications. Table 3.2 gives an overview of a select few in use at accelerator facilities worldwide. For a more thorough review of operational sources, please see [42, 43].

3.4.1 D-Pace Filament

A commercial spin-off [44] from the filament-driven multicusp volume source used at the TRIUMF cyclotron in Canada [45], the D-Pace filament source is now in use at

many international facilities. Using a large tantalum filament and 5 kW of arc power, the unique filter-field arrangement is able to produce up to 15 mA of CW H^- beam.

3.4.2 RADIS Planar Antenna

A negative hydrogen ion source driven by a 13.56 MHz external planar RF antenna has recently been installed on one of the cyclotrons in Jyväskyla, Finland. Although only requiring a modest beam current of 1 mA, the extraction optics and overall power efficiency have been very well optimised. With a simple aluminium-nitride RF window as the only relatively-fragile plasma-facing part, long lifetimes are expected [46]. D-Pace are now interested in making a commercial spin-off of this source.

3.4.3 PKU Microwave

Peking University have been working on a microwave driven, caesium-free H^- ion source. There have been many failed attempts by several labs over the years to produce high H^- beam currents at large duty factors in an RF or microwave-driven ion source; see for example [47, 48, 49, 50, 51]. Nevertheless, the PKU 2.45 GHz ECR source is able to produce over 25 mA of H^- beam current at any duty cycle without the addition of caesium. With no filaments or other replacable parts, the ECR source has no apparent lifetime limitations. If this result can be verified by another team then the PKU ion source will be a game-changer [52].

3.4.4 Linac4 External Antenna

An upgraded copy of the highly successful DESY external antenna bucket source [53], the CERN Linac4 source is designed to operate at a higher duty cycle whilst producing more beam. It uses an octupole cusp field and a five-turn external RF antenna to feed 40 kW of 2 MHz RF power into the plasma. Originally intended to be operated without caesium, as at DESY, the required operational parameters could only be met with the introduction of caesium. A two-day stabilisation period is required after installing the ion source, however persistent beam currents have been demonstrated for seven weeks [54].

3.4.5 SNS Internal Antenna

Another multicusp volume source, but with higher coupling efficiency with the 2.5-turn RF antenna held inside the plasma, the SNS source operates at high duty cycles. With a pulsed discharge power in excess of 50 kW, and with a temperature

controlled outlet aperture, the SNS source is an excellent all-round performer. By using caesium-chromate cartridges housed in the outlet aperture and a precise start-up procedure, this ion source can maintain high beam currents without the need for continual caesium injection. The ion source injects around 50 mA of beam into a compact electrostatic LEBT which focusses the beam into the RFQ. Around 38 mA of beam exits the RFQ, whose transmission is very sensitive to ion source and LEBT alignment [55].

3.4.6 J-PARC Internal Antenna

Originally operating with a lanthanum-hexaboride solenoidal filament, the J-PARC ion source has been retro-fitted with an SNS-type RF antenna. Operating with an external caesium reservoir, carefully positioned filter magnets and a sophisticated computer-controlled feedback system, the J-PARC source is now producing 33 mA of H^- beam current in user operations, with the ability to increase to 50 mA during machine physics periods [56].

3.4.7 LANSCE Converter

A 6 kW pulsed discharge is ignited from a set of specially shaped tungsten filaments, whilst caesium vapour is continuously applied to a converter plate. Positive ions, attracted to the negatively-biased converter, sputter H^- ions from it. These are then back-accelerated and focussed across the plasma toward the outlet aperture due to the converter's spherical geometry. The set-up and stabilisation time of this source is over 36 hours, but it can operate at a wide variety of repetition rates [57].

3.4.8 FNAL Magnetron

Derived from the BNL magnetron [58], the FNAL magnetron is an excellent example of an H^- ion source with an long lifetime and high H^- beam current, albeit at a relatively low duty factor. A pulsed arc is confined to rotate around a cathode 'bobbin' by the $E \times B$ drift from a dipole magnetic field and the electric field between cathode and anode. A spherical dimple on the cathode focusses the H^- beam across the high density plasma to the circular outlet aperture. With only 15 A of arc current, over 80 mA of H^- beam current is extracted reliably for many months with a new solid-state 35 kV pulsed extraction power supply [59].

3.4.9 ISIS Penning

A higher duty factor cousin of the magnetron, the ISIS Penning source is shown in Figs. 3.4 & 3.5. Hydrogen and caesium enter a void between cathode faces via holes in a central anode. A pulsed arc plasma is ignited between the cathode faces and confined by a dipole magnetic field arranged perpendicular to the cathode faces. Operating at high duty factors requires air and water cooling for the source body and cathode, respectively. Surface-produced H^- ions have no direct line of sight from the cathode to the outlet aperture, so must undergo resonant charge exchange with slow neutral hydrogen atoms to reach the outlet. This process yields a beam with low energy spread and emittance. After being extracted by a puller electrode, the H^- beam is deflected 90° by a dipole magnet before entering the rest of the accelerator. The ISIS source [60] is essentially unchanged from the LANL source of the 1980s [61], itself derived from the original Penning ion source developed by Dudnikov in the 1970s [62]. With 30 years of operational experience, it has been replicated in several international facilities [63, 64] due to its high emission current density, low emittance, reasonable lifetime, simple operation, rapid replacement and relatively low cost.

The ISIS ion source has undergone significant development over the last ten years, primarily to deliver a 60 mA, 10% beam duty cycle, low emittance H^- beam for the Front End Test Stand (FETS) project [5]. Nevertheless, increasing efficiency and facility up-time is an on-going pursuit and several possible improvements are explored in this thesis.

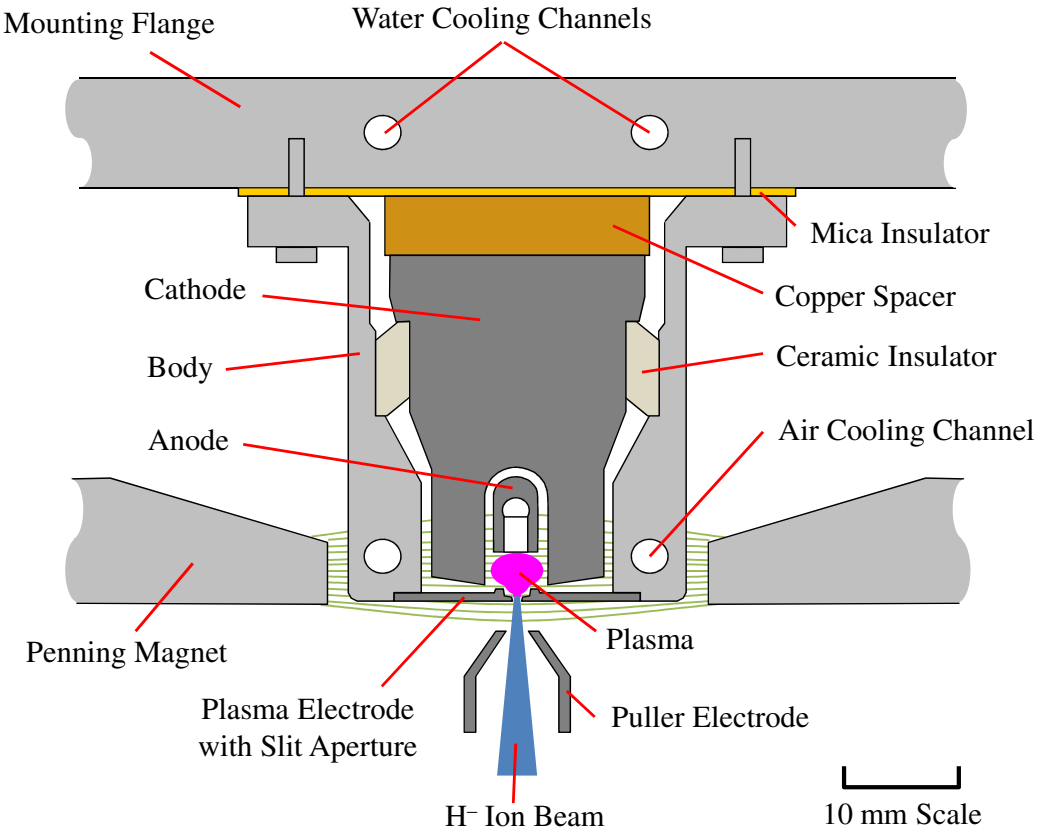

Figure 3.4: Schematic of the ISIS Penning H^- ion source.

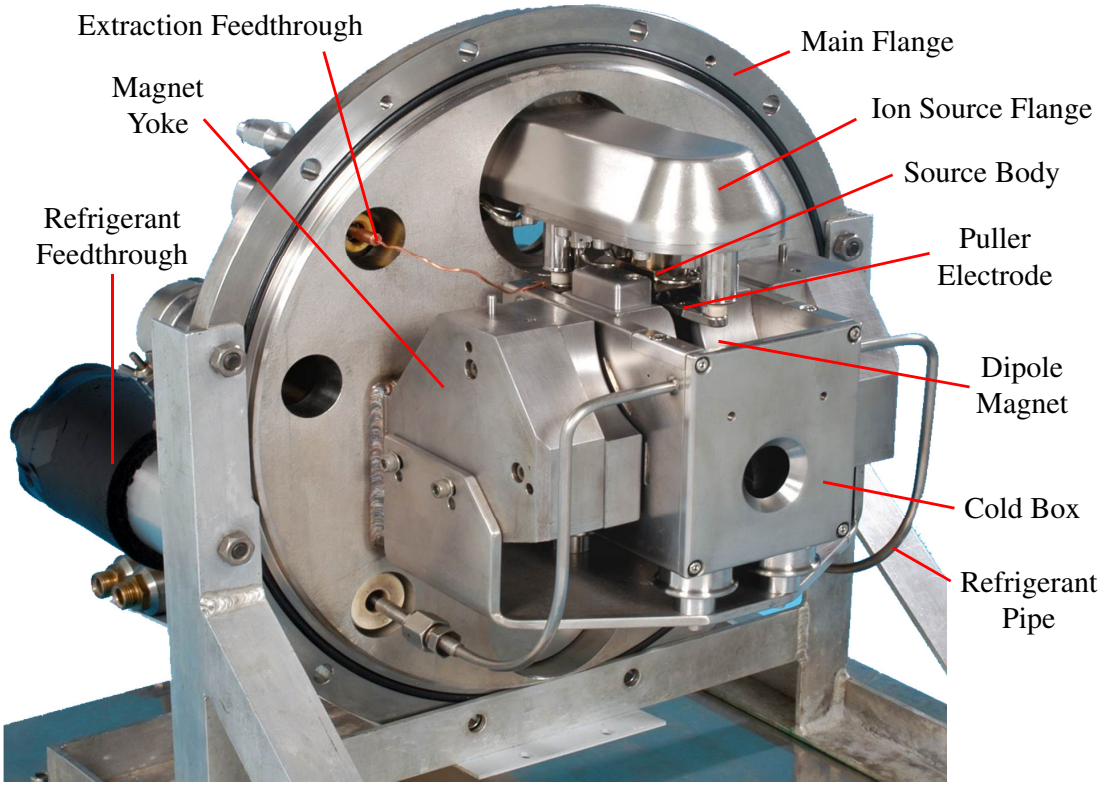

Figure 3.5: ISIS ion source in position above the dipole magnet and cold box.

Chapter 4

VESPA: the Vessel for Extraction and Source Plasma Analyses

In order to proceed with R&D work on the ISIS ion source, a new test facility was required. The requirements for this new facility – and indeed this thesis – were:

- Mount an ion source for horizontal beam extraction without a caesium trap.
- Measure the effect of removing caesium trapping.
- Include comprehensive beam diagnostics positioned close to extraction.
- Perform optical spectroscopy measurements of the ion source plasma.
- Characterise the existing extraction system without collimation.
- Design and test a new extraction system to transport a high brightness beam.
- Expansion room for future ion source R&D, such as a 'scaled source'.
- Use the same mounting flanges and HV insulator as the standard ISIS source.
- Test alternative ancillary equipment designs.
- Suitable safety and remote control systems for long-term source operation.

The new facility would, for the first time, determine exactly how the ISIS ion source plasma operates using optical techniques, and then have a new beam extraction and focussing system to deliver a low emittance, high current, loss-less H^- beam for future applications. The crux of this new facility would be a new vacuum Vessel for Extraction and Source Plasma Analyses (VESPA).

As can be seen in Fig. 3.5, the present ISIS ion source is mounted such that negative species are extracted from the source vertically downwards. A 0.235 T dipole magnetic field mass-separates electrons which are co-extracted along with the desired H^- ions. The H^- ions travel around the 90° bend of the magnet, whereas electrons are constrained to spiral close to the ion source and cannot move any further past extraction. The dipole magnet also has a quadrupole magnetic field component, giving some degree of weak focussing to the H^- ion beam. After the magnet, the beam is post-accelerated to the required 35 keV input energy of the next accelerator component. Previous studies [65, 66, 67] found that – despite the weak focussing effect – the H^- beam is sufficiently divergent after extraction that significant beam-loss occurs on the dipole magnet pole faces. The first measurement of beam current on ISIS is after the post-acceleration region, and typically 50-55 mA of beam current is produced. Simulations showed that to achieve this beam current, over 80 mA needed to be extracted from the ion source. Therefore perhaps as much as 40% of the H^- is lost on the dipole magnet, which is an extremely inefficient regime of operation.

The dipole magnet is housed inside a refrigerated 'cold box'. Held at a temperature of around 5 °C, the cold box condenses and traps the significant amount of neutral caesium escaping the ion source. Caesium, H^- and electrons begin travelling vertically downwards after the ion source. The mass-separating magnet ensures that neutral caesium continues downwards, away from the H^- beam, to be intercepted at the bottom of the cold box. This caesium trapping and mass-separation system works well, but has several drawbacks. Firstly, the extracted H^- beam passes through the dipole magnet at only 18 keV, resulting in severe space-charge-induced beam blow-up contributing to the beam-loss discussed. Secondly, with the downward-facing ion source emission aperture and the close proximity of a bulky magnet and cold box, there is no space or convenient viewpoint for diagnostics close to the ion source: it is essentially a 'black box', with no knowledge of beam or plasma processes happening within. The first beam diagnostics are over 150 mm downstream and there are no plasma diagnostics at all. Thirdly, the entire magnet and cold box must be held at extraction voltage, which adds significant challenges: such as how to energise the magnet and feed in refrigerant whilst at high voltage. Finally, the magnet and cold box require ancillary equipment which could fail, such as a refrigerator, water chiller, magnet power supply and lifting apparatus for the heavy magnet yoke and coil.

Because of these problems, one of the primary goals of the VESPA was to demonstrate direct, horizontal beam extraction without a caesium trap. A similar modification was made successfully on FNAL's magnetron [68] with no reported problems due to the lack of caesium trapping. Although a large undertaking and completely different way of operating the ion source, FNAL's experience gave confidence that the same benefits could be realised with a Penning source at ISIS. This chapter details the design process and commissioning results of the horizontally-mounted ion source.

4.1 Vacuum Vessel Mechanical Design

If the VESPA were only to perform plasma measurements, no beam extraction would be required. This would remove the need to include a high voltage insulator and the vessel could be made much more compact: limited in size only by the ion source mounting flange and the required diagnostic devices. In principle a simple off-the-shelf vacuum 'cross' would suffice. However, beam production requires the installation of a high voltage insulator, which imposes limits on the vessel dimensions.

4.1.1 High Voltage Insulator

The insulator had the following requirements:

- Hold off the required 35 kV in both air and vacuum.
- Suitable for affixing vacuum mounting and sealing surfaces.
- Have low moisture retention and out-gassing properties for vacuum operation.
- Mechanically strong enough to support the ion source flange.

As is shown in Fig. 4.1, high voltage insulators can take one of two general forms: radial or longitudinal. In the radial configuration, the ion source is mounted in the centre of a flat insulating disk. The outer diameter of the disk is large enough to withstand the high voltage on the air side. Whilst compact and very simple to manufacture, this type of insulator has the drawback of having large exposed areas on both the air and vacuum side. The insulator material must be thick and strong enough so as not to flex under vacuum loading from the large area exposed to air. The vacuum side can accumulate caesium or other impurities, creating a shorting path, or become damaged through repeated sparking [53].

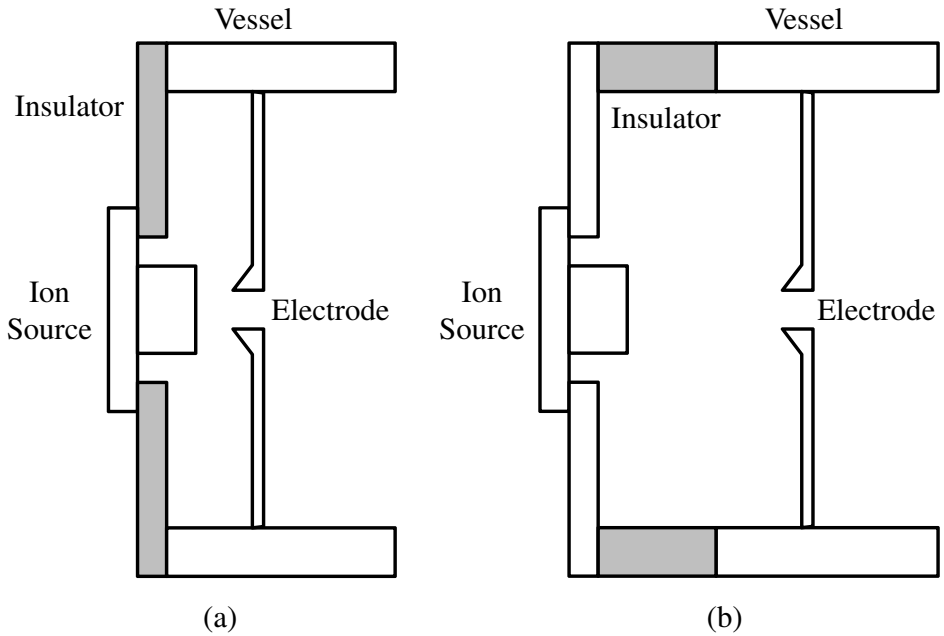

Figure 4.1: Radial (a) and longitudinal (b) high voltage insulator designs. Note how – with all things being equal – the ion source is moved away from the accelerating electrode with a longitudinal insulator.

A longitudinal insulator has the ion source mounted on one end of a hollow cylinder, whilst the other end is mounted on the vacuum vessel. This type of insulator is easier to shield from caesium and high voltage breakdowns, but is bulky and difficult to machine. The material must be strong enough mechanically not to flex under the weight of the ion source pulling down on one end. Also, the longitudinal insulator adds significantly more length to the beam extraction and transport than the radial design, which must be mitigated somehow.

The high voltage insulator used on VESPA was the same as that presently used on ISIS, with a longitudinal design approximately 100 mm long, and inner and outer diameters of approximately 400 mm and 450 mm, respectively. This type of insulator was chosen as it is a tried and tested geometry and is a viable spare in the event of an emergency on the operational source. Additionally, by using the same geometry insulator, the VESPA ion source can be installed immediately on ISIS without any modification to the mounting system.

The one difference between the existing ISIS high voltage insulator and the one manufactured for VESPA is the material. The existing insulator is made from glass-reinforced Noryl [69]. This amorphous blend of polyphenylene and polystyrene has all

the required characteristics (high electrical strength, high mechanical strength due to the impregnation with glass-fibre, good machinability, low water retention, low outgassing rate, low creep, etc). However in recent years it has become impossible to obtain in the large billet sizes required for this application. Ertacetal-C [70], which is a semi-crystalline copolymer grade of acetal, has similar properties to Noryl but is much easier to source in large billets. The Front End Test Stand (FETS) 65 kV insulator was manufactured from Ertacetal-C but suffered from regular high voltage breakdowns. The problem may have been caused by failings in the mechanical design (exposed triple junctions, inlaid metal tapped holes, etc), rather than the material properties, so it was decided to try the material on a known good geometry in the form of the existing ISIS insulator. So far the VESPA Ertacetal-C insulator has had no high voltage breakdown issues, so will be tested on the ISIS ion source during the 2017/03 operational cycle.

4.1.2 Ion Source Mounting Flange

The existing ISIS mounting flange shown in Fig. 3.5 is a flat stainless steel plate to which the ion source is bolted and which also holds the dipole magnet yoke, coil and refrigerant lines. As such it is a very heavy item which must be lifted into position by crane. The high mass of the flange is the reason for the glass-fibre reinforcement of the existing ISIS insulator: to counteract the torque of the flange whose centre of mass is outside the insulator. With the magnet yoke removed and a *top-loading* [71] ion source mounted for horizontal beam extraction, the flange was much less massive. In addition, to reduce the distance from the ion source emission aperture to the beam diagnostics, the flange was made re-entrant, like a top hat. The centre of mass was thus inside the insulator and the torque vastly reduced.

To limit caesium contamination on the insulator, a *caesium shield* is attached to the existing ISIS flange. This is an aluminium cylinder which sits just inside the insulator, limiting the amount of exposed material which could get covered in caesium, possibly leading to high voltage tracking and increased breakdown rates. Even with the caesium shield, the insulator needs regular cleaning through discolouration due to caesium getting past the shield. The re-entrant VESPA flange, on the other hand, is its own caesium shield and, when installed, leaves only 20 mm of exposed insulating material. So far, the VESPA insulator has needed no cleaning whatsoever.

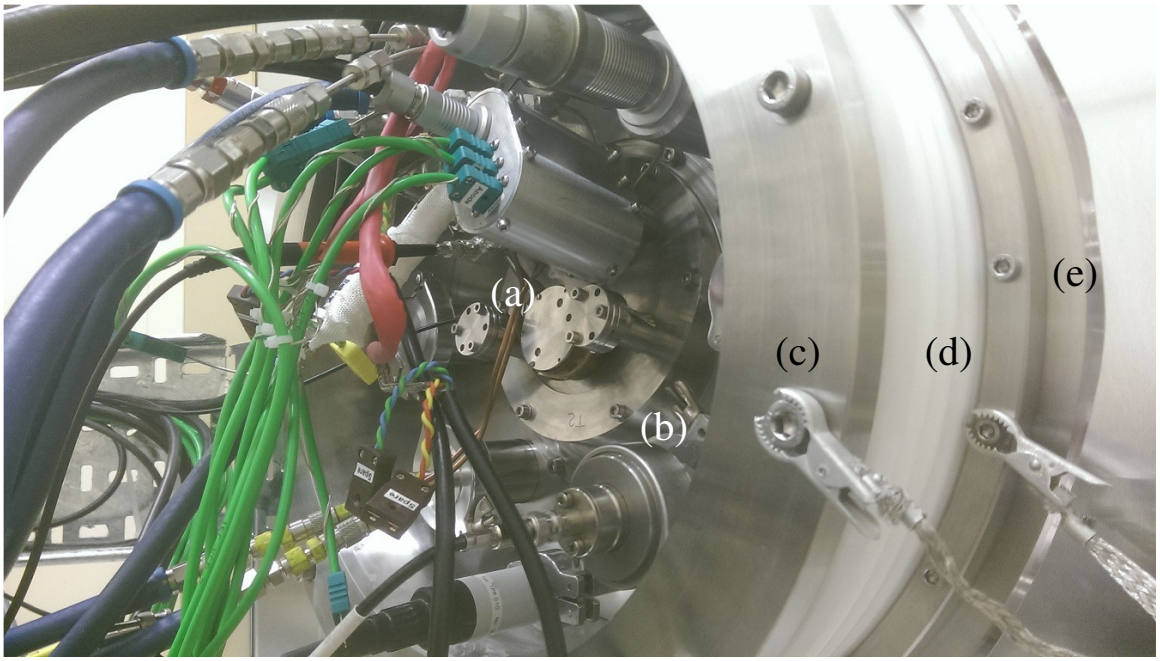

Figure 4.2: Ion source (a) mounted at an angle (b) on the re-entrant VESPA main flange (c). The high voltage insulator (d) separates the flange at 35 kV from the rest of the vacuum vessel (e) at ground.

With the dipole magnet yoke, coil and refrigerant lines removed, there was ample space on the VESPA ion source mounting flange for additional vacuum ports, despite the larger source flange of the top-loader relative to the standard ISIS variant. As well as the three ports required for vacuum pressure gauges and the puller electrode power connection, there were five assorted ports available for future use. For example, the new extraction cooling system discussed in Section 6.3 used one of the available KF40 ports as a water feedthrough. The mounting flange is shown in Fig. 4.2.

The ion source was positioned at the centre of the mounting flange. Although referred regularly throughout this thesis as being 'positioned for horizontal extraction', the H^- beam was actually deflected somewhat by the Penning magnetic field used for plasma confinement. The axis of the vacuum vessel, and indeed all subsequent accelerator components, was taken as the datum to which the beam should be aligned. In order to achieve a parallel, on-axis beam after extraction, the ion source should therefore be offset by the amount the beam is deflected. Particle tracking results discussed in Section 6.1 indicated an optimal offset of 12° in angle and 0.5 mm in vertical position. Flexibility is always desirable in systems when such precise offsets are required, as reality often differs from simulation. On the other hand, the ability

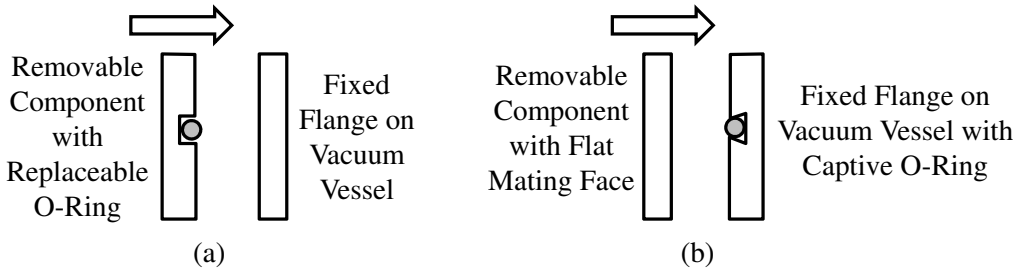

Figure 4.3: A removable component, such as an ion source, mounted onto a vacuum vessel requires its own o-ring (a) if the flat mating surface is on the vessel. If there is a family of several available ion sources, they each need their own o-ring, which may unduly increase the cost of spares. The necessity of spare o-rings also implies the o-ring is not held captive on the ion source so may fall out upon mounting, resulting in a vacuum leak. A single captive o-ring on the fixed vacuum vessel (b) is preferable.

to make minor adjustments whilst the ion source is operational, such as through the use of vacuum bellows, lead screws or stepper motors used in some ion sources [63, 72] is very expensive. Therefore adjustment was allowed for on the VESPA by means of an adaptor plate fixed semi-permanently on the mounting flange, onto which the ion source was located. The adaptor plate had the angle and position offsets required of the ion source yet was relatively inexpensive to manufacture. If emittance measurements subsequently showed the beam to be significantly misaligned relative to the vessel datum, a new adaptor plate could be made.

Two more advantages are afforded by the adaptor plate. The VESPA ion source mounting flange was designed to accommodate a different ion source, in the event one is needed in the future. For example, a *scaled* ion source [73] may need a new, larger mounting system. This could fit in place of the tilted adaptor plate, without any modification to the main mounting flange. It turned out that a prototype scaled source design did actually fit on the existing top-loader plate [74], but the possibility of future expansion is always helpful.

The second, more trivial advantage of the adaptor plate was the location of the vacuum o-ring. Ordinarily, demountable items are clamped onto a flange with an embedded o-ring already in place. For example, the standard ISIS ion source has a flat mating surface which locates onto an o-ring held captive in the mounting flange. As demonstrated in Fig. 4.3b, this ensures the o-ring is always in position, is easy to maintain cleanliness and only one is needed which can be used for all ten ion sources. The top-loading ion source, however, was designed such that an o-ring must

be located manually onto each ion source and clamped onto a flat mating surface on the mounting flange. This has, on occasion, led to the o-ring slipping off or getting dirty, both of which caused vacuum leaks. The VESPA tilted adaptor plate – and thus any future ion source design – itself clamped onto a captive o-ring in the mounting flange, but was flat on the source-facing side to allow for the loose o-ring system of the existing top-loading ion source. A photograph of the complete tilted ion source mounting assembly is shown in Fig. 4.2.

4.2 High Voltage Enclosure and Ancillary Equipment Installation

In principle an ion source takes up a very small amount of space compared to the rest of an accelerator. In practice, however, it requires additional room for ancillary equipment which powers and monitors the plasma, usually mounted in one or more 19" racks. Additionally, consideration must be made for how to float the ion source and ancillary equipment to high voltage. This section details the work involved in the construction of a high voltage enclosure and the layout of ancillary equipment.

4.2.1 Floating the Ion Source

In order to extract beam from an ion source, high voltage (HV) is applied to an electrode, which attracts and thus accelerates the charged particles. The problem is that the HV electrode is housed inside a vacuum vessel at laboratory ground potential. As Fig. 4.4(1) shows, a particle produced at ground potential and accelerated to HV will be decelerated again as it passes through the electrode and is exposed to the zero-potential of the vessel – and the rest of the accelerator. For the beam to gain additional energy, the entire rest of the accelerator would therefore have to be at the same potential as the HV electrode. To solve this clearly impractical dilemma, Fig. 4.4(2) shows how the ion source is instead *floated* to a potential equal and opposite to the voltage that would be applied to the electrode. In this case, a particle beam is created in a plasma held at a high negative voltage and accelerated to ground, thereafter continuing on at the energy it acquired during extraction, despite being at ground potential.

The difficulty with floating the ion source, however, is that the ion source and all equipment used to drive it must be operated whilst floating at HV. Since HV poses a serious electrocution risk, everything at HV must be shielded somehow from possible

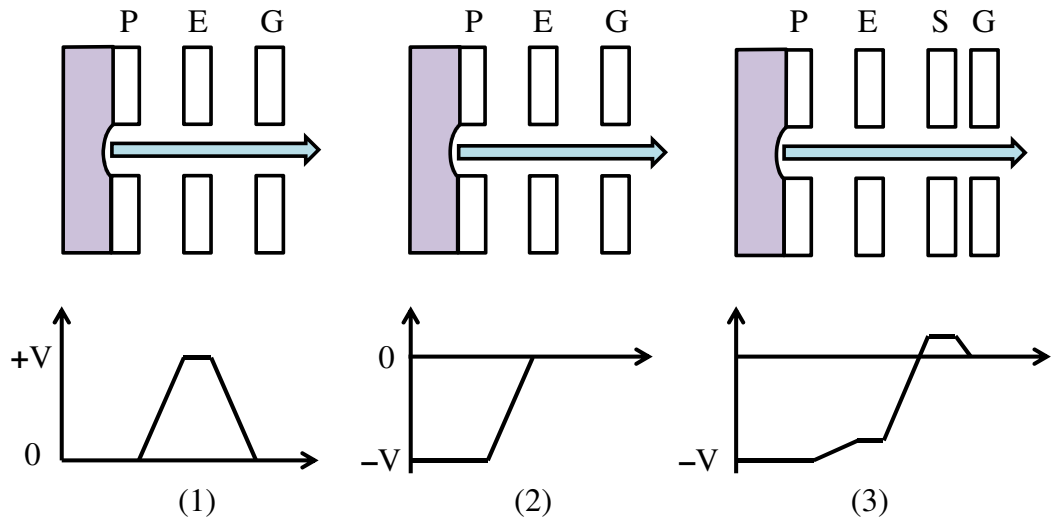

Figure 4.4: In (1), a negative ion beam emitted from a plasma potential (P) is accelerated to a positive extraction voltage (E). However upon continuing to the rest of the accelerator at ground (G), the beam loses all its energy. In (2), P is instead floated at a negative voltage, so the beam is accelerated towards E, which is at the same potential as G. A more sophisticated set-up in (3) shows that fine tuning of the beam parameters can be achieved with a small acceleration to E followed by a larger acceleration to the desired final energy at G. Particles of the opposite charge to the beam can be trapped by a small suppression voltage (S) just before G, to enhance space-charge neutralisation.

interaction with personnel. One solution is to put a small Faraday cage around the ion source, put the ancillary equipment in racks which are themselves floated inside larger, grounded racks and pass the connecting cables, hoses, etc (which are at HV) through a large, insulating pipe. This option means the vicinity around the ion source and racks is free to access as all hazardous parts are safely Faraday screened. On the other hand, the screening must be very well thought out to ensure no HV breakdowns occur across small distances to the screens. Multiple levels of interlocks are required as well, to ensure all screens are closed before high voltage can be applied safely.

The option for high voltage screening used on the VESPA was to house the ion source, ancillary equipment and connecting cables inside one large enclosure with only one point of access. This made interlocking simpler and reduced the number of close approaches which could incite HV breakdowns. On the other hand, an HV enclosure took up significantly more space than multiple small screens and it also prevented the user getting close to observe the equipment, so remote controls and monitoring were mandatory.

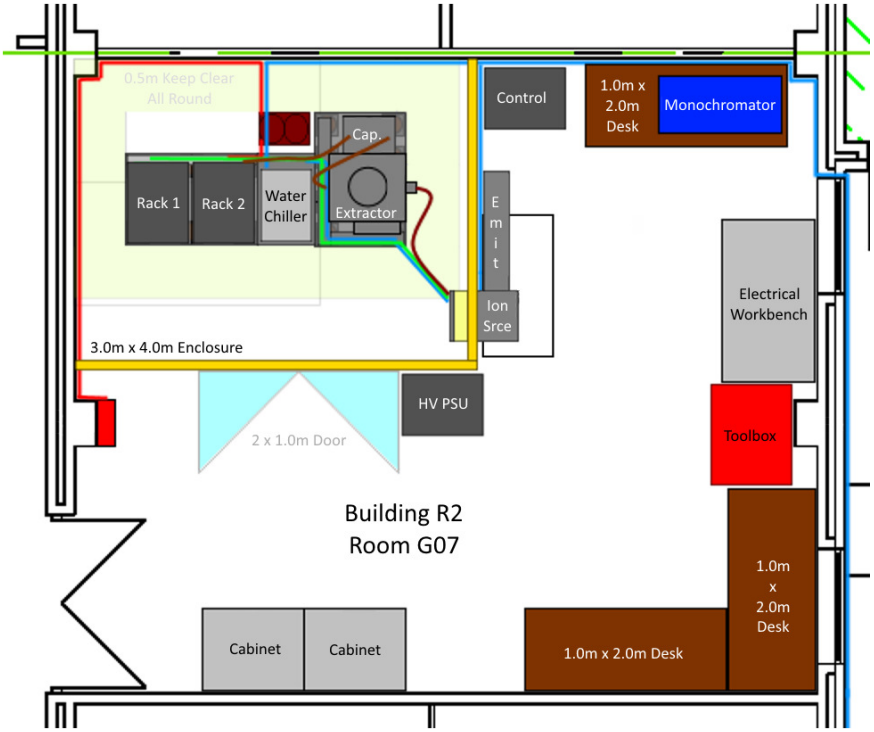

Figure 4.5: Layout of the VESPA laboratory.

4.2.2 High Voltage Enclosure Layout

A laboratory was acquired for the VESPA project with enough space for a high voltage enclosure, vacuum vessel, diagnostic equipment, controls desks and electrical workstations. The layout chosen by the author for the VESPA lab is shown schematically in Fig. 4.5. A partition wall was erected to create the HV enclosure. The vacuum vessel was located outside the enclosure and the ion source on its insulator protruded through a hole in the wall. Ancillary equipment was housed in 19" racks mounted on an HV *platform*. The platform was biased to high voltage relative to the laboratory ground by positioning it on ceramic insulating legs. The legs had *sheds* meaning they isolate the platform safely to 40 kV even if the legs were coated in water. This feature was important as the ion source required water cooling from a chiller mounted on the platform. Without sheds, the legs would suffer catastrophic damage from a high voltage breakdown in the event of a water leak from the chiller.

The HV platform was positioned a suitable distance away from the enclosure walls, to allow access all round such that equipment could be easily mounted or adjusted in the racks. Power cables and water hoses were connected to the ion source via trunking connecting the platform to the ion source mounting flange. This ensured

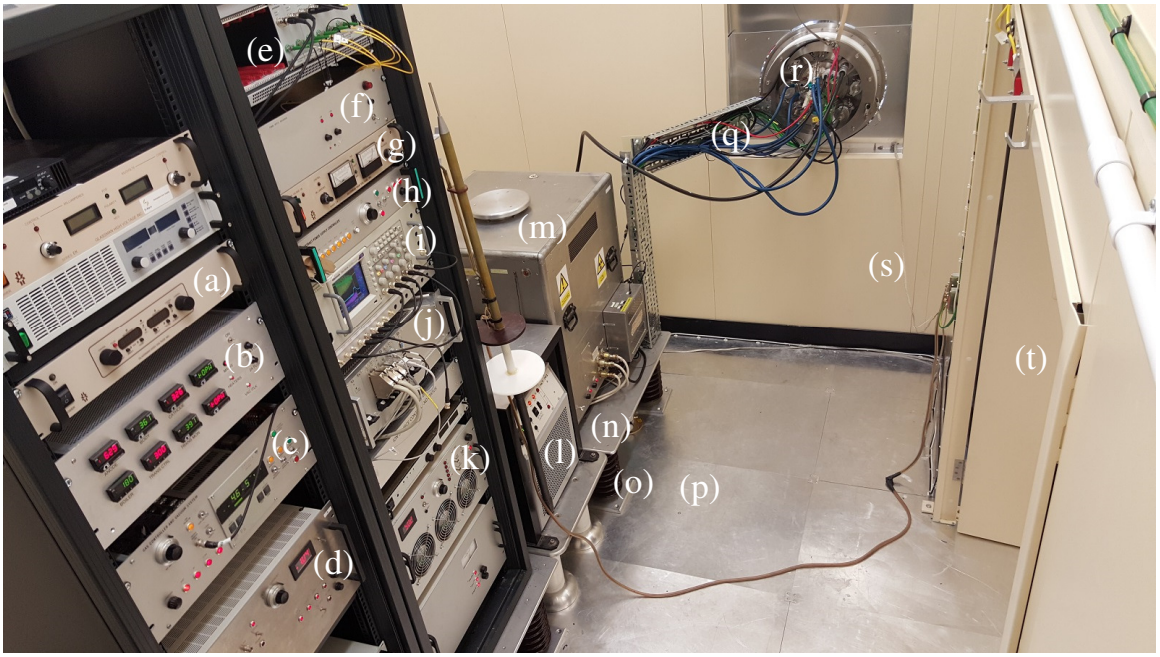

Figure 4.6: Equipment in VESPA high voltage enclosure. Refer to main text for item descriptions.

there were no trailing leads which could cause HV breakdowns. Finally, additional space inside the enclosure allowed for future expansion. The author prepared the laboratory area; designed and organised the erection of the partition wall; designed and installed the high voltage platform; designed and installed the vacuum vessel, and installed the cabling and pipework for the ion source. Electrical technicians constructed and installed the high voltage power supply, isolation transformer and mains electricity distribution. A photograph of the high voltage enclosure is shown in Fig. 4.6.

4.2.3 Ancillary Equipment

Although the ion source plasma generator fits in the palm of a hand, it required a large amount of ancillary equipment to run the plasma. The main items shown in Fig. 4.6 are the a) einzel electrode HV PSU b) temperature controller c) gas controller d) DC arc PSU e) RF-over-fibre link f) timing-over-fibre link g) extraction charging unit h) extraction valve control i) oscilloscope j) remote control interface k) pulsed arc PSU l) water chiller m) extraction valve pulser n) high voltage platform o) shedded insulator legs p) earth mat q) services trunking r) ion source s) enclosure walls and t) entry door.

The gas control crate set the flow rate of hydrogen into the ion source. It also generated interlock signals, disabling all other equipment if the vacuum collapsed. A crate, constructed by the author and discussed in depth in Section 4.2.3.1, was used to monitor source temperatures and provide closed-loop control of the caesium delivery system. With these two crates ensuring hydrogen and caesium were fed into the source, an arc discharge could be generated.

There were two arc power supplies. A low current DC arc power supply (DAPS) was used to warm up the ion source from cold to ∼400 °C: sufficient temperature to drive a high current arc. When cold, a high voltage (∼700 V) was required to generate a low current glow discharge. The arc was in *high impedance mode*. The discharge power – although low – was sufficient to increase the temperature of the source gradually. As the temperature increased, the rate of thermionic emission (and hence arc current) from the cathode increased. This effect was enhanced by the addition of caesium. A positive feedback process thus began, whereby the increased temperature led to higher currents, which in turn further raised the temperature. As the current increased, the arc voltage dropped. At around 2 A of DC arc current and 300-400 °C, the voltage rapidly fell to ≈70 V and the arc entered *low impedance mode*. At this transition, a higher current pulsed arc power supply (PAPS) could take over the operation of a pulsed plasma and the DAPS was turned off. Unless otherwise stated, variations in arc current discussed in Chapters 5 and 7 are referring to the PAPS current. The DAPS and PAPS were bespoke pieces of equipment which needed to be able to cope with the unusual *negative impedance* characteristics of the ion source discharge i.e. a higher set current required a lower driving voltage. Occasionally, the discharge could not strike using the PAPS alone, so a negligible amount of DC 'keep-alive' current could be injected in parallel from the DAPS.

Assuming H^- ions were generated inside the plasma by the processes described in Chapter 3, they needed to be extracted from the plasma and formed into a usable beam. A pulsed extraction power supply (EPS) performed this task. Note that the terms *extraction* and *puller* may be used interchangably. This power supply applied a ≈250 μs high voltage pulse to the puller electrode. The process to do this was rather involved, thus again the EPS was a bespoke piece of equipment. To summarise, an off-the-shelf Glassman *charging unit* powered a 1 μF *reservoir capacitor*, whose output was switched via a tetrode valve, thus generating an HV pulse which was applied to the puller. By switching the output of the reservoir capacitor in this manner, a

short pulse of relatively high current could be sent through the puller to achieve the high voltage required, despite originating from the low current charging unit. The charging unit output voltage was fixed at a high enough level to keep the capacitor charged, whereas the amplitude of the voltage pulse was varied by adjusting the grid voltage inside the tetrode valve. The valve was housed inside a floating chassis in the main extract pulser box and control signals were sent to it via fibre optics. The whole extraction system thus consisted of a charging unit, a reservoir capacitor and the valve pulser; as well as a dump relay to earth the capacitor safely when not in use. A higher-rated EPS with a more compact form-factor has been commissioned recently for FETS and ISIS, but was not available for VESPA at the time of writing [75].

The gas, arc and extraction pulses must all be timed accurately, so a set of on/off trigger pulses was generated from the ISIS central timing unit. The triggers, amplitude set-points and status indication signals were all shepherded by three control crates. The various pulsed signals were monitored on an oscilloscope.

4.2.3.1 Temperature Control

The caesium delivery temperatures were controlled by adjusting the electrical power through resistive heaters wrapped around the caesium oven and transport tube. On ISIS, the power is supplied from a 3 A, 110 V AC transformer, giving a maximum heating power of 350 W. The power is adjusted by varying the proportion of the 50 Hz sinusoid delivered to the heater using a phase-angle trigger module. The temperature monitoring, feedback, phase control and remote monitoring circuits are separate and rather complicated. Bulky transformers are required as part of the heating module, increasing the mass and taking up internal space in the temperature crate. Finally, some of the operational amplifiers are prone to failing in the event of an HV breakdown. Therefore, the author constructed a completely new temperature crate.

The new temperature crate was designed to be simpler, lighter, inexpensive, rugged and built using off-the-shelf parts. As such, the crate was based around Omega iSeries control units. These compact controllers had a multi-function display; were fully remote programmable; performed all the proportional integration and differentiation (PID) feedback necessary to reach and hold a temperature set-point, and had their inputs optically isolated from the output, making them rugged. This removed two of the printed circuit boards (PCBs) needed in the old crate. The heater power came from two dual-output 2 A, 50 V DC power supply bricks. Although

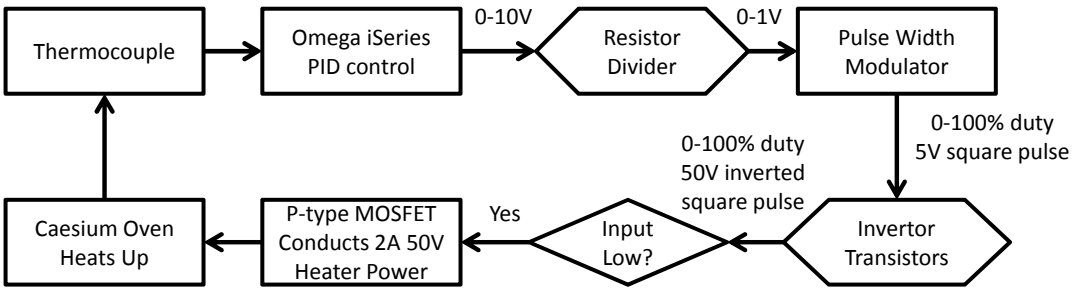

Figure 4.7: New temperature control crate operational principle. Four of these control loops were available in one PCB.

offering less power than the mains-powered phase-angle trigger modules, this only really had an impact on the ramp-up time at switch-on: there was more than enough power to sustain ≈300 °C on the caesium transport tube. The power was adjusted and delivered to the heating elements by MOSFETs driven by simple pulse-width modulator (PWM) circuits. A block-diagram of the technique is shown in Fig. 4.7.

Two other advantages of the new temperature crate were the simplified remote control scheme and the multi-function display. In the old crate, eight input/output channels were required: two inputs for the caesium set-points plus six outputs to read back the temperatures. The new system performed all the sets and reads for eight Omega controllers (i.e. 16 input/output channels) on a round-robin RS485 scheme, requiring just one serial connection. The Omega controllers' displays could be colour-coded to highlight any errors. For example the display value could be yellow during a temperature ramp-up, green when the set-point was achieved and red if the temperature was outside an acceptable range. The VESPA controllers were set to be green within a ±2 °C bracket around the caesium set-point and within ±25 °C of an acceptable value for each of the ion source cathode, anode and body temperatures; outside of these brackets, the displays were red. This colour function gave a quick indication whether the temperatures were within acceptable limits, even if the user was too far away to actually read the digits. The new temperature crate performed extremely well and, due to its simpler, cheaper and more rugged design, a batch is now being manufactured for ISIS operations and other ion source test areas at RAL.

4.3 Ion Source Commissioning

The first DC plasma was ignited in the VESPA ion source on the 27th of August 2014, with the first pulsed arc and beam extraction a month later. At first only one 2000 l/s turbo pump was installed which, due to the pressure-control loop discussed in Section 5.3, meant only a small hydrogen flow of around 10 ml/min was needed to increase the vacuum pressure to a 'normal' level. However the ion source needed a flow rate between 15 and 20 ml/min to operate effectively. At lower flow rates, the cathode, anode and body temperatures needed to be over 100 °C hotter than normal to allow enough thermal emission of electrons to sustain the discharge. Running at high temperatures lead to stability problems and generated less beam. On the other hand, increasing the set pressure to achieve a nominal flow increased the spark rate in both the ion source and extraction regions. To alleviate this problem, an additional 800 l/s turbo pump was installed, which brought the operating pressure, flow rate and temperatures to levels very consistent with standard ISIS operating settings. Therefore a high pumping speed and excellent temperature stability is essential for optimum operation of a high current Penning H^- ion source.

4.3.1 Plasma Noise

As well as the general plasma oscillation and collision frequencies discussed in table 3.1, the high power pulsed Penning ion source had interesting bulk plasma properties leading to low frequency resonant oscillations. A summary investigation was performed in the early days of Penning ion source development by Derevyankin and Dudnikov [76]. They postulated that resonant low frequency *ringing* was caused by the bulk motion of caesium ions, summarised in the following process:

1. A large voltage is needed to strike the arc plasma
2. Caesium vapour is continually injected into the plasma and covers the cathode
3. The cathode work function decreases as the caesium layer builds up
4. The arc voltage drops drastically with the decreased work function
5. The current sharply increases due to the negative impedance of an arc plasma
6. The increased arc current causes large sputtering of caesium from the cathode
7. The work function and hence arc voltage increases again so the current drops

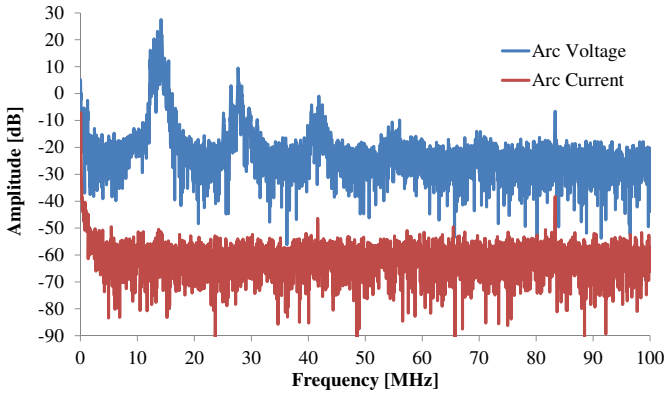

Figure 4.8: Pulsed arc power supply output current had a high frequency noise filter. A separate voltage probe at the ion source input could still see variations, though.

8. Sputtered caesium ions drift through the plasma toward the opposite cathode

9. The process repeats on the timescale of the traversal time of caesium ions between cathodes: on the order of 25 μs or 40 kHz.

A 1 GHz, 10 GS/s oscilloscope with a fast Fourier transform (FFT) function was used to perform a more rigorous study of plasma frequency components. Since ISIS operations require a clean, quiescent H^- beam pulse, high frequency plasma current fluctuations were filtered out in the arc power supply using a parallel 25 Ω resistor and 1 μF capacitor. However MHz-range signals could still be seen on a separate voltage probe, as shown in Fig. 4.8. As such, both the current and voltage signals were analysed in this study.

The low frequency ringing discussed above is demonstrated in Fig. 4.9. At low arc currents the plasma suffered significant ringing, which was not a suitable state to produce a stable ion beam. Studying the frequency response in Fig. 4.10, it can be seen that the amplitude of 40 kHz peaks mentioned in bullet point 9 above decreased at higher current set-points. In order to test whether operating the ion source at lower arc currents resulted in a longer lifetime, it was essential that a stable quiescent discharge could be achieved at low arc currents.

Typically on the ISIS operational ion source, the arc noise is suppressed by varying the caesium flux into the plasma. The flux is set by controlling the temperature of the caesium oven via a resistive heating element. As Figs. 4.11 and 4.12 show, the caesium oven temperature had a strong influence on low frequency arc noise. More impressive still is how the high frequency components in Fig. 4.13 were suppressed

almost completely above 150 °C. The drawbacks are those detailed in Section 3.3.2; namely that caesium adversely affects cleanliness and spark rates.

A study was performed on the ISIS Penning ion source to observe qualitatively the effect of increasing the plasma volume [77]. Although the plasma was only operated in high impedance, low current DC mode, it was found that increasing the cathode-cathode gap helped increase the duration of a noise-free discharge. It was postulated that the noise was caused by plasma turbulence, which was more likely to occur in low density plasmas confined with strong magnetic fields. An increased plasma volume takes longer to evacuate through a fixed conductance outlet aperture, so builds up a higher pressure from the pulsed gas injection. Charged particles in a magnetic field undergo collisional *diffusion* D at different rates perpendicular and parallel to the field [78]

$$D_\perp = \frac{k_B T_\perp}{m\nu_c[1 + (\Omega/\nu_c)^2]} \qquad D_\parallel = \frac{k_B T_\parallel}{m\nu_c} \tag{4.3.1}$$

where Ω and ν_c are the Larmor and collision frequencies, respectively, whilst $T_\perp$ and $T_\parallel$ are the perpendicular and parallel temperatures in a *bi-Maxwellian distribution*. The Einstein relation compares the diffusion coefficient to the electrical *mobility*, μ by

$$\frac{D}{\mu} = \frac{k_B T}{Ze} \tag{4.3.2}$$

therefore combining equations 4.3.1, 4.3.2 and 3.1.14, the charged particle mobility can be written as

$$\mu = \frac{1}{B}\frac{(\nu_c/\Omega)}{[(\nu_c/\Omega)^2 + 1]} \tag{4.3.3}$$

which is plotted in Fig. 4.14.

Dudnikov proposed [77] that plasma turbulence (and hence arc noise in the Penning ion source) may be suppressed by operating on the right hand side of the maximum in Fig. 4.14. That is, the collision frequency should be greater than the Larmor frequency. This can be achieved by lowering the magnetic field and/or increasing the gas density. To test this theory for the standard-sized plasma volume, the magnetic field was adjusted on the VESPA ion source, with the results plotted in Fig. 4.15. It can be seen than reducing the magnetic field was a viable method for noise reduction when combined with temperature adjustments, rather than solely relying on the caesium oven temperature as in Fig. 4.11. This technique made it possible to operate the ion source at lower arc currents.

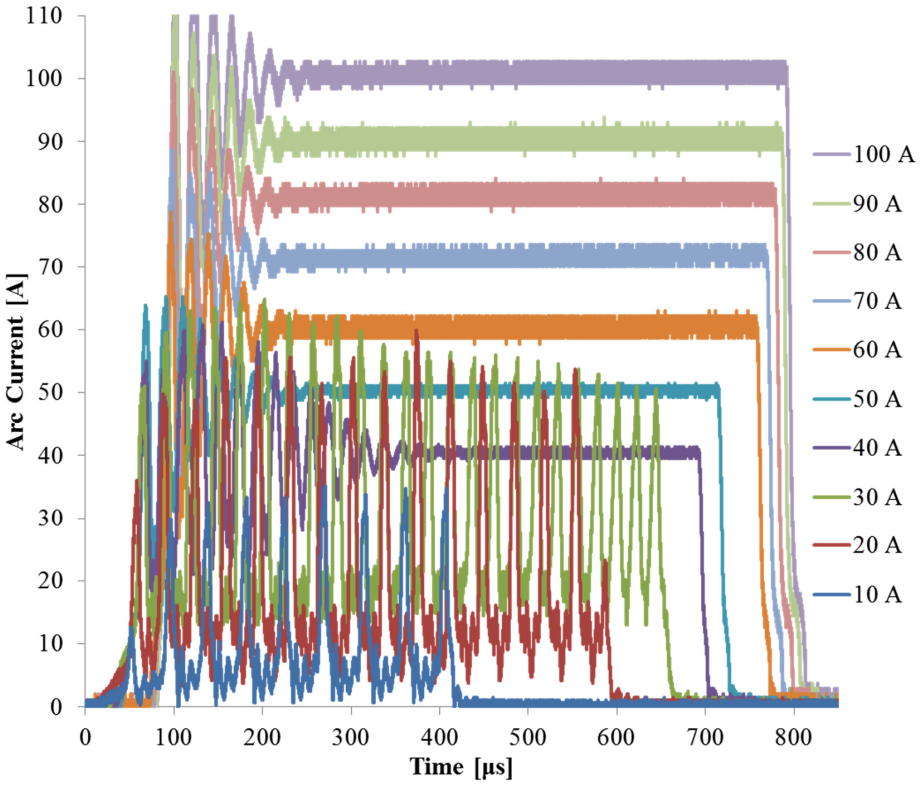

Figure 4.9: Arc pulse shape at various current set-points. Note the significant ringing below 40 A. Typical operational setting is 55 A, which provided a long quiescent discharge for stable beam production.

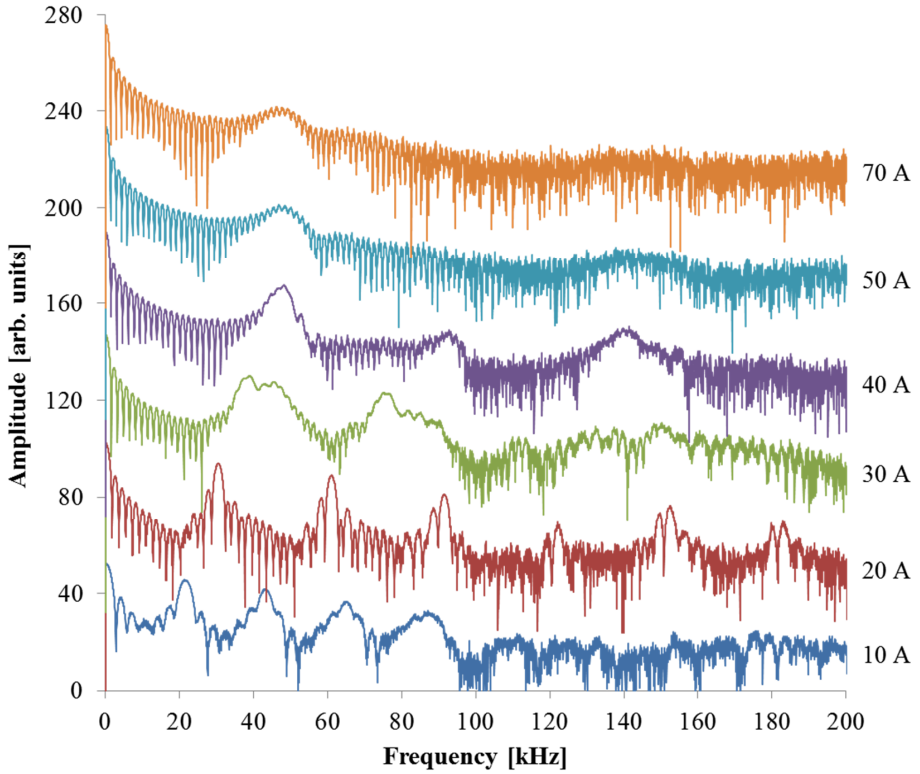

Figure 4.10: Fourier transform of the current signals shown in Fig. 4.9. Spectrum did not change for currents higher than 50 A, so number of datasets displayed is truncated for clarity.

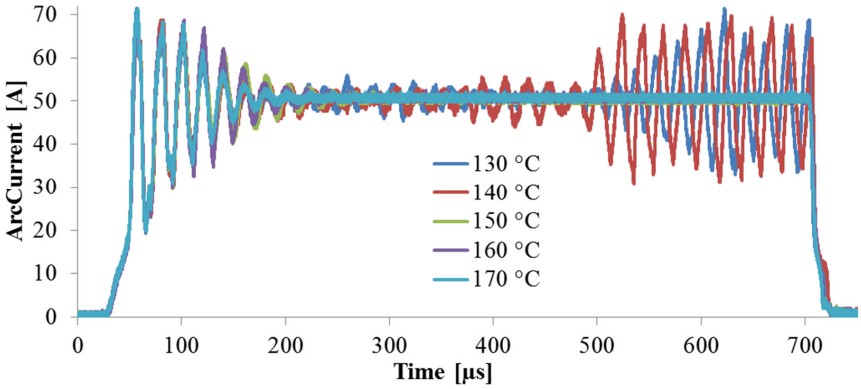

Figure 4.11: Arc noise suppression by increasing caesium flow rates using a resistive oven heater. Arc was quiescent for oven temperatures above 150 °C.

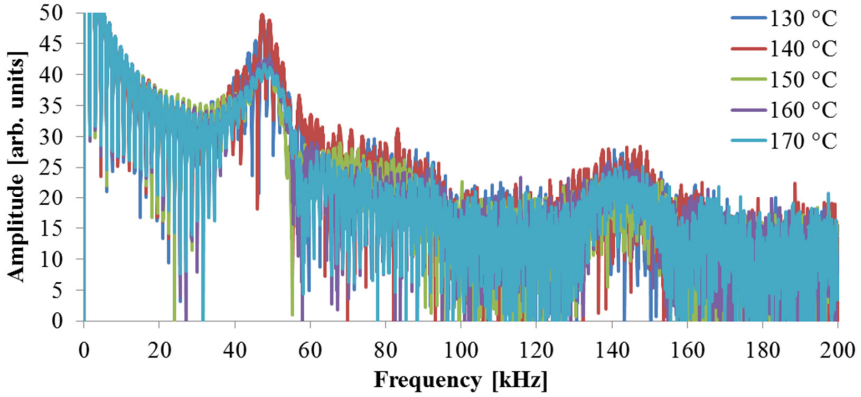

Figure 4.12: Low frequency components of signals shown in Fig. 4.11. Note how the amplitude of 50 kHz oscillations decreased significantly with increased oven temperatures.

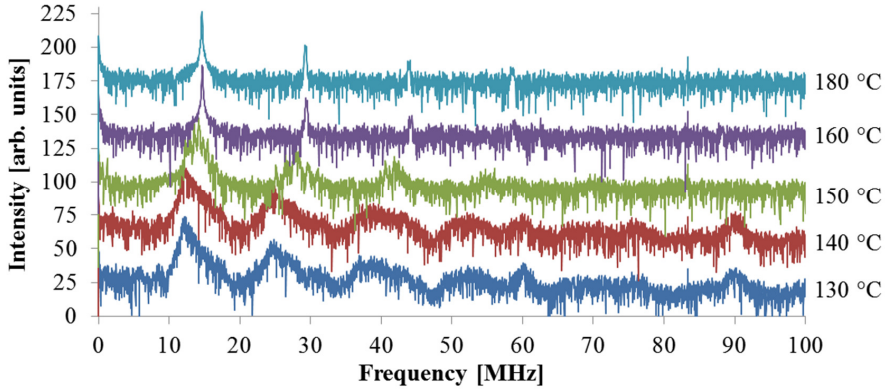

Figure 4.13: High frequency components of signals shown in Fig. 4.11.

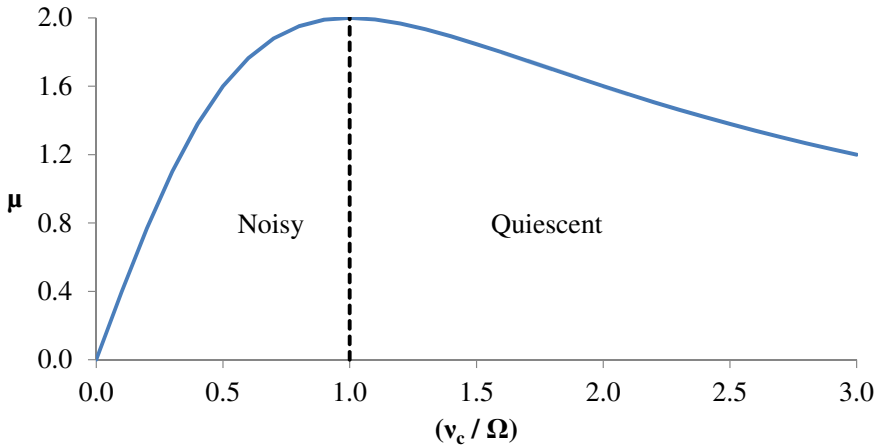

Figure 4.14: Charged particle mobility μ as a function of the ratio between collision and Larmor frequencies ν_c/Ω as described by Eq. 4.3.3, for a Penning magnetic field magnitude of 0.25 T. Operating on the right of the maximum is preferable for a quiescent discharge.

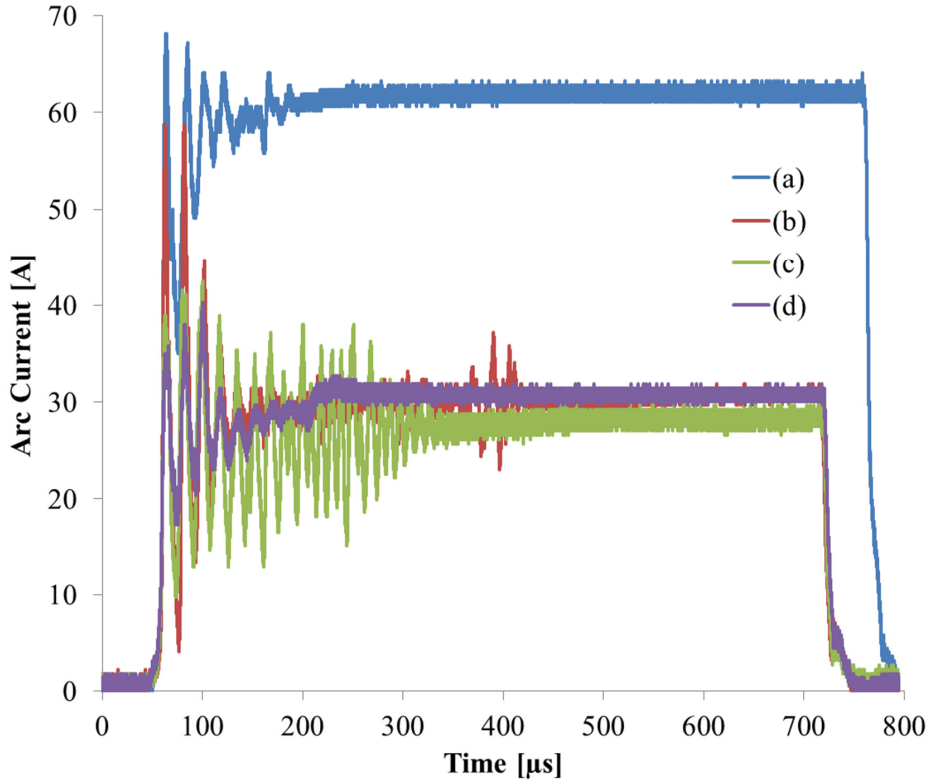

Figure 4.15: A standard, clean 60 A arc (a) was reduced to half the current (b), whereby the noise duration increased drastically. The Penning magnetic field was reduced (c) which successfully drew the noise duration back by 30%. The temperature balance was disrupted by operating at lower power, so the cooling was also adjusted (d) to bring the temperatures back to normal operational values, which further improved the noise duration.

4.3.2 Beam Commissioning

With the sector dipole magnet removed on the VESPA, the diagnostic equipment was brought closer to the ion source. The main beam diagnostic was the AC current transformer (ACCT) *toroid* which non-destructively measured beam current [79]. The magnetic field of a particle beam flowing through a ring of high permeability material induces a current to flow through a wire wrapped around the ring. Essentially, the charged particle beam is the primary turn of a transformer. The number of secondary turns on the ring determines the amplification, but the total inductance of the ring plus wound-wire also strongly affects the performance, such as bandwidth. The toroid manufactured by the author was designed to have a reasonably quick rise time (and hence high bandwidth) of 10 μs, plus a long droop time; meaning the measured pulse amplitude was less than 1% different from the input, for pulse durations of less than 1 ms. For a standard ISIS beam pulse of around 0.25 ms, the toroid had excellent performance in a compact form factor. On the other hand, the high permeability material inside the toroid was very sensitive to stray magnetic fields. Due to its proximity to the strong permanent magnets on the VESPA ion source, it was prudent to check the toroid's calibration.

A Faraday cup (FDC) is an alternative and even simpler method for measuring beam current: particles dumped on a metal plate charge it up, inducing a voltage. Measuring the voltage to ground across a resistor gives a direct measurement of the beam current flowing to ground. Although simple and high performance, FDCs have the disadvantage of being a destructive diagnostic device: the entire beam is lost during the measurement. Therefore an FDC was constructed and mounted on the emittance scanners (discussed in Section 7.1.4) with only 10 mm clearance from the toroid to ensure that the toroid and FDC both measured identical beam currents. Being insensitive to stray magnetic fields, the FDC could then be brought into the path of the beam to cross-check the toroid measurement. Figure 4.16 shows the beam diagnostic set-up on the VESPA.

Faraday cups have another disadvantage in that they have a limited collecting area. Beam ions impacting the cup generate *secondary electrons* which leave the cup, altering the measured current signal. Secondaries increase the current for positive ion sources and decrease it for negative ion sources. Similarly, electrons generated from interactions of the beam with residual gas particles can impinge on the cup, further altering the true signal. To combat the effect of secondaries, FDCs require

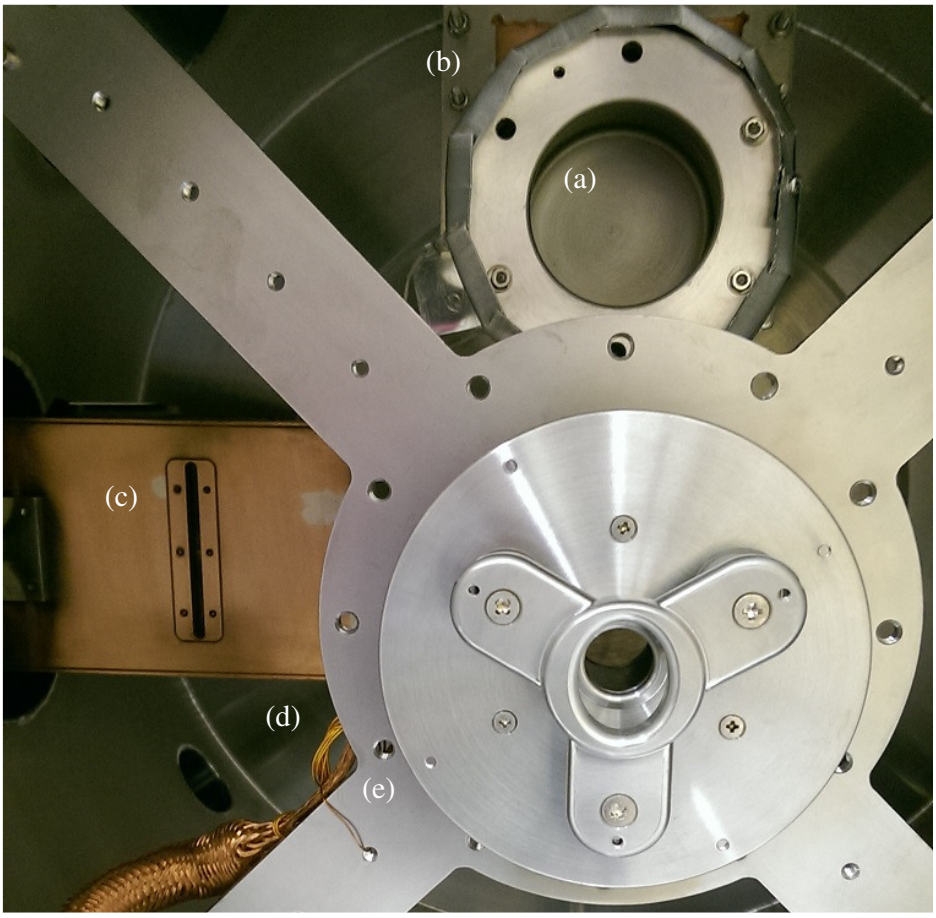

Figure 4.16: Diagnostics set-up for VESPA beam commissioning. A Faraday Cup (a) was temporarily mounted on the vertical emittance scanner (b). The sampling slit of the horizontal scanner (c) was visible to the left. An AC current transformer toroid (d) was mounted on the rear side of the electrode assembly (e).

a *suppressor* electrode to repel residual gas electrons trying to enter and secondary electrons trying to exit the cup. Stray electrons only have energies of a few tens of eV, so a potential hill of around 100 V is sufficient to suppress them. This brings us to the problem of size: to generate the hill at the cup central axis requires a higher set voltage on the suppressor electrode itself. The larger the electrode diameter, the higher the set voltage. Also, the the suppressor needs to be sufficiently long to ensure a big enough hill to prevent electrons escaping the cup. However long suppressors increase the travel distance of the beam to the cup itself, meaning a large, divergent beam could collimate on the suppressor before reaching the cup; i.e. a long suppressor reduces the cup *acceptance*. In general, then, the larger the cup collecting area, the higher the required suppressor voltage and longer the overall length. The FDC used on the VESPA was a spare from another project and – at 50 mm diameter – was close

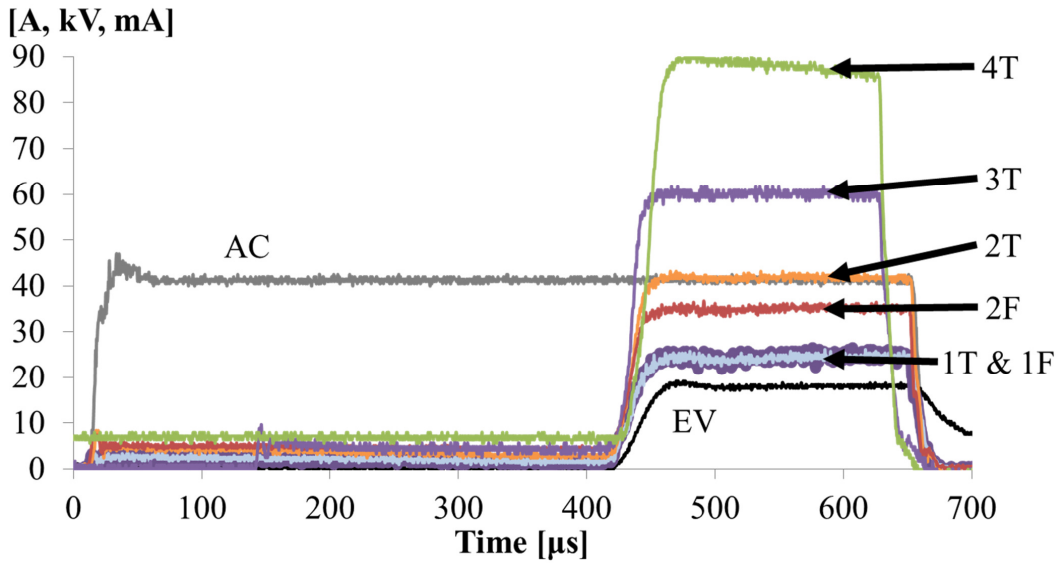

Figure 4.17: Beam commissioning experiments. With a constant arc current (AC) of 40 A and extraction voltage (EV) of 18 kV, beam was measured for various collimator set-ups. With front and rear collimators in place, the toroid (1T) and faraday cup (1F) recorded identical beam currents, validating the toroid calibration. With the rear collimator removed, the beam was divergent enough to collimate on the Faraday cup's suppressor elecrode. In this case the Faraday cup (2F) measured a lower beam current than the toroid (2T). Trace (3T) shows the beam current measured with both collimators removed but the ion source performing poorly. When the ion source pressure and temperature were in the nominal range, the beam current was increased to expected levels (4T).

to the practical size limits of a Faraday cup. This being the case, it was expected that the cup would be too small to capture the entire ion beam leaving the ion source.

Recall, though, that the FDC was only installed temporarily in order to calibrate the toroid. The toroid had an inner diameter of 82 mm and was much shorter in the beam direction so was guaranteed to measure all the beam, no matter how large or divergent. To calibrate the toroid properly with the FDC, then, the ion beam measured by both instruments was reduced in size by a pair of collimating holes installed before the toroid. These ensured the beam would be no bigger than 20 mm in diameter by the time it hit the cup and hence the whole collimated beam would be measured by both devices. Fig. 4.17 shows the results of toroid calibration.

With the small collimated beam, the measured current was identical on both the toroid and FDC. This proved that the magnetic field at the position of toroid was low enough not to affect its performance and hence the toroid behaved as expected. With

the rear collimator removed, some beam was already lost on the FDC's suppressor electrode so the measured current was reduced relative to the toroid signal. Therefore the FDC did its job of calibrating the toroid, but as expected, was unable to measure a large beam correctly; it was removed from all further measurements. With both collimators removed, the full extracted beam was measured for the first time. The effect of poor pressure and temperature, discussed in Section 4.3, is also shown in Fig. 4.17, as the beam current increased 30% with optimal ion source performance.

With the ion source commissioned and operating well, the Vessel for Extraction and Source Plasma Analyses (VESPA) could begin living up to its name. A new extraction system was designed in Chapter 6 and beam measurements were taken on the new system in Chapter 7. First, though, Chapter 5 discusses plasma measurements using optical techniques.

Chapter 5

Plasma Optical Spectroscopy

Plasma spectroscopy is a non-invasive diagnostic technique which can be used to identify the constituent components of a plasma as well as the dynamic processes happening within. The measurements are independent of the method of plasma ignition (high energy lasers, RF fields, hot filaments, etc) and only require a diagnostic window which gives line of sight into the plasma. Traditional plasma diagnostic methods, such as Langmuir probes [80], insert small delicate parts directly into a plasma. This requires complicated vacuum feed-through arrangements for laboratory plasmas and clearly cannot be performed at all for distant astrophysical objects. Spectroscopy equipment, on the other hand, is located remotely from the plasma, so the technical components can be handled with relative ease in a laboratory environment. The drawback of spectroscopy is that, although gathering the data is straightforward, analysing it and interpreting plasma phenomena is a complex process. This is especially true in low temperature, short-lived plasmas which are often far from thermal equilibrium and thus cannot be described by simple Boltzmann distributions.

Optical spectroscopy is divided broadly between absorption and emission spectroscopy. Absorption spectroscopy involves illuminating a plasma with an external light source and recording the decrease in transmitted light due to some proportion being absorbed by the plasma medium. The VESPA ion source plasma was far too small to mount an active absorption source on to; therefore passive optical emission spectroscopy (OES) was the technique chosen for this thesis.

5.1 Optical Emission Theory

5.1.1 Atomic Spectra

An excellent introduction to OES theory and techniques is given by Fantz [81]. Atoms and molecules have well defined emission spectra based on the energy levels of allowed electron transitions. An atomic electron may be excited from a low energy level q to a higher level p due to a collision with a nearby particle or absorption of a photon of sufficient energy. The excited electron will then decay to a different level k with a *transition probability* A_{pk}. Decays to different k levels are grouped in named *series*. For example, decays to the hydrogen ground state, $k = 1$ form the *Lyman* series in the UV region of wavelengths. Decays to $k = 2$ form the *Balmer* series at optical wavelengths. Decays to $k = 3$ form the infrared *Paschen* series, and so on. Given a *population density* $n(p)$ in the excited state, a distinct *emission line* will be emitted with an intensity in units of photons $\mathrm{m}^{-3}\ \mathrm{s}^{-1}$ given by

$$I_{pk} = n(p)A_{pk} \tag{5.1.1}$$

at a wavelength λ_0 given by the difference in level energies

$$\lambda_0 = \frac{hc}{E_p - E_k}\,. \tag{5.1.2}$$

The emission line is nominally at one precise wavelength, but in practice there is a *natural linewidth* caused by the Heisenberg uncertainty principle

$$\Delta E \Delta t \geq \frac{\hbar}{2}\,. \tag{5.1.3}$$

If the typcial lifetime of an excited state is 10 ns, then the uncertainty in energy is 6.6×10^{-8} eV, resulting in a natural linewidth on the order of 10^{-5} nm for visible light emissions, with a Lorentzian profile. The natural linewidth cannot usually be measured as other plasma processes broaden the line significantly more. For example, thermal motion of atoms moving toward and away from the observer causes Doppler broadening $\Delta\lambda_D$ of emission lines with a Gaussian profile given by [82]

$$\Delta\lambda_D = 2\sqrt{\ln 2}\lambda_0\sqrt{\frac{2k_B T_{gas}}{mc^2}} \tag{5.1.4}$$

where λ_0 is the central, unshifted line wavelength and T_{gas} is the temperature of the gas particles, which may be atoms, molecules or ions. Other broadening processes can occur at the same time. For example, emission lines can be shifted by Stark

and Zeeman effects from strong electric and magnetic fields, respectively. Similarly, if the plasma is particularly dense, collisional and pressure broadening processes can become significant. These effects have different shape profiles, generally Lorentzian or Gaussian, which convolute to give an overall Voigt line profile [83]. If meaningful measurements are to be made, it is therefore important to deconvolute the measured profile accurately. Alternatively, one can study emission lines which have only one dominant broadening process. For example, studying Eq. 5.1.4, Doppler broadening is more significant for long wavelength emission lines of low mass particles. Therefore the 656.28 nm Balmer H_α emission line of atomic hydrogen is a good choice to study Doppler broadening. A hydrogen plasma with $T_{gas} = 1$ eV will have an H_α Doppler linewidth of around 0.075 nm (75 pm), which is three orders of magnitude larger than the natural line width.

Another effect to take into account is the *instrument broadening*. This is the Gaussian response function (resolution, $\Delta\lambda_I$) of the spectrometer. Assuming a Gaussian emission line, the Doppler and instrument profiles add in quadrature to give a measured line width

$$\Delta\lambda_M = \sqrt{(\Delta\lambda_I)^2 + (\Delta\lambda_D)^2}\,. \tag{5.1.5}$$

For an accurate measurement of the real emission line, therefore, the instrument should have a resolution much less than the anticipated line width; typically 5 to 10 times smaller. This means that a spectrometer with a resolution of around 10 pm is required for precise Doppler broadening measurements.

5.1.2 Spectroscopic Notation

Plasmas normally contain several gas particle species: ions, atoms and molecules; each with its own emission spectrum. If multiple gas types are present in the plasma, many emission lines may be in close proximity. Therefore, again, a high resolution instrument is beneficial to pick out each line correctly and identify the species. Spectroscopic notation is used to label energy levels – between which electrons jump to generate emission lines – by:

$$n^{2S+1}L_{L+S}{}^{+,-}_{g,u} \tag{5.1.6}$$

where S is the total spin, $L + S$ is the total angular momentum and $2S + 1$ is the electron multiplicity [84]. n is the principle quantum number, denoted $1, 2, 3, 4...$ for atoms and $X, a, b, c...$ for molecules. L is the total orbital angular momentum, denoted by $S, P, D, F...$ for atoms and $\Sigma, \Pi, \Delta, \Phi...$ for molecules. The $+, -$ and g, u quantum

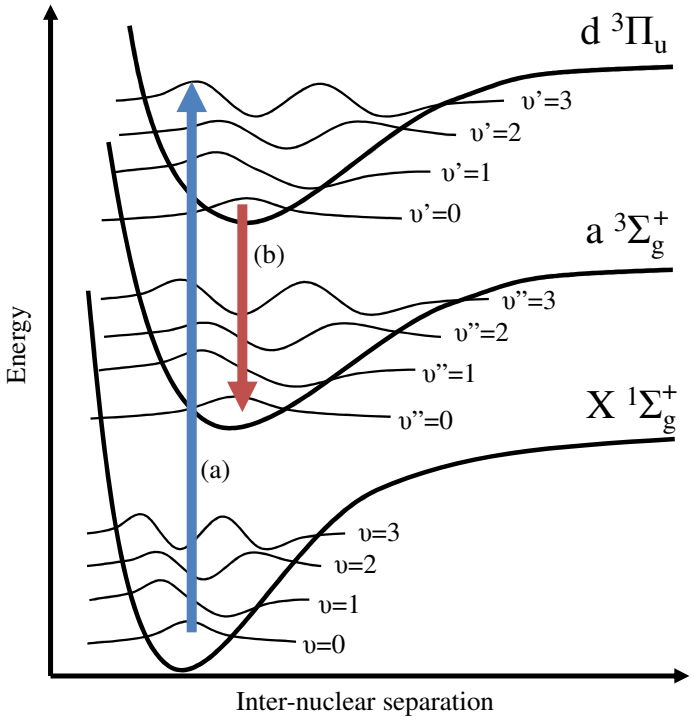

Figure 5.1: Schematic diagram of a Fulcher emission of molecular hydrogen. A molecule in the ground state is excited via an electron impact to a d state (a). Due to the Franck-Condon principle, the excited molecule also occupies a ro-vibrational level, ν. The molecule can decay by emitting P, Q or R-branch Fulcher lines (b).

numbers indicate the symmetry of molecules. Electrons are free to transition between energy levels, subject to certain *selection rules* which limit how much the quantum numbers may change [85]. $\Delta L = \Delta J = \pm 1$ and as long as $L \neq 0$ or $J \neq 0$, then $\Delta L = \Delta J = 0$ is also allowed. Electrons cannot in general jump between atomic multiplets, so $\Delta S = 0$. Finally, molecules must transition according to $u \leftrightarrow g$.

5.1.3 Molecular Spectra

Molecules have additional degrees of freedom in that the relative positions of the nuclei can oscillate. This means each electronic state has a set of vibrational energy levels, labelled with quantum number ν, and each vibrational level has quantised rotational levels, J. These *ro-vibrational* levels are close in energy and can all decay back to the electronic ground state, so one observes vibrational emission *bands* over a small range of wavelengths. In much the same way that decays to specific atomic energy levels form the Lyman and Balmer series etc, molecular emission bands are often named. For example the *Fulcher* band is a well-studied molecular spectrum of hydrogen [86], as shown in Fig. 5.1.

Ro-vibrational transitions also follow selection rules, namely $\Delta\nu = \pm 1$ and $\Delta J = \pm 1$. Emission lines with $\Delta J = +1$ form the so-called *R branch* whereas lines with $\Delta J = -1$ are known as the *P branch*. Although forbidden by the selection rules, $\Delta J = 0$ is possible if the molecule is first electronically excited and then de-excited back down to the ground state via steps through ro-vibrational levels. This phenomenon relies on the *Born-Oppenheimer* principle whereby electronic transitions occur on timescales much faster than the movement of nuclei, so the electronic wavefunctions do not change on the timescale of a transition [87]. In this case the molecule is allowed to transition between levels with $\Delta J = 0$ and such transitions form the so-called *Q branch*. According to the *Franck-Condon* principle, transition from the ground state to an electronically excited state is more likely when the vibrational wavefunctions overlap significantly. Vibrational bands often form a *band head* whereby the individual lines are separated by ever smaller amounts and end up piling on top of each other with a sharp cut-off in wavelength. It is clear that molecular spectroscopy is a broad discipline in itself and includes large subjects like Raman spectroscopy, so the entire range of details cannot be discussed in this thesis. The interested reader should refer to the myriad of papers and books available, for example [87, 88, 89, 90, 91].

5.1.4 Population Models

Equation 5.1.1 states that the emission line intensity scales linearly with the population density, $n(p)$ of the excited state. Unfortunately plasmas are rarely in thermal equilibrium so cannot be described by a simple Boltzmann distribution, making $n(p)$ difficult to estimate. Instead, computational models are required which describe all the (de)population processes based on a variety of plasma parameters; such as the temperatures and densities of all the particle species within the plasma. Since there are a great many energy levels – particularly for molecules – these models quickly become rather complicated. Well documented collision cross sections and rate coefficients are also needed, such as from [92]. The *collisional-radiative* (CR) models used [93] calculate population densities through a balance between the excitation processes, such as collisions, with de-excitation processes such as radiation of photons. The end result of a CR model is the calculation of an effective emission rate coefficient, X_{pk}^{eff} which can be used to determine vital plasma parameters through an extension to Eq. 5.1.1:

$$I_{pk} = n(p)A_{pk} = n_n n_e X_{pk}^{eff}(T_e, n_e, ...) \tag{5.1.7}$$

5.1.5 Measurable Plasma Parameters

The main plasma properties which are required to begin to understand a plasma are the electron density and temperature; the neutral gas density and temperature, and the dissociation degree. Further useful information in an H^- ion source may be the caesium density and the proportion of negative ions. With careful analysis, all of these values may be obtained through optical emission spectroscopy (OES) methods. In plasmas with large volumes, long pulse lengths and multiple diagnostic ports, accurate measurements are easily obtained [94], but the process becomes significantly harder for such a small plasma with low duty cycles such as the ISIS Penning source. Therefore only the most important plasma parameters are measured in this thesis.

The electron density and temperature can be obtained through accurate measurements of line intensities. If the intensity ratio of two lines from the same element is measured, then the direct dependence on particle density is cancelled out in Eq. 5.1.7. Therefore the line ratio is immediately given by the ratio of effective rate coefficients:

$$\frac{I^1_{pk}}{I^2_{pk}} = \frac{X^{eff,1}_{pk}}{X^{eff,2}_{pk}} \,. \tag{5.1.8}$$

This technique may be used when the rate coefficients only depend on the parameter being studied. For example using pure hydrogen gas is unsuitable because there are many competing processes such as the excitation and dissociation of H_2 in combination with atomic emission. Therefore a diagnostic noble gas such as argon or helium should be used as there are no molecular processes to take account of. Well documented and accurate cross sections for these gases are vital. Equally, emission lines are needed with threshold energies close to the high energy tail of the predicted electron energy distribution function (EEDF). Detailed computer modelling investigations using the Atomic Data and Analysis Structure (ADAS) [95] have shown that the emission rate coefficient ratio of the 480.6 nm and 488.0 nm emission lines of singly charged argon ions is sensitive to changes in electron density but not temperature [94]. With n_e determined from this line ratio and n_{argon} known from the measured flow rate of argon injected, T_e may be calculated through Eq. 5.1.7 by measuring the intensity I_{pk} of an emission line with a well documented X^{eff}_{pk}. The 750 nm argon line is suitable for this purpose. Note that it is critically important to have a properly intensity-calibrated spectrometer to give a valid measurement of I_{pk}.

This rather complex use of a diagnostic gas, rate coefficients and ADAS modelling is necessary because of the expected parameter space of the Penning ion source plasma. It is likely to be far from local thermal equilibrium (LTE) and is in an intermediate region whereby simple corona models (for very low density plasmas) and Saha-Boltzmann statistics (for very high temperatures and densities) are not valid. For example hot, dense plasmas ($T_e > 5$ eV, $n_e > 1{\times}10^{21}$ m^{-3}) may have their electron density evaluated by comparing the H_β emission line to tabulated Stark-broadening profiles [83]. Similarly, their electron temperature may be determined from the statistical weights and transition probabilities via the Saha-Boltzmann equation [82]. Employing these methods in an ion source, as in [96, 97, 98], gives invalid results, so more advanced argon studies are mandatory.

The gas temperature T_{gas} is determined from the Doppler broadening of the Balmer H_α hydrogen emission line and Eq. 5.1.4. This parameter may be inserted into the ideal gas equation

$$n_{gas} = \frac{P_{pulse}}{k_B T_{gas}} \tag{5.1.9}$$

to find the gas density. In a system such as the ISIS Penning ion source plasma, which uses pulsed gas injection, care must be taken to get an accurate measurement of the pressure: see Section 5.2.5.

The degree of molecular hydrogen dissociation, R_{dis} is an important parameter to study as it affects the dominant creation process for H^- ions. A high proportion of atoms tends to favour surface-production mechanisms; a high proportion of molecules favours volume-produced H^-. Detailed ADAS simulations show that the ratio of emission rate coefficients of atomic H_γ and molecular $H_{Fulcher}$ is almost independent of electron density and temperature [94]. Therefore measurement of the emission line ratio $H_\gamma/H_{Fulcher}$, combined with Eq. 5.1.8 and combinative-ratiative (CR) models, yields the dissociation degree n_H/n_{H_2}. Note that the entire integrated intensity of the Fulcher band spectrum must be evaluated from 600 nm to 640 nm. Therefore careful analysis and removal of extraneous lines is required [99]. A summary of the measurement techniques discussed is given in Table 5.1.

5.2 Apparatus

Two broad categories of optical spectrometer can be used for optical emission spectroscopy. For a quick overview of the entire emission spectrum, a *survey spectrometer*

Table 5.1: OES techniques required to measure specific plasma parameters.

Parameter	**Measurement Method**
Dissociation Degree, R_{dis}	$\frac{I(H_\gamma)}{I(H_{Fulcher})} \rightarrow \frac{X(H_\gamma)}{X(H_{Fulcher})} \rightarrow$ CR Model $\rightarrow R_{dis} = \frac{n_H}{n_{H_2}}$
Electron Density, n_e	$\frac{I(Ar_{480.6})}{I(Ar_{488.0})} \rightarrow \frac{X(Ar_{480.6})}{X(Ar_{488.0})} \rightarrow$ ADAS Model $\rightarrow n_e$
Electron Temperature, T_e	$\left.\begin{matrix} I(Ar_{750}) \\ n_e \\ n_{Ar} \end{matrix}\right\} X(Ar_{750}) \rightarrow$ ADAS Model $\rightarrow T_e$
Atom Temperature, T_H	$\Delta\lambda(H_\alpha) \rightarrow$ Doppler Broadening $\rightarrow T_H$
Atom Density, n_H	$\left.\begin{matrix} T_H \\ P_{pulse} \\ R_{dis} \end{matrix}\right\}$ Ideal Gas Law $\rightarrow n_H$

with low wavelength resolution of the order of 1.0 nm is an inexpensive option. With a CCD detector recording a wide wavelength range and giving continual output to a computer, survey spectrometers may be used to see impurities which might otherwise be overlooked and monitor long-term changes to the main plasma emission lines. For precise measurements of emission line widths of the order 0.1 nm, a much higher resolution instrument is needed. A suitably sized *optical monochromator* using Czeny-Turner optics [87] and a diffraction grating may achieve resolutions of the order 0.01 nm (10 pm), which is sufficient to record several samples across a narrow emission line, and thus determine its line-width accurately. The term monochromator stems from the idea that these high precision instruments only pass one very narrow band of wavelengths to the detector.

A StellarNet EPP2000 survey spectrometer and an Horiba Jobin Yvon FHR1000 monochromator were used to measure a wide range of plasma properties of the VESPA Penning H^- ion source. The survey spectrometer could measure the entire optical spectrum from 200 to 1100 nm with a refresh rate of 1 ms at a resolution of 0.5 nm. The monochromator had a turret to select from two diffraction gratings enabling measurements of the spectrum over the same range as the survey spectrometer, but at a resolution of 12 pm. A demonstration of the difference in resolving power of the two spectrometers is given in Fig. 5.2.

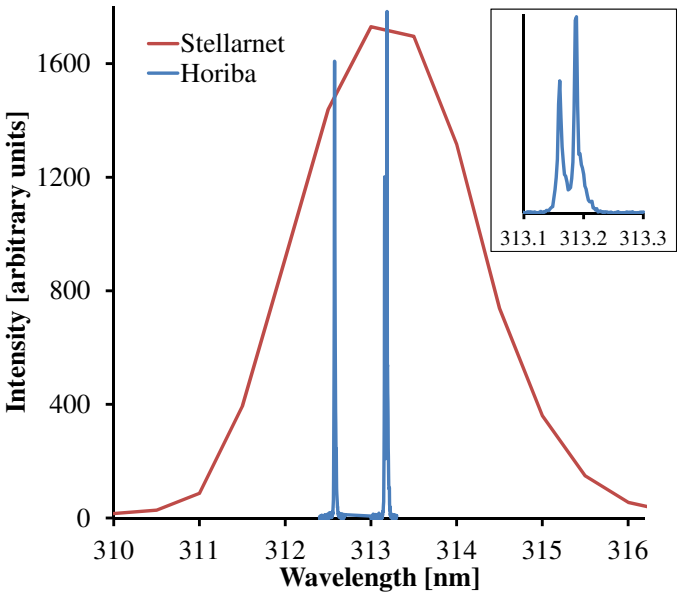

Figure 5.2: Measurement of the atomic emission lines near 313 nm in a mercury calibration lamp. Red line indicates measurement using the survey spectrometer. Blue line indicates measurement with the monochromator. Inset: the monochromator had 50 times greater resolution and easily resolved the doublet at 313.156 nm and 313.184 nm.

The monochromator had two exit ports so a CCD camera and a photomultiplier tube (PMT) could be used simultaneously. The CCD would enable a range of wavelengths to be recorded from the grating, with each pixel on the CCD recording a specific wavelength; so in principle a whole emission line could be recorded in one shot. However with the light source in this application being a pulsed plasma, it was felt that high time response was more important, so only a PMT was used in this measurement campaign. PMTs directly record the incoming photons as a voltage so are extremely quick and relatively inexpensive compared to an image-intensified fast CCD camera.

Direct line of sight into the plasma was available in the VESPA configuration by means of an optical window on the vacuum vessel. This was in line with the beam emission aperture of the ion source plasma electrode. Due to space constraints, the cumbersome monochromator was located remotely from the vacuum vessel and light was coupled to it via a multimode optical fibre. The small (0.6×10.0) mm^2 emission aperture slit and the large 570 mm distance from the aperture to the window resulted in a rather small image captured by the fibre. Therefore a telescoping arrangement of two short focal-length lenses was used to magnify the image so the entire fibre

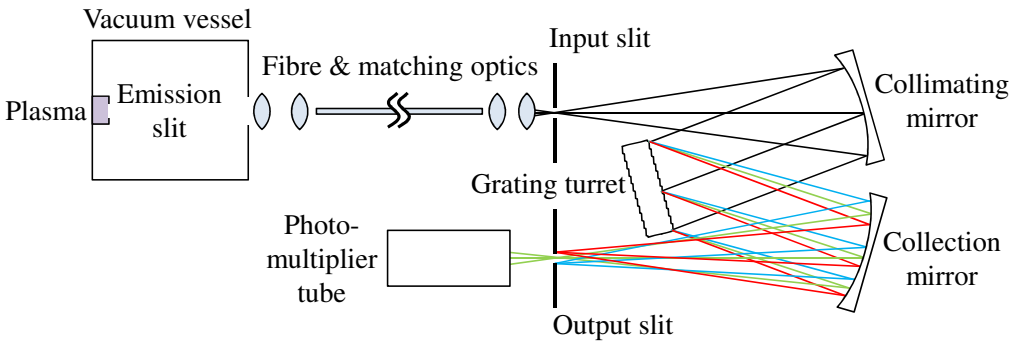

Figure 5.3: Czeny-Turner monochromator set-up.

core was illuminated. The *numerical apertures* of the fibre and monochromator were different, which meant not all the light emitted by the fibre would be transported through the monochromator optics. To ensure maximum transmission, or *etendue*, matching optics consisting of two lenses were installed between the output end of the fibre and the entrance slit of the monochromator. This took the divergent light from the fibre and focussed it through the entrance slit. A schematic of the entire optical arrangement is given in Fig. 5.3.

5.2.1 Wavelength Resolution

The ultimate resolution of a monochromator is determined from a number of factors, primarily:

- Focal length from collimating mirrors to grating
- Grating groove density
- Maximised etendue using input matching optics
- Size of entrance and exit slits

The FHR1000 was chosen as it had a relatively long one-meter focal length and stepper-motor controlled entrance and exit slits, adjustable to 10 μm. Gratings ruled at 1200 lines per mm and with blaze wavelengths of 330 nm and 500 nm gave high resolving power over a sufficiently large spectral range. Higher resolution could be achieved with higher grating groove density, but at the cost of scanning range.

To maximise both the light intensity collected by the PMT and the wavelength resolution, a compromise was required. On the one hand, since the light source was so small, the fibre core diameter should be large enough to capture all the light

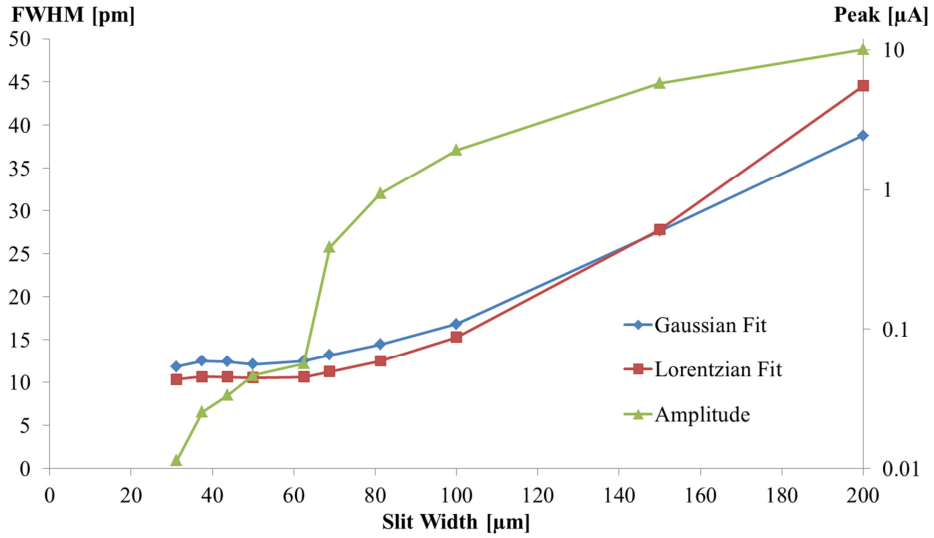

Figure 5.4: Full width at half maximum and peak amplitude of mercury 763 nm emission line as a function of monochromator input and output slit widths.

available. On the other hand, the best resolution was achieved when the light was focussed tightly enough to pass fully through the entrance slit: easier to achieve with a small fibre core diameter. In practice, though, to achieve the desired resolution for this application required the entrance and exit slits to be between 30 μm and 100 μm, which was less than the core diameter. Therefore the ultimate resolution was dominated by the slit setting, not the fibre used. Using a mixed mercury and argon wavelength calibration lamp, which had a large number of narrow emission lines in the optical range, the resolution of the monochromator was determined, as shown in Fig. 5.4.

Reducing the slit separation increased the resolution of the instrument until it either saturated at its maximum resolution or it reached the natural line width of the measured emission line. The wavelength-calibration lamp was a very low power, low temperature light source so the natural line widths were significantly smaller than those measured. Therefore it can be concluded that the monochromator's maximum measured resolution was 10 pm. Saturation to this limit began for slit widths smaller than 100 μm. However Fig. 5.4 shows that the difference in measured signal from 30 μm to 100 μm slits was a factor of 100. Therefore to benefit from an increased signal-to-noise ratio, the slits were kept at 100 μm in all subsequent measurements.

5.2.2 Absolute Intensity Calibration

As mentioned in Section 5.1.5, the absolute intensity of the 750 nm argon emission line is mandatory to determine the electron temperature: photomultiplier voltage, amplifier current or 'counts' are insufficient. Therefore the OES system was absolutely calibrated using a precision Avantes Avalight-DH-S-BAL mixed deuterium-halogen calibration lamp. This had a certificated, calibrated output spectral radiance in units of $W\ m^{-2}\ nm^{-1}$, measured 50 mm from the output hole. Placing the calibration lamp at the same distance from the window as the ion source emission aperture (570 mm) and conserving the solid angle, the light was measured on the PMT through the entire optical set-up shown in Fig. 5.3. Dividing the measured amplified PMT signal (in μA) by the known spectrum gave a calibration conversion factor. As long as the set-up was unchanged, the measured signal could thus be converted into spectral intensity, I_{pk} in units of $photons\ m^{-3}\ s^{-1}$, which may then be used in Eq. 5.1.7 to determine the effective emission rate coefficient.

5.2.3 Triggered Data Acquisition

The monochromator was shipped with a 'SpectrAcq2' data acquisition (DAQ) hardware module and control software called 'SynerJY'. When testing the DAQ with a pulsed plasma as a light source, it became clear that the combination of SpectrAcq2 and SynerJY was fundamentally limited since neither could be triggered to acquire data at a specific instant in time. The integration window within which signal was captured from the PMT was not tied to the plasma pulse so it was not guaranteed that a plasma pulse was within the window. Therefore the signal would fluctuate significantly dependent on whether a light pulse was captured or not. Emission lines thus became very noisy, making it difficult to fit Gaussian or other functions and hence determine line widths accurately. The control and DAQ code was re-written from scratch in LabVIEW by the author such that triggering could be enabled. An existing Microstar Laboratories DAP840 data acquisition board was used to capture data from the PMT via a Stanford Research Systems SR570 current pre-amplifier. The basic workflow of the LabVIEW code was as follows:

1. Initialise communications with monochromator and SpectrAcq2. Monochromator self-calibrates grating position.

2. Enable photomultiplier and set monochromator slit separation

3. Move grating to starting wavelength and readout position whilst moving

4. Begin wavelength scan iteration
   (a) Move to next wavelength step
   (b) Readout wavelength position
   (c) Initialise DAP840 data acquisition module:
      i. Initiate data communication pipes from PC to DAP840
      ii. Flush any existing data in pipes
      iii. Input DAQ commands, including triggering
      iv. Begin DAQ
   (d) Read required number of samples, average over several plasma pulses and pass to main code loop
   (e) Flush and close DAQ pipes
5. Plot light intensity as a function of time in the plasma pulse
6. Add a point to the emission line plot by taking a sample mid-way through the light pulse and plotting that value for each wavelength
7. Loop to next scan position

The LabVIEW front-panel and a typical data set is shown in Fig. 5.5. A comparison of H_α emission line measurements using the SynerJY and LabVIEW DAQ codes is shown in Fig. 5.6. The improved line profile allowed more accurate curve fitting.

5.2.4 Argon Injection

As discussed in Section 5.1.5, argon is a suitable diagnostic gas to help characterise plasma parameters. Argon was bled into the ion source via a mass-flow monitor, a needle valve to control flow, a shut-off valve and a tee into the hydrogen inlet line. The pressure was set on the argon bottle regulator such that a positive flow was just achieved through the mass-flow monitor. This was to ensure hydrogen did not flow back into the argon line, but that the hydrogen-plus-argon pressure was still positive into the ion source rather than back into the hydrogen bottle. It was assumed that the hydrogen and argon gases were mixed fully at the piezoelectric pulsed valve just before entry into the ion source. Using the needle valve, the argon flow rate was adjusted to 0.3 ml/min: approximately 2% of the hydrogen flow.

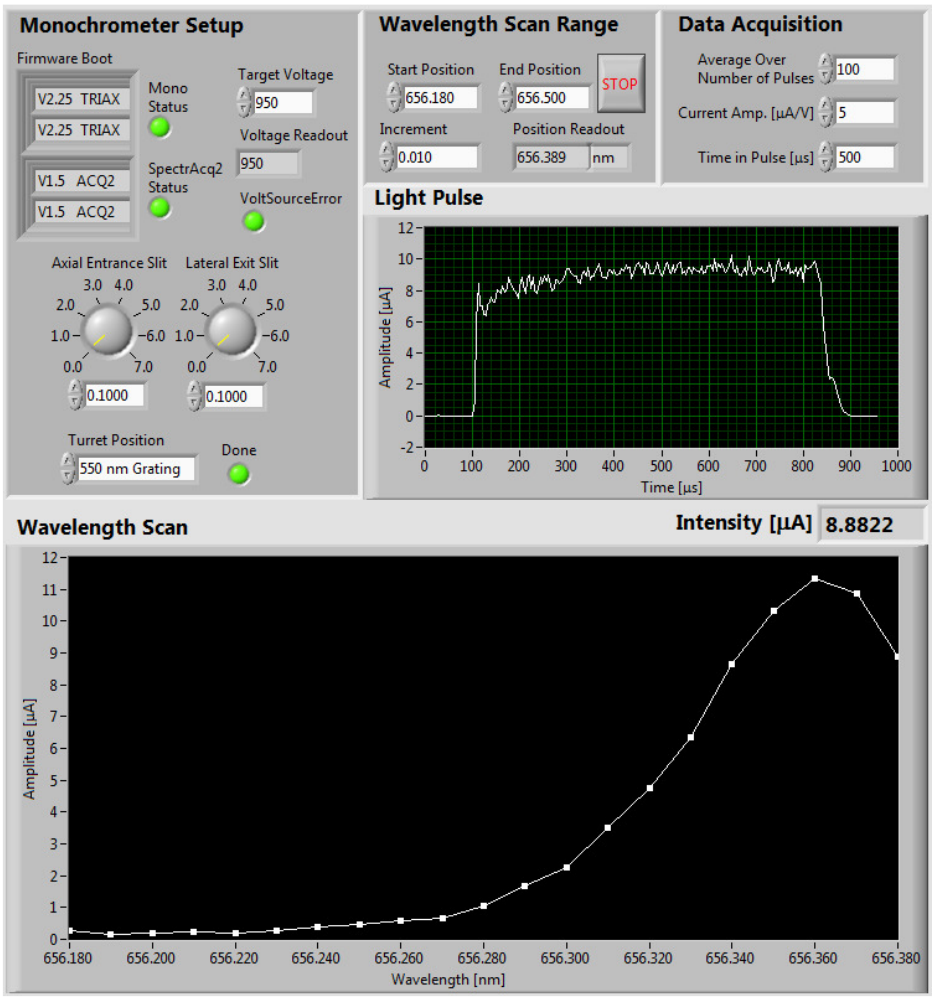

Figure 5.5: Front-panel of the LabVIEW monochromator control and analysis software. Displayed image taken part-way through a scan of the H_α emission line from the VESPA pulsed arc plasma.

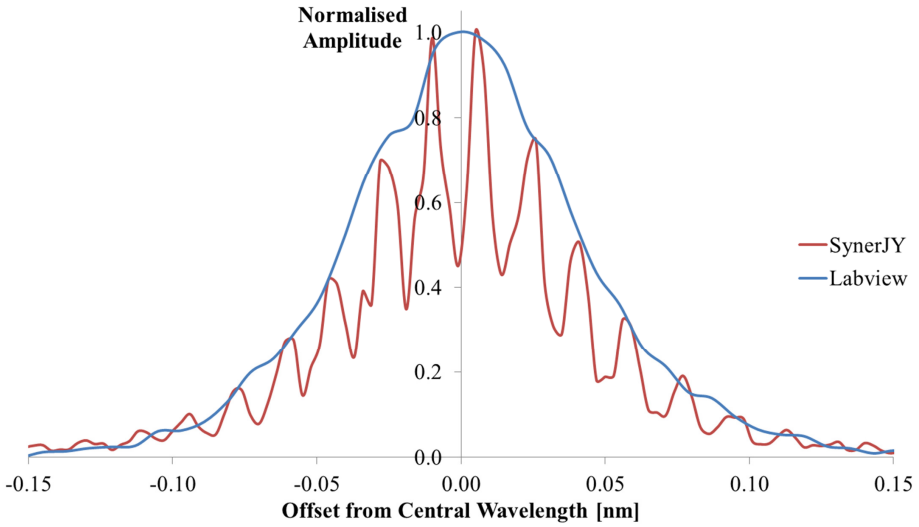

Figure 5.6: Comparison of the SynerJY data acquisition software shipped with the monochromator and the purpose-built triggered LabVIEW code.

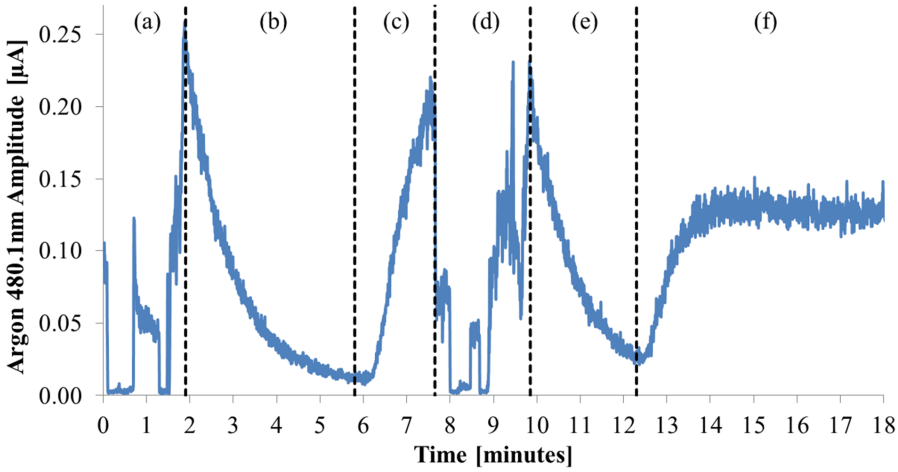

Figure 5.7: Log of argon optical emissions during commissioning. A pulsed arc which had collapsed when argon was injected (a) was recovered and stabilised with the argon feed closed (b). When the arc was stable and all the argon gas evacuated from the plasma volume, argon was again injected (c), as registered by the increased emissions. At some point, the amount of argon inside the plasma was again sufficient to collapse the arc (d). After again recovering the arc with argon turned off (e), the argon was injected for a third time, but at the minimum possible flow rate (f). This time, the argon flow rate was low enough that the pulsed arc survived stably as usual.

Argon was chosen as a source of well-known emission lines because it is inert and should not affect the plasma in any way. However it was found that the ion source was significantly more difficult to operate when argon was injected. When running the source up from cold, it took over twice as long to reach operational temperature and a higher caesium flow was required. Pulsed mode of plasma operation was even more difficult, with a previously well-running pulsed plasma being extinguished within minutes of argon being injected, as shown in Fig. 5.7.

With long-term operational experience on the ion source, it is known that there is a balance between hydrogen and caesium partial pressures in the ion source. For example, when the hydrogen flow rate is adjusted upward, the operational characteristics of the pulsed plasma sometimes appear as if the caesium level has been reduced. One possible explanation for the drastic and immediate deterioration of performance with the introduction of argon, therefore, was that the argon affected the partial pressure balance and hence resulted in less caesium entering the source. Alternatively, maybe the argon itself was in some way affecting the caesium deposition on the molybdenum cathode surfaces, despite being supposedly inert.

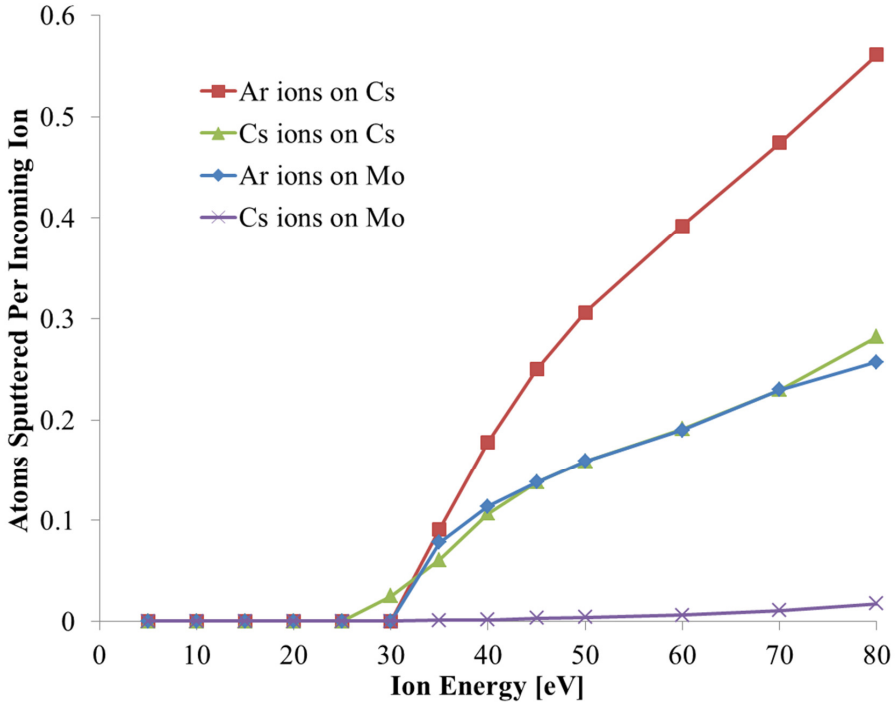

Figure 5.8: SRIM calculation of the number of caesium or molybdenum atoms sputtered off the cathode by incoming caesium or argon ions. Sputtering only occurs above a certain threshold energy, which is generally inversely related to the incoming ion mass.

The Stopping and Range of Ions in Matter (SRIM) software [100] was used to determine the effect of argon ions impacting on the caesium-coated molybdenum cathode. The sputtering rates of caesium and molybdenum surfaces as a function of impacting argon and caesium ions of various energies are shown in Fig. 5.8.

It is clear that argon – despite having only a third of the atomic mass of caesium – sputters significant amounts of cathode material: double the amount of caesium atoms are removed by argon ions hitting the surface, than by caesium ions themselves. Similarly, an order of magnitude more molybdenum is sputtered by argon than by caesium. Hydrogen ions were also tested in the simulation, but do not sputter material below an impact energy of around 1 keV. Argon sputters cathode material aggressively; but it is unclear whether it was the destruction of the caesium monolayer on the cathode, or the poisoning of the plasma by sputtered molybdenum, which affected ion source operation. Despite these difficulties, by setting the argon flow to the absolute minimum, as shown in Fig. 5.7f, useful measurements were made.

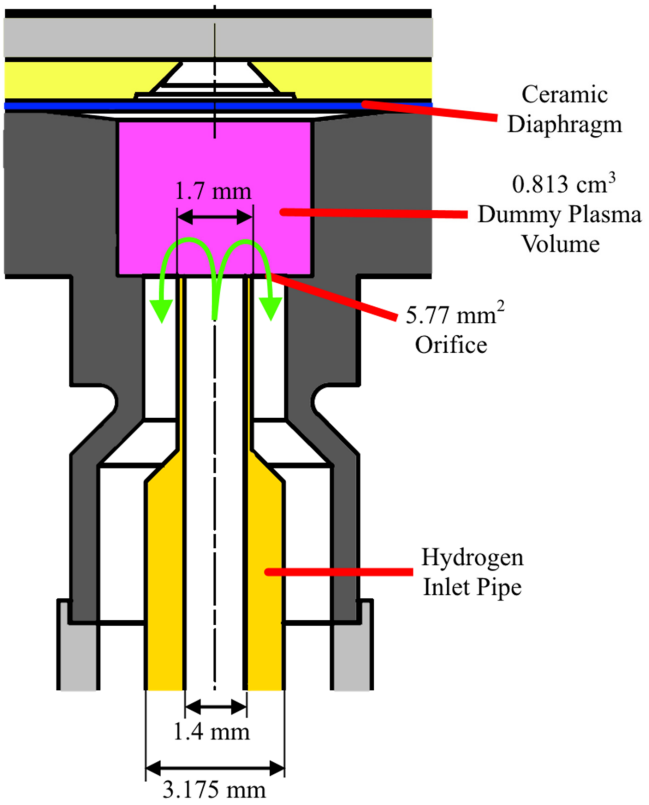

Figure 5.9: Cross section of the internal components of a fast capacitive diaphragm pressure gauge modified to simulate a Penning ion source plasma volume.

5.2.5 Pulsed Gas Pressure

The hydrogen flow rate and pressure were difficult to quantify. Because the plasma was pulsed, it was inefficient to inject hydrogen continually into the discharge region: it was a waste of gas and put undue stress on the vacuum pumps. Therefore the hydrogen was pulsed via a piezoelectric valve. The pulse amplitude of the piezo was varied on the gas control crate, which resulted in a set average pressure. The time-averaged vacuum pressure was measured approximately 10 cm away from the ion source at the vacuum vessel wall. The time-averaged gas flow was measured by a mass flow meter attached to the hydrogen bottle. The gas control crate was a closed loop system whereby the piezo amplitude – and hence the mass flow rate – was adjusted to ensure the set pressure was kept constant. The aim being that if the vessel pressure was constant, then the pulsed pressure (and hence particle density) inside the ion source should be constant. It was very difficult to determine the hydrogen flow rate during the pulse and hence what the pressure was inside the discharge region at the time of the plasma pulse.

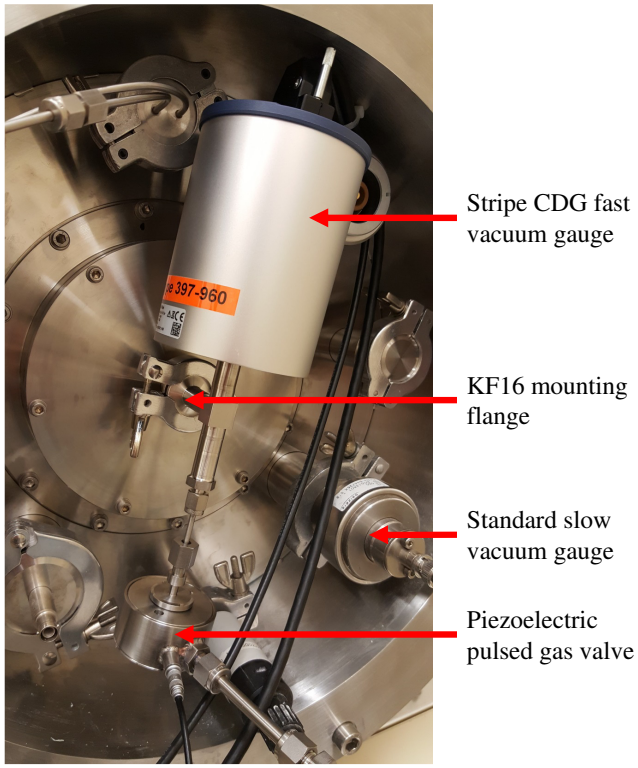

Figure 5.10: Photograph of the custom capacitance diaphragm gauge installed on the VESPA where the ion source was usually mounted.

A novel method was devised to estimate the pulsed pressure inside the plasma chamber. Inficon's Stripe Capacitance Diaphragm Gauge (CDG) shown in Fig. 5.9 is typically used in chemical vapour deposition and other thin-film applications. Precise control of layer thickness is possible by measuring vacuum pressure (related to the number of atoms deposited on a substrate) on fast timescales. The CDG thus acts as a closed-loop control in those kinds of application: switching off the ion source when the desired layer thickness has been reached. The CDG has a reponse time less than 1 ms at pressures down to 6×10^{-2} mbar and has an upper measurement range of 13 mbar. Sampling speed is limited by the mean-free-time of particles impacting the sensor diapragm. As the CDG is typically used in applications involving corrosive particles, a complex baffle system is installed in the connection flange to prevent particles travelling to and depositing on the sensor.

A modifed Stripe CDG, shown in Fig. 5.10, was proposed by the author as an effective way of estimating the pulsed pressure in the ion source plasma chamber. Although the CDG was best-in-class for speed, 1 ms sampling time was still rather

long compared to the 200 μs input gas pulse of the VESPA ion source. Similarly, since the ion source operated at 50 Hz repetition rate, the CDG could only achieve twenty sample points per gas pulse. However the gas pulse was smeared out in time as it travelled from the piezo valve to the plasma chamber, and even a crude time-sampled pressure measurement was significantly more accurate than a time-averaged measurement located far away in the vacuum vessel. Therefore the CDG was the closest representation of reality possible to achieve on the VESPA Penning ion source.

With the baffle removed, hydrogen gas was fed into the modified CDG from a standard ISIS piezo valve via a $^1/_8''$ pipe. The hydrogen accumulated in a volume in front of a ceramic diaphragm. The diaphragm elastically deformed when gas pressure was applied to one side. The other side had a pick-up which measured the deformation via a change in capacitance and output a corresponding voltage. The voltage was calibrated to be linear with applied pressure. The volume enclosed by the pipe, diaphragm and walls was approximately four times larger than the plasma chamber inside the standard ISIS Penning ion source and was the smallest manufacturable volume. Although not a perfect replica, it was close enough for a reasonable extrapolation; especially to future scaled-up ion source designs [74]. The outside diameter of the pipe tip was reduced such that an annular orifice was formed with the same area as the slit-shaped ion source outlet aperture. The CDG was attached to the vacuum vessel via a KF16 flange to pump away the hydrogen and allowed two hours to stablise thermally for accurate low-pressure measurements.

The closed-loop nature of the ion source gas control crate is apparent in Figs. 5.11 and 5.12, where the piezoelectric gas valve repetition rate was varied. In normal closed-loop operation, the piezo's pulse amplitude was adjusted automatically by the gas control crate to ensure that the average vessel pressure was kept constant whatever the repetition rate. This meant that the peak pulsed pressure scaled inversely proportional to repetition rate; i.e. halving the rep. rate doubled the peak pressure. When in open-loop mode, the piezo amplitude was directly controlled by the user. At a fixed set amplitude, the same peak pressure occurred during each gas pulse regardless of the rep. rate. Therefore open-loop operation at low rep. rates resulted in a reduced average pressure and gas flow rate. Note however that at rep. rates higher than 6.25 Hz, there was insufficient time between pulses for the gas to be evacuated fully from the plasma chamber. Therefore the residual gas was added to the next incoming gas pulse, resulting in an increased peak pressure. At 50 Hz,

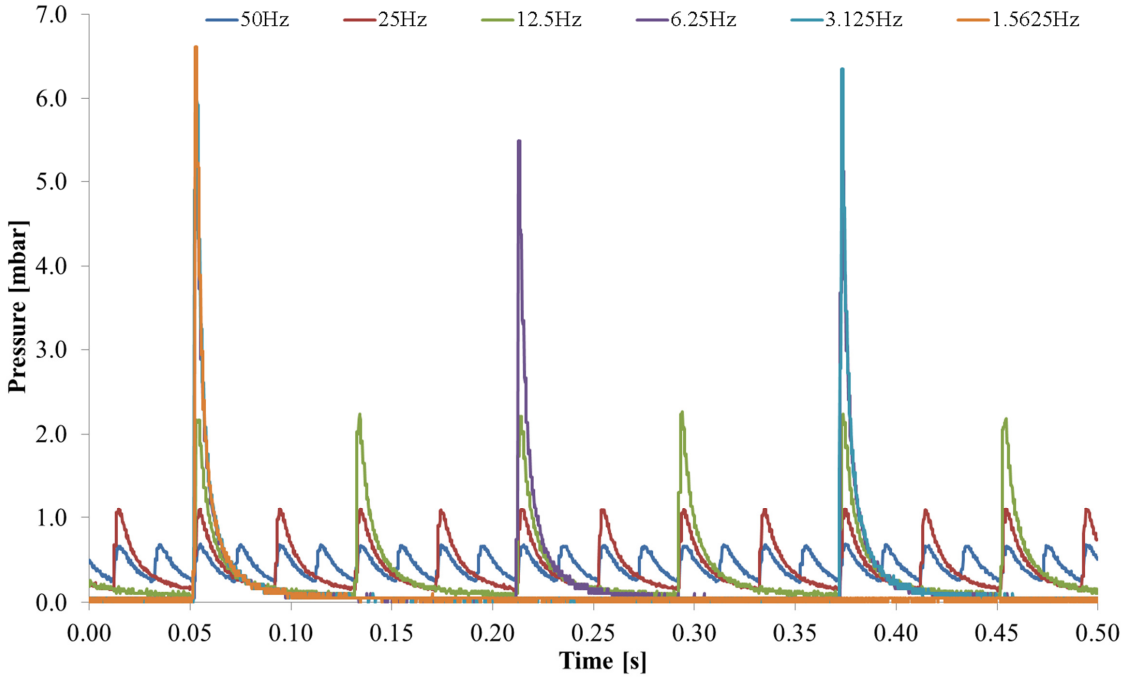

Figure 5.11: Variation in pressure as measured by the CDG, with the gas control crate operated in closed-loop mode.

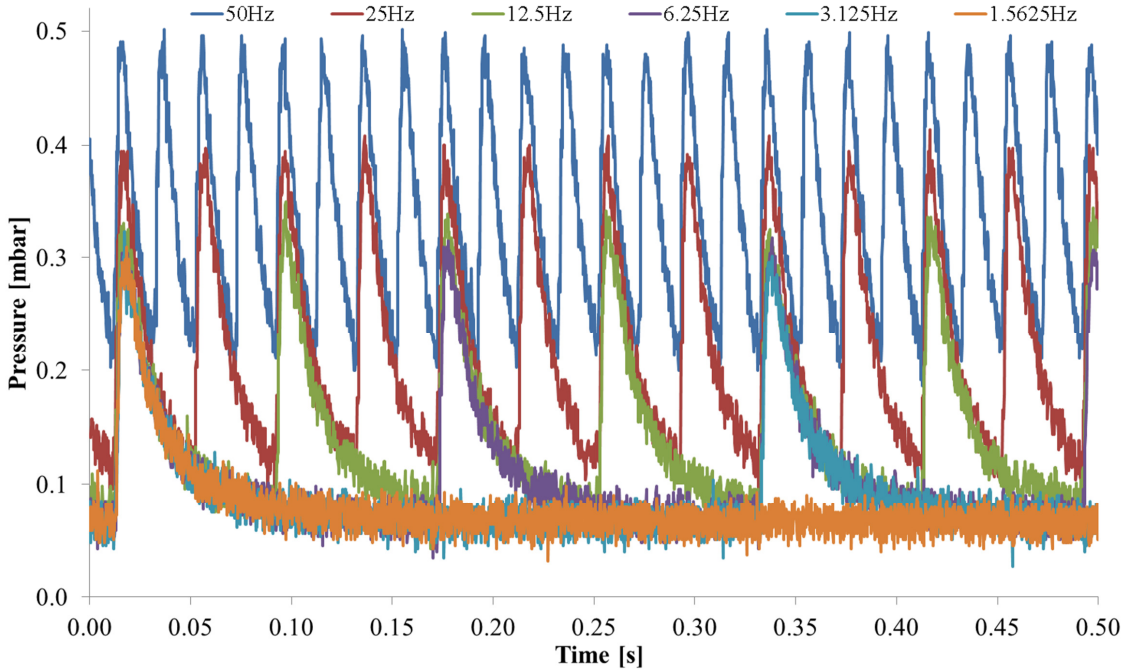

Figure 5.12: Variation in pressure as measured by the CDG, with the gas control crate operated in open-loop mode.

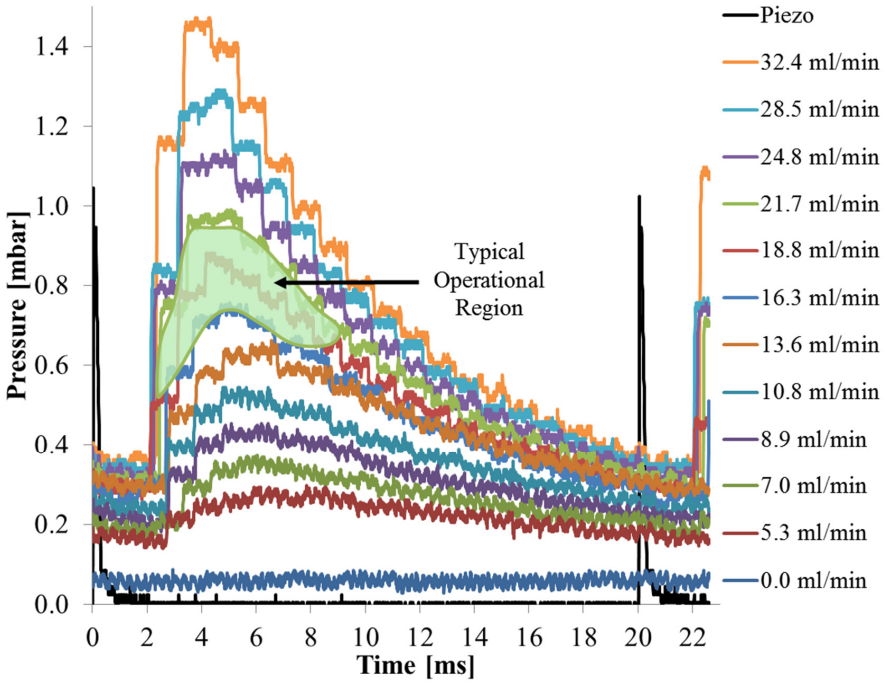

Figure 5.13: Variation of pressure with time after the piezo gas pulse for a range of average hydrogen flow rates.

the peak pressure was 67% higher than at 6.25 Hz due to the residual gas. Although open-loop operation was interesting in its own right, the remainder of the fast pressure measurements were taken in closed-loop mode, as that was how the ion source gas control crate was operated normally.

At a constant 50 Hz repetition rate and 100 μs piezo pulse length, the set-point average pressure on the gas control crate was adjusted and the average hydrogen flow rate recorded. There was a direct linear relationship between average pressure and flow rate. Since flow rate is a somewhat more useful quantity than the average vacuum vessel pressure, the time variation of pressure as measured by the CDG is given in Fig. 5.13 for a range of flow rates. The 1 ms sampling rate of the CDG is visible as a sequence of steps in each plot; nevertheless the overall pressure profile was well resolved. Also evident is the time delay between the piezo and pressure pulses caused by the time taken for gas to travel from the piezo to the CDG. The peak pressure varied linearly with average flow rate. The green area marked on Fig. 5.13 shows the region of flow rates and pressures in which the ion source was typically operated. As such, a reasonable estimate for the peak pressure inside the ion source plasma was 8×10^{-1} mbar. This was the first accurate estimate of the pressure in over 30 years of ion source operation.

5.3 Optical Emission Spectroscopy Measurements

In ordinary operation, the ion source has a number of parameters which can be adjusted: the arc current; the hydrogen and caesium flow rates; the Penning magnetic field, and the cathode, anode and body temperatures. Unfortunately, because of the argon difficulties discussed in Section 5.2.4, only the arc current could be adjusted in the OES campaign without harming plasma stability.

5.3.1 Emission Intensity

A typical H_α light pulse is shown in Fig. 5.14. The arc power supply operated in current-limited mode, so the arc voltage varied to maintain a set current. The light intensity tended to follow the arc voltage. However there was a step-change decrease in hydrogen emissions during the beam extraction pulse, indicating a depletion of H^- ions from the plasma; this is also seen in ion sources for fusion [94]. Interestingly, even in the quiescent part of the discharge pulse, the emitted light was rather noisy, often with 10% fluctuations evident. Optical fluctuations were completely random, unlike the normal periodic arc noise discussed in Section 4.3.1. This may indicate the presence of plasma turbulence, which is discussed in Section 5.3.2.

Figure 5.15 shows interesting features of caesium optical emissions. When the arc was extinguished, Cs^+ ions were able to de-excite and subsequently re-combine with electrons so there was a spike of Cs^+(460 nm) emission during the neutralisation process. This measurement agrees well with the spike seen when monitoring caesium flux escaping an ion source using a surface ionisation detector [101]. Also, it can be seen that the caesium emission intensity varied during the arc pulse: falling at low arc currents and rising at higher currents. This may be explained by considering the stability of the caesium monolayer on the cathode surface. At low arc currents, both the cathode temperature and sputtering rate were lower, so caesium was able to continue accumulating on the cathode during the arc pulse. The plasma became depleted of caesium, so optical emissions decreased. At higher arc currents, the rate of desorption and sputtering was higher from the hotter cathode; more Cs^0 atoms entered the plasma to be immediately ionised, leading to increasing Cs^+(460 nm) emission during the arc pulse. This is an independent confirmation of the theory that the cathode caesium balance is compromised at high duty-factor operation, leading to beam current droop [102, 103]. It also implies that 30 A may be an ideal setpoint.

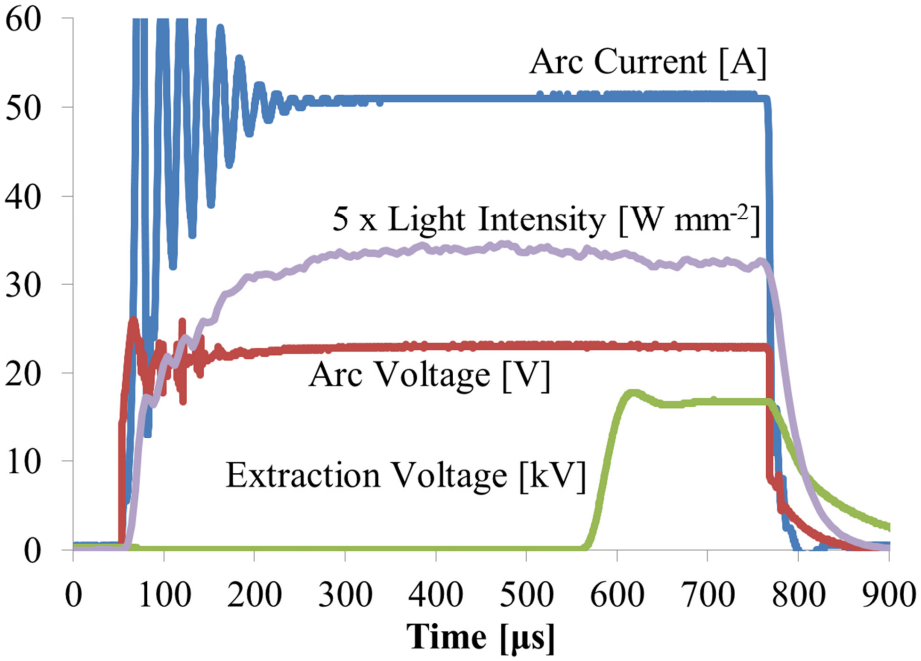

Figure 5.14: Typical arc, extraction and H_α light pulses for a 50 A arc. Note that the light intensity has been scaled by a factor of five for clarity.

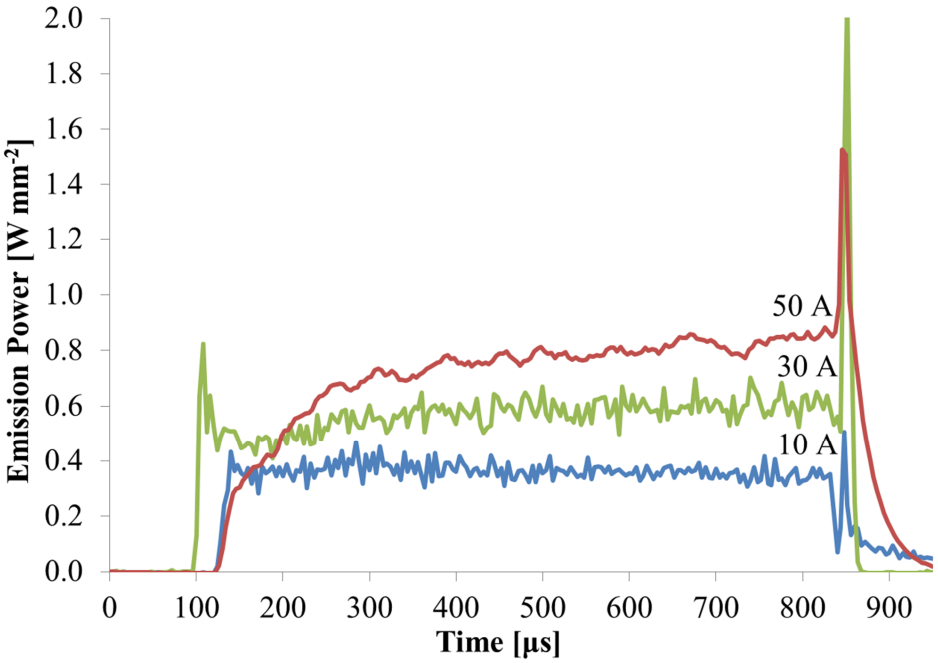

Figure 5.15: Cs^+(460 nm) emissions at different arc current set-points.

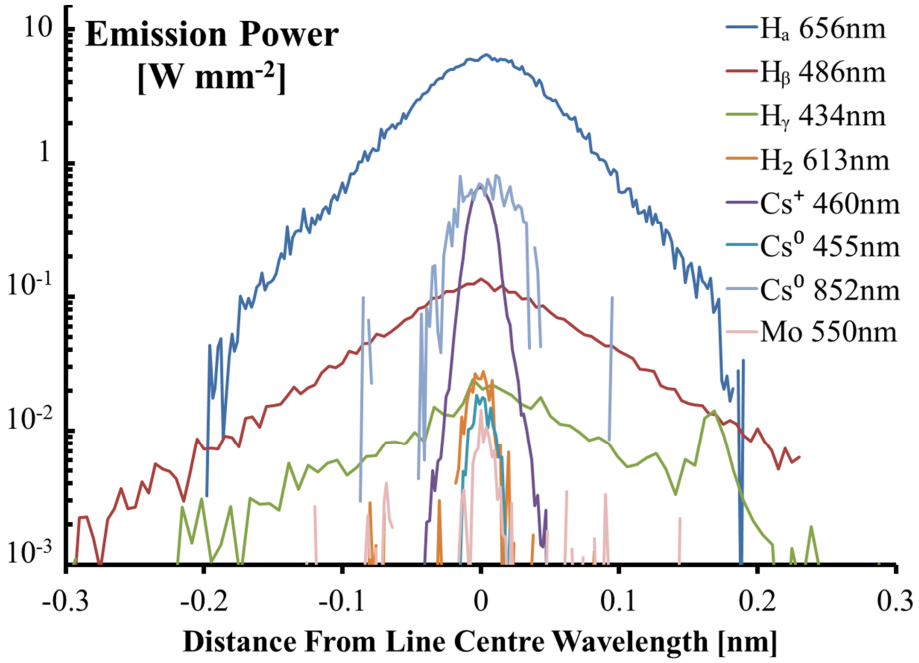

Figure 5.16: Comparison of the absolute emission line intensities and widths in the VESPA 50 A arc plasma.

The absolute emission power of various principal lines in a 50 A arc is shown in Fig. 5.16. Plotted on a log scale, this summarises the relative intensities and widths of the most important lines under study. The hydrogen lines were much more affected by Doppler broadening than heavy caesium atoms, as predicted by Eq. 5.1.4. Caesium dominates all emissions except for the H_α, showing that it had a high degree of ionisation due to its loosely bound valence electron. Note that the poor signal-to-noise on the Cs^0(852 nm) line was due to the low infrared transmission of the vacuum window. Fig. 5.16 also shows how important it was to have a high resolution monochromator to measure line widths accurately on the order of 0.1 nm.

5.3.2 Density and Temperature

Using the techniques summarised in Table 5.1, figures 5.17 and 5.18 show how the gas and electron density and temperature varied with arc current, measured at the end of the arc pulse. A pulsed gas pressure of 8×10^{-1} mbar was assumed, as measured in Section 5.2.5. As the arc current was increased, more atoms and molecules were ionised so the neutral gas density decreased whilst the electron density increased. Provided the arc was operating in a reasonably comfortable and quiescent regime (which occurred above about 10 A of arc current), the densities seemed to follow square-root relationships with arc current. Because of the high gas pressure in the

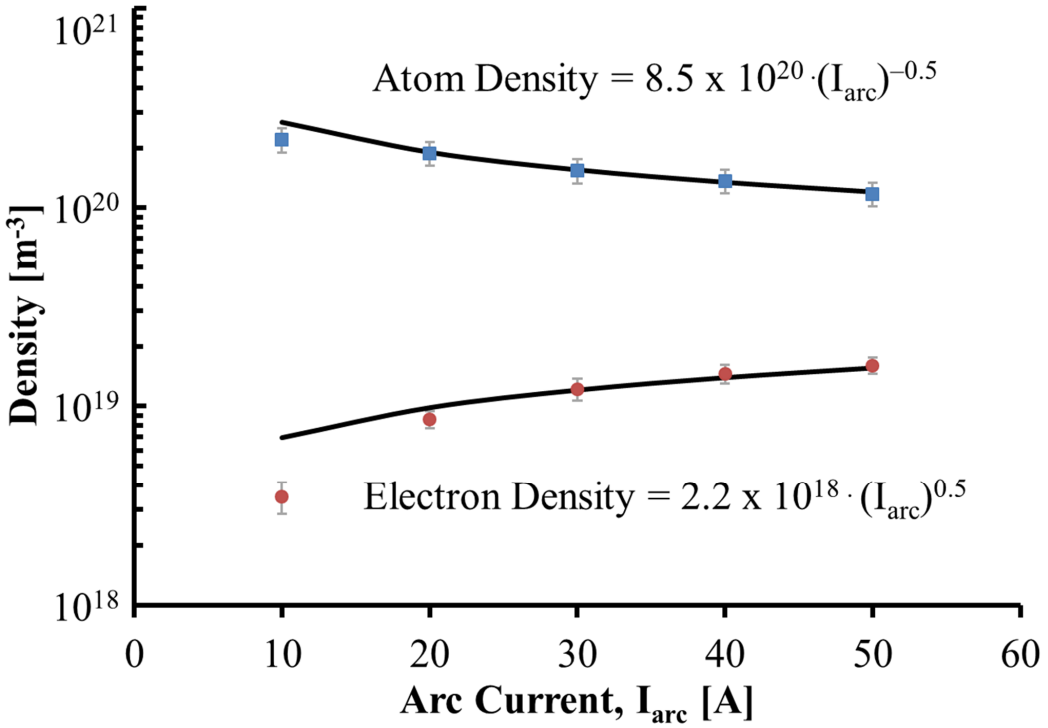

Figure 5.17: Atom and electron density as a function of ion source arc current.

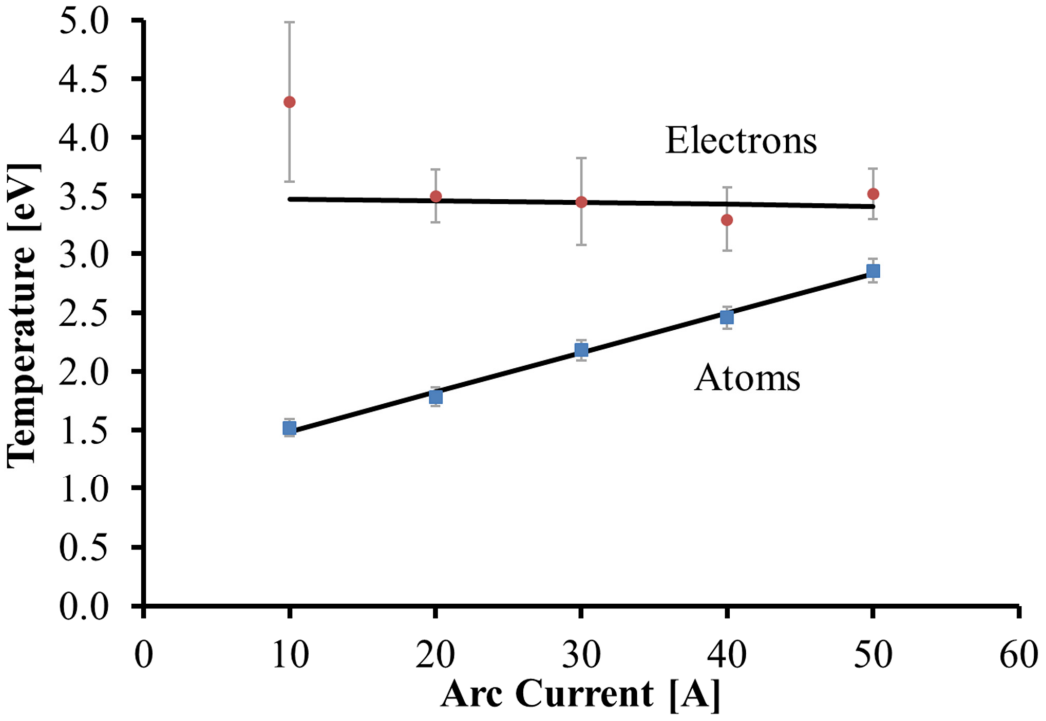

Figure 5.18: Atom and electron temperature as a function of ion source arc current.

Penning ion source (8×10^{-1} mbar compared to 3×10^{-3} mbar in large volume sources [104]), the electron and gas density were over an order of magnitude higher than in RF ion sources.

The electron temperature stayed fairly constant at around 3.5 eV and was greater than the atom temperature, as is the normal case in most plasmas [105]. However the atom temperature increased linearly with arc current and appeared to meet or even exceed the electron temperature at high arc currents. This finding agrees with other measurements made of Penning ion sources [97, 106]. There are three possible explanations for this phenomenon: first, with the degree of ionization increasing with arc current, it may be that the remaining neutral atoms had, on average, a higher kinetic energy. Measurements of the particle energy distribution functions are required to validate that theory, which may the subject of future work. Similarly, a procedure is needed to operate higher arc currents stably in the presence of argon, to ascertain whether the atom temperature eventually exceeds that of the electrons, or whether they equalise.

Another cause of high measured atomic temperatures could be the desorption of hydrogen from cathode surfaces. Caesium covering the cathode bonds hydrogen readily to the surface. Positive ions accelerated across the cathode sheath can gain energies of up to 100 eV, depending on the arc voltage, which is more than enough to break the caesium-hydrogen bond and release hydrogen atoms [106]. The released atoms will have a range of energies up to the cathode potential. The high energy tail of the distribution has significant influence on the average temperature measured spectroscopically. Again, a quantitative energy distribution measurement would be an excellent indicator of processes such as this.

A third, alternative explanation for high atom temperature is that strong density gradients could be causing plasma turbulence which transfers energy to the atoms. The random oscillations of optical intensity discussed in Section 5.3.1 support this idea. In an homogenously turbulent plasma with no mean flow, the energy spectrum of turbulent oscillations, $E(k)$ varies in time according to [107]

$$\frac{\partial E(k)}{\partial t} = -2\nu k^2 E(k) + T(k) \tag{5.3.1}$$

where k is the wavenumber and ν is the kinematic viscosity. $T(k)$ is the energy transport function caused by creation or destruction of wavenumber k through the

interaction between two other, dissimilar waves. In general, $E(k)$ peaks initially at low k – i.e. wavenumbers associated with large physical scales – since energy is supplied to the turbulence usually from a large-scale initial mean flow. In the case of the ion source, this would be the gas pulse from the piezoelectric valve. After the gas pulse arrives inside the plasma chamber, it takes significant time to pump away through the emission aperture. Therefore on the timescales of plasma oscillations, there is no mean flow after the initial gas pulse.

The first term on the right-hand side of Eq. 5.3.1 describes the rate of turbulent energy dissipation into heat. The factor k^2 means that energy dissipation to large-k (or small spatial scales) is high. Since total energy is conserved, this means that large-scale (small-k) oscillations decrease in time whilst ever-smaller-scale (large-k) components become more energetic. A visual example of this process is how a large whirlpool gradually breaks apart into smaller and smaller eddies as the turbulent energy is dissipated. For the case of the ion source, large-scale oscillations eventually dissipate their energy into the heating of plasma particles. The higher the arc current, the larger the initial plasma turbulence and the more energy goes into heating the atoms. This may also explain why higher current arc pulses are more quiescent in Fig. 4.9: the initial arc power spike generates high-amplitude, low-k turbulence which quickly dissipates energy into atom kinetic energy, thus rapidly diminishing the large scale plasma oscillations or *ringing* at the start of the arc pulse. This does result in higher atom temperatures, though. At lower arc currents, there is less turbulence, so the ringing takes a long time to decay and the atom temperature remains low.

5.3.3 Fulcher Spectrum

As discussed in Sections 5.1.3 and 5.1.5, analysing the molecular hydrogen spectrum can be extremely fruitful yet is rather complex; particularly for the limited optical access of the small, pulsed VESPA plasma. Therefore only the dissociation degree, R_{dis} was measured in this study, by taking the ratio $I(H_\gamma)/I(H_{Fulcher})$ and comparing with collisional-radiative models. Figure 5.19 shows the entire Q-branch of the VESPA ion source's molecular Fulcher spectrum. The Fulcher intensity was rather weak, implying that molecular emissions were low. Because of this low intensity, there were many overlapping lines from other spectra, so integrating the measured range manually gave much too high an intensity. Therefore specific individual lines were identified and used to estimate the overall intensity of the entire Fulcher spectrum as $I(H_{Fulcher}) \approx 0.8$. The integral of a Gaussian fit to the H_γ line gave $I(H_\gamma) = 1.0$. The

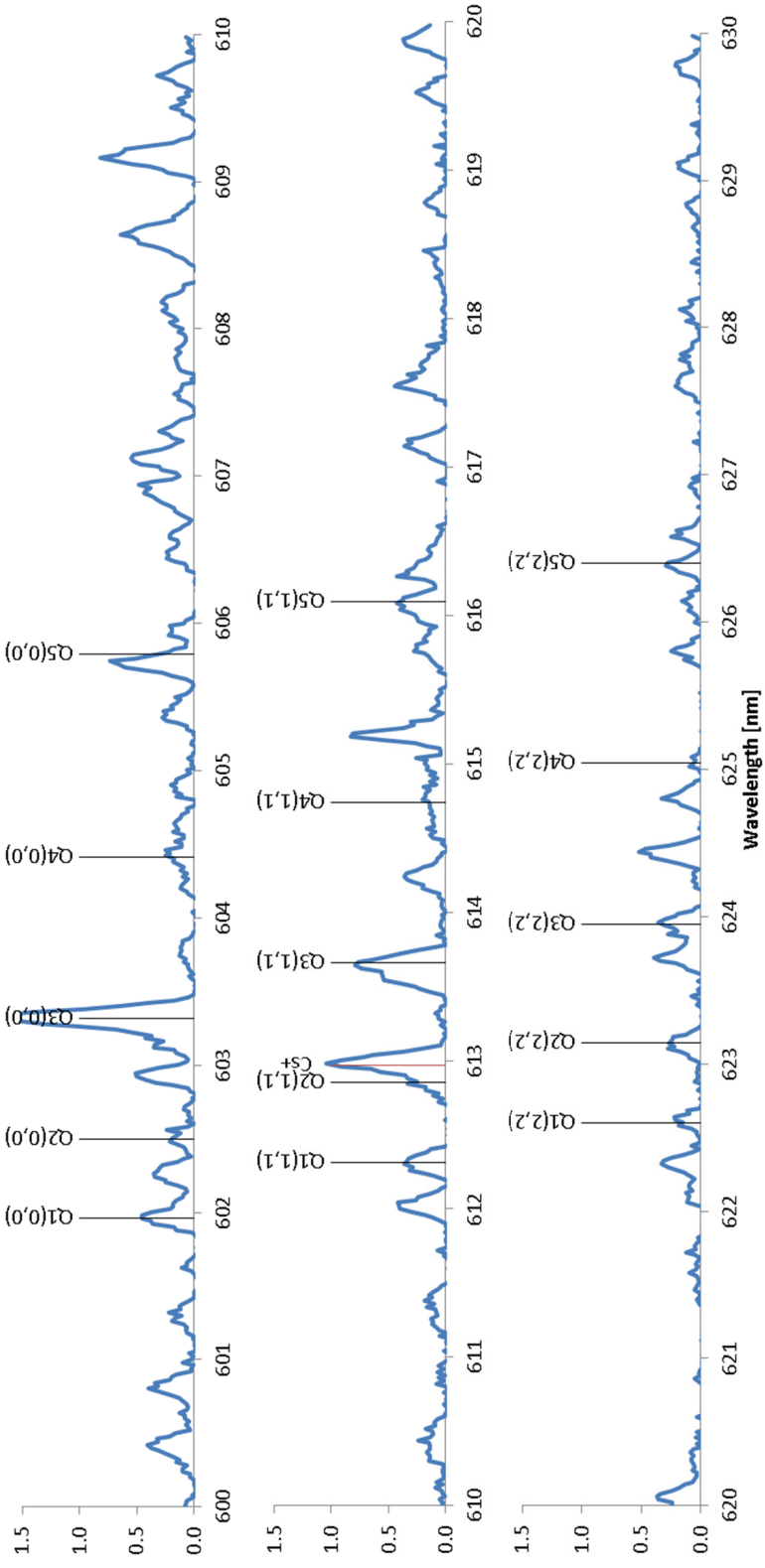

Figure 5.19: Intensity of Fulcher spectrum from 600 to 630 nm. Labelled Q-branch line wavelenth data from [88].

Yacora [108] combinative-radiative model estimated that an electron temperature of 3 eV and electron density of $1 \times 10^{19}\ m^{-3}$ yields a ratio of effective emission rate coefficients $X^{eff}_{H_\gamma}/X^{eff}_{H_{Fulcher}} \approx 1.75$. Rearranging Eq. 5.1.7 gives

$$R_{dis} = \frac{n_H}{n_{H_2}} = \frac{I(H_\gamma)}{I(H_{Fulcher})} \frac{X^{eff}_{H_{Fulcher}}}{X^{eff}_{H_\gamma}} \sim 70\%. \tag{5.3.2}$$

This is a rather high dissociation degree compared to the 10-15% measured in large volume-type plasmas [109]. The gas was much more dissociated and as a result the plasma density plotted in Fig. 5.17 was at least an order of magnitude higher than that measured in typical RF plasmas. The high dissociation degree implies that molecular emissions were low compared to RF sources, and may also explain why previous measurements of vacuum-ultraviolet (VUV) emissions [110, 111] gave unexpectedly low Lyman molecular-band intensity.

The high molecular dissociation degree could be another contributing factor to high measured atomic temperatures. If a fast particle collides with an H_2 molecule and has a kinetic energy of at least 4.51 eV, it will dissociate the H_2 [112]. Any remaining energy may be used to either excite the dissociated atoms or impart kinetic energy on them. Cathode-produced particles have kinetic energies up to the cathode potential of several tens of volts: ample energy to provide significant atomic heating. With a measured molecular dissociation fraction of 70%, there is evidently a high collision rate, and with the density increasing with arc current, this could explain the high measured atomic temperatures in Section 5.3.2.

5.4 Measurement Errors

Measuring the plasma parameters using OES methods was challenging in an ion source plasma as small as the VESPA's, so it is unlikely that cumulative errors could ever be better than 10%. Nevertheless, thorough consideration was given to all error sources to determine and reduce the dominant factors. A breakdown of the error sources is given in Table 5.2. Error propagation was used throughout and emission lines were measured several times to reduce the standard errors on curve fitting functions. Specific argon emission lines were chosen such that the quantity being measured (either electron density or temperature) was relatively independent of the other parameter, however they could not be separated entirely in the combinative-radiative models. For example, calculation of the argon-750 nm emission rate coefficient (which yielded the

Table 5.2: Measurement errors propagated through calculations of plasma parameters using optical emission spectroscopy techniques. Parameters defined in main text and in Table 5.3.

Experimental Error	**Contributing Errors**
$\sigma_{T_H} = 4\%$	$\sigma_{\Delta\lambda} = 2\%$
$\sigma_{R_{dis}} = 11.9\%$	$\sigma_{I(H_{Fulcher})} = 10\%$ $\sigma_{I(H_\gamma)} = 4\%$ $\sigma\left[\frac{X^{eff}_{H_{Fulcher}}}{X^{eff}_{H_\gamma}}\right] = 5\%$
$\sigma_{n_H} = 13.6\%$	$\sigma R_{dis} = 11.9\%$ $\sigma_{P_{pulse}} = 5\%$ $\sigma_{T_H} = 4\%$
$\sigma_{n_e} = 7 - 11\%$	(σ_{T_e}) $\sigma\left[\frac{I(Ar_{480.6})}{I(Ar_{488.0})}\right] = 7 - 11\%$ $\sigma\left[\frac{X(Ar_{480.6})}{X(Ar_{488.0})}\right] = 1\%$
$\sigma_{T_e} = 9 - 15\%$	(σ_{n_e}) $\sigma\left[I(Ar_{750})\right] = 5 - 13\%$ $\sigma_{P_{pulse}} = 5\%$ $\sigma_{T_H} = 4\%$ $\sigma\left[X(Ar_{750})\right] = 3\%$ $\sigma\left[H_2^{flow}\right] = 1\%$ $\sigma_{Ar^{flow}} = 1\%$ $\sigma_{Calib.} = 1\%$

electron temperature) required knowledge of the electron density. However accurate determination of the density required prior knowledge of the temperature. Therefore, both parameters were calculated iteratively until they converged. Because of this iterative nature, errors on n_e and T_e were correlated, making their exact value difficult to determine. Regardless, the largest errors were due to low signal-to-noise on the argon and Fulcher emission lines which is evident by the variable-sized error bars shown in Figs. 5.17 & 5.18. The absolute intensity calibration procedure discussed in Section 5.2.2 led to a conversion factor between measured photomultiplier current and photon intensity, with a total systematic calibration error $\sigma_{Calib.} = 1\%$.

Table 5.3: Measured plasma parameters at standard 50 A operational settings.

Parameter	Measured Value
Peak pulsed pressure, P_{pulse}	$(8.0 \pm 0.4) \times 10^{-1}$ mbar
Electron Density, n_e	$(1.6 \pm 0.1) \times 10^{19}$ m^{-3}
Atom Density, n_H	$(1.2 \pm 0.2) \times 10^{20}$ m^{-3}
Electron Temperature, T_e	(3.5 ± 0.3) eV
Atom Temperature, T_H	(2.8 ± 0.1) eV
Dissociation Degree, R_{dis}	$(71 \pm 8)\%$

5.5 Discussion

The major plasma parameters measured are given in Table 5.3. The steady-state plasma parameters were measured at the end of the arc pulse. An extension to the project could be to evaluate how the parameters vary in time during the arc pulse. This is complicated because the ringing at the start of the arc (and hence light) is different pulse-to-pulse, so it would be unclear whether the emission parameters varied in time, or if it were just an artifact of the random arc noise at plasma ignition.

The high dissociation degree tends to favour H^- surface-production mechanisms through the bombardment of H^0 atoms with the cathode. Conversely, at 2.8 eV, the dominant H^- ion destruction process is from mutual neutralisation with H^+ ions, with a cross section, $\sigma = 8 \times 10^{-19}$ m^2 [113]. This leads to a mean free path, $l = (\sigma n_{H^+})^{-1} \approx 8$ cm, assuming $n_{H^+} = n_e$ for plasma quasineutrality. On the other hand, although the cross section for resonant charge exchange between H^- and H^0 is similar at 1×10^{-18} m^2, the ten times higher n_{gas} leads to a mean free path ~ 1 cm. Therefore, the small mm-scale of the Penning ion source has two benefits: most H^- ions are able to be extracted without being destroyed and, moreover, a significant proportion of fast cathode-produced H^- ions are able to undergo resonant charge exchange with slow H^0 atoms, resulting in a low temperature (thus low emittance) extracted H^- beam.

The addition of argon into the plasma was necessary as a diagnostic gas with well-documented emission rate coefficients. However it was shown both experimentally and in an SRIM simulation that argon disrupted the cathode-layer of caesium severely. Therefore it may be questioned if argon also compromised the plasma itself, potentially affecting the measureable plasma parameters. Assuming the hard-sphere

collision model, with molecular hydrogen and atomic argon van der Waals radii $r_{H_2} = 120$ pm and $r_{Ar} = 188$ pm, respectively [114], the cross section $\sigma_{H_2Ar} = \pi(r_{H_2}+r_{Ar})^2 = 3\times10^{-19}$ m^2. This leads to an argon mean free path of around 3.4 cm, which is several times larger than the plasma dimensions. Therefore, there were very few argon collisions with plasma particles, implying a negligible change to the plasma temperature.

Integrating Fig. 5.16 over the entire spectrum gave a total emission power density of 6.2 W mm^{-2}. Assuming optical emissions were approximately isotropic throughout the plasma, this gave a total optically emitted power of 780 W: around 30% of the input arc power. This is a high yet reasonable value, especially when combined with evidence of low VUV emissions in previous studies: the high plasma density resulted in a shift in emission power from low to high wavelengths as the plasma became optically thick to UV emissions [115].

With the plasma parameters measured using OES techniques, beam extraction simulations could be performed with accurate starting conditions. The results of particle tracking, as well as electrostatic and thermal simulations, are discussed in Chapter 6.

Chapter 6

Simulations

Ion source research requires simulations over a wide range of physics. Unfortunately the asymmetric, high density, high temperature, time-dependent nature of the Penning ion source makes plasma simulations exceptionally difficult both conceptually and in terms of financial resources. Therefore a true plasma simulation is outside the scope of this thesis. Nevertheless an excellent start to many other simulations can be made through the use of the plasma parameters measured using optical spectroscopy techniques in Chapter 5.

The first type of simulation detailed in Section 6.1.1 concerns the extraction of a particle beam from the plasma. Accurate models of this region are critically important because the beam quality or *emittance* generated at extraction from the ion source determines the transport effectiveness throughout the entire accelerator complex. Next, Section 6.1.2 discusses the particle tracking simulations performed to design new post-extraction electrodes to ensure flexible, efficient injection into the following accelerator. Section 6.2 details the electrostatic simulations carried out to ensure that the electrode system arrived at from particle tracking simulations can actually be manufactured to achieve minimal sparking. Finally, thermal simulations discussed in Section 6.3 ensure that the electrodes do not overheat from any lost beam.

The undertaking of the various simulations also requires a deep understanding of other practical problems, which lead inevitably to an iterative design procedure. For example, consideration must be paid as to how to apply cooling to various electrodes: electrical isolation of the cooling water must exist somewhere in the system, otherwise large drain currents or even sparking may occur in the water. Providing space for cooling, for example by increasing the thickness of electrodes to allow internal cooling

channels, may then impact on the high voltage and beam transport designs.

Electrodes need electrical connections, usually in the form of cable from a vacuum feed-through. The cable layout from feed-through to electrode must be designed so that the cable doesn't spark to ground. High voltage coaxial connections are difficult or expensive to achieve in vacuum, generally, because standard coaxial insulating materials have high *out-gassing* rates. Therefore, the centre conducting wire is usually left bare, coated in a thin layer of Kapton, or covered in ceramic beads. The wire should then be of a large enough gauge to reduce electrical field enhancement, and should be kept out of the vicinity of stray particles. The wire must then be connected onto the electrodes with a screw terminal, since solder out-gasses in vacuum. The screw terminal must be secure enough to pass potentially high currents, but small enough to reduce field enhancement. Although trivial, all experimentalists working with high voltage cables in vacuum have had issues with wiring, so it is important to consider it in the design.

An ion source uses a high input gas flow, which needs to be removed as quickly as possible from the vacuum vessel to reduce ion beam stripping losses through collisions with residual gas particles. Therefore a high vacuum pumping speed in the vicinity of the source is mandatory. Equally, the vacuum pressure should be low in the region of high voltage components to reduce spark rates, which are pressure-dependent according to Paschen's Law [116]. Therefore, the electrodes should be designed such that they do not affect the vacuum pumping speed adversely. For example, pumping holes can be added and large surface areas removed which would impede the molecular flow.

A final issue which should be taken into account during the simulation process is the mechanical assembly of the electrodes. An alignment system should be included to ensure coaxiality and parallelism. Bolt heads should be rounded and recessed if they are in a region where they could contribute to field enhancement and sparking. Sufficient thickness should be allowed in the electrode material for bolt threads.

With the understanding that mechanical issues such as these are taken into account, the following sections of this chapter address the particle tracking, electrostatic and thermal simulations performed to design the VESPA post-extraction electrodes.

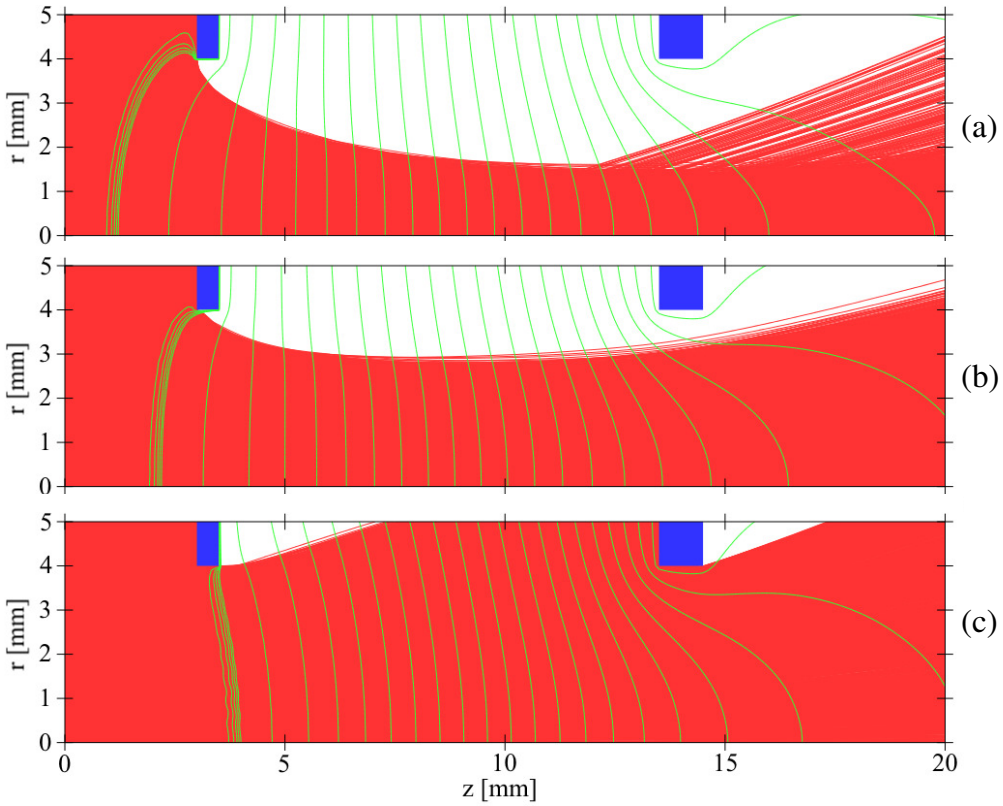

Figure 6.1: Simple cylindrically symmetric 2D model of a two-electrode or *plain diode* extraction system. Electrodes are solid blue items, H^- ion trajectories are red and equipotentials are green. Particles stream from the plasma on the left toward the outlet aperture. The electric field is shaped at the aperture by the balance between the beam space-charge and the extraction voltage. In this way, the particles appear to be emitted from a quasi-boundary called the *plasma meniscus* at the aperture. For a constant beam current density, the meniscus is varied by reducing the extraction potential from (a) to (c). Simulation performed using IBSimu software package [117].

6.1 Particle Tracking

6.1.1 Plasma Meniscus

Very low energy plasma particles follow electric field lines, which are orthogonal to equipotentials. At the outlet aperture of the plasma electrode, a quasi-boundary is formed called the *plasma meniscus*, as shown in Fig. 6.1. The meniscus is the location in the potential field where the outward-going space-charge field of the plasma balances the inward-pushing field from the extraction electrode. It is not a true boundary because the potential decays exponentially to zero, rather than having a sharp edge. However it is a helpful concept to tell qualitatively where the particle trajectories inside the plasma 'begin'. If the meniscus has an overly concave shape,

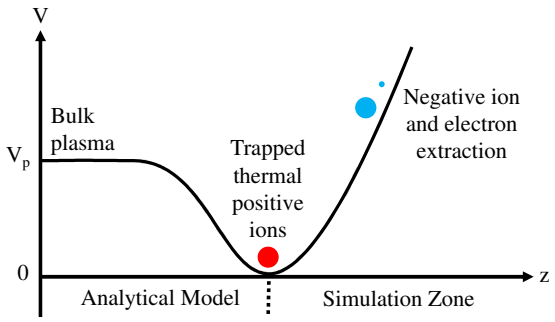

Figure 6.2: Schematic diagram of the analytical negative ion plasma model used in IBSimu. Negative ions are created close to the outlet aperture at zero potential, creating a local field minimum due to their excess negative space charge. Positive ions made at plasma potential V_p are accelerated toward the minimum. There, they are trapped and thermalised in the potential well formed by the rising positive extraction field on the other side of the aperture. The simulation domain begins at zero potential, with the analytical model controlling the flux of fast and thermal positive ions.

as in Fig. 6.1a, particles emerging from the plasma are over-focussed and a beam *halo* is formed. Halo should be avoided as it can cause losses and activation later in the accelerator. A convex meniscus bulging out of the outlet aperture will form a large divergent beam, as in Fig. 6.1c. Therefore, the meniscus should be set flat or slightly concave such that the beam is focussed smoothly with minimal divergence after extraction, for example in Fig. 6.1b. This case is called the *perveance match* and is the ideal compromise between high extracted current and transportability. The extraction voltage and plasma density should thus be tuned *together* to achieve a perveance match at the desired beam current.

The Ion Beam Simulator (IBSimu) software package [117] was used to simulate the new extraction system. The software is capable of solving fully-3D, space-charge-dominated problems with the comprehensive negative-ion plasma model demonstrated schematically in Fig. 6.2. H^- ion sources necessarily include at least one dipole magnetic field to either filter out high energy electrons inside the plasma chamber, or to mass-separate co-extracted electrons from the H^- ion beam. Therefore a full 3D simulation is mandatory, even if the ion source is in all other aspects axisymmetric. As such, IBSimu is the ideal choice for modelling H^- ion sources. IBSimu solves Poisson's equations on a regular rectangular mesh using finite-difference techniques, rather than the more common finite-element mesh. This means that the mesh cannot have regions with different densities, so the total number of mesh cells quickly becomes large if very small features must be resolved. The standard ISIS ion source

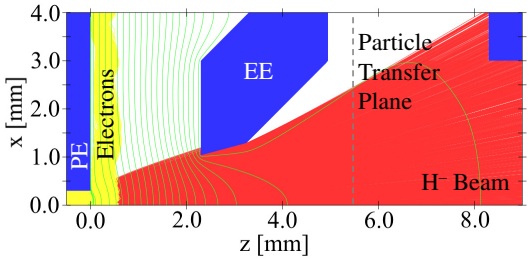

(a) 6 kV extraction voltage.

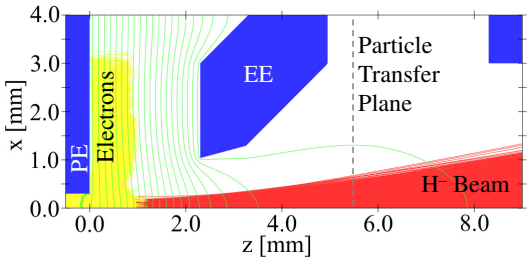

(b) 13 kV extraction voltage.

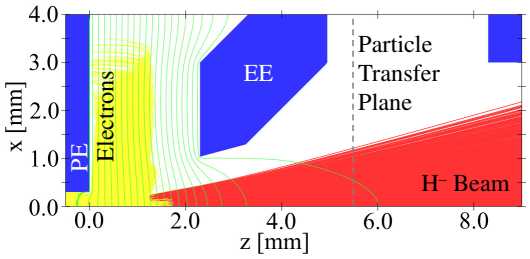

(c) 20 kV extraction voltage.

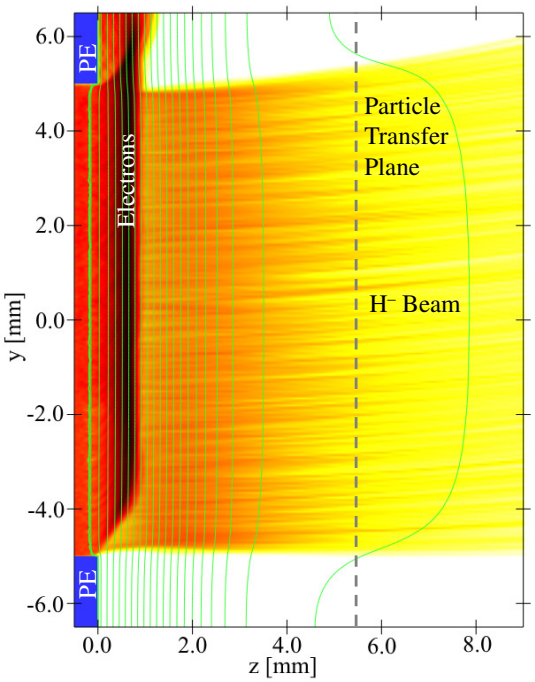

(d) Particles in the vertical plane at 13 kV extraction voltage. Particles coloured by current density on a logarithmic scale.

Figure 6.3: Particle tracking from the VESPA Penning ion source plasma. The plasma (PE) and extraction (EE) electrodes are shown as solid blue objects. Green lines show equipotentials. Figures (a), (b) & (c) show how the extraction voltage affects the plasma meniscus and initial focussing of H^- ion (red) and electron (yellow) tracks in the horizontal plane. Figure (d) shows particle current densities in the vertical plane, emphasising the mass-separation effect of the Penning magnetic field. Note also how the H^- beam centre is deflected vertically by approximately +1.0 mm. The EE cannot be seen in (d) because a feature of the EE geometry is that it is open at both ends. However the equipotential lines indicate its general shape. Figures (b) and (d) show an approximately perveance-matched beam at 13 kV extraction voltage.

plasma electrode emission aperture is a (0.6×10.0) mm^2 slit. On the VESPA, the ion source was mounted such that the long slit dimension was vertical (along the y-axis) and the short slit dimension was horizontal (along the x-axis). Beam was extracted and travelled along the z-axis. Accurate resolution of the plasma meniscus required at least 10 mesh steps across an aperture. Because of the narrow horizontal slit dimension, the entire extraction model therefore had a mesh size of 50 μm. The puller electrode, typically biased to +18 kV relative to ion source ground potential, was separated from the plasma aperture by 2.3 mm. There was significant electric field penetration through the 2 mm-wide puller aperture, and the H^- beam had enormous space charge at that location, so the simulation must solve the field a sufficient distance past the puller for accurate results. On the other hand, the small mesh size led to computational memory issues. Therefore a reasonable compromise was to track extracted particles to 9 mm from the plasma aperture. Particle positions and velocities were then transferred to a following simulation of the post-extraction optics with a larger mesh size of 250 μm. Particles were actually transferred at 5.5 mm to avoid simulation-boundary effects.

To first order, the meniscus curvature was affected by the plasma emission current density and the extraction voltage. Figure 6.3 shows 25,000 particles tracked through the ISIS extraction geometry using the analytical negative ion plasma emission model in IBSimu. The simulation was fully 3D with space charge. A magnetic field map was imported from Opera3D [118]. If the voltage was too high or the current density too low, the meniscus was very concave. On the other hand, a high plasma density and low extraction voltage lead to a convex meniscus. Assuming a balance was achieved, second order effects such as particle starting energy became important, and this is where accurate plasma parameters were crucial. Figure 6.4 shows how the output beam emittance and Twiss parameters varied with extraction voltage when the plasma particle temperatures were varied away from the real measured values in Section 5.5. It can be seen that if incorrect estimates were made of the plasma parameters, the beam emittance and focussing from the meniscus was affected. This is because the effective space-charge of positive ions changed, depending on their velocity in the vicinity of the potential minimum. As expected, lower particle temperatures led to lower emittance, but also affected at what extraction voltage the perveance match was found. This analysis demonstrates why the gas and electron temperatures given in Table 5.3 are so important as inputs to IBSimu's negative ion plasma model if successful, low emittance extraction systems are to be designed.

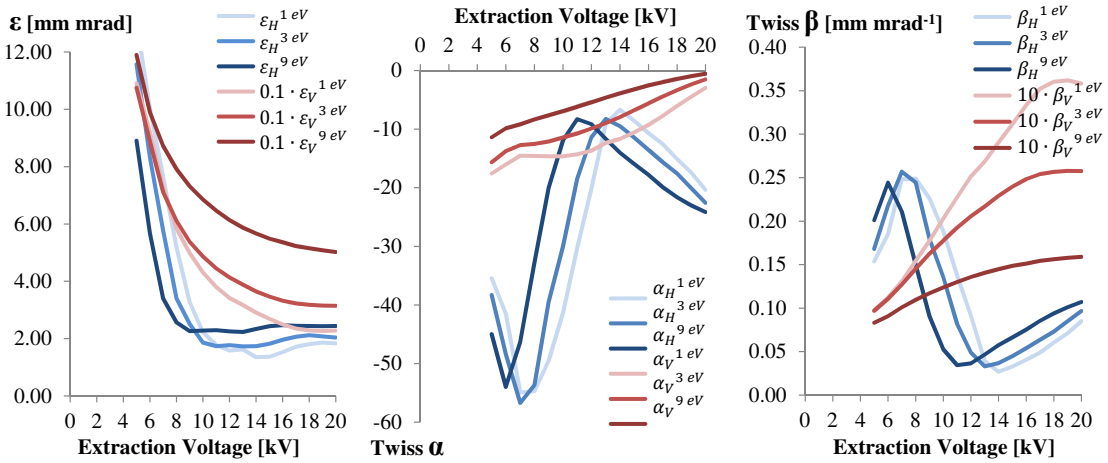

Figure 6.4: Simulation of a beam extracted from a slit-shaped plasma outlet aperture. Blue and red lines show trends in the horizontal (H) and vertical (V) planes, respectively. Darker colours indicate increasing ion temperature. Note that the vertical parameters have been scaled by a factor of ten for clarity. An ion emission current density of 1.42 A.cm^{-2} and an electron to ion ratio of 3 were assumed. The electron and ion temperatures of around 3 eV measured in Section 5.5 were used as inputs, but the effect of varying the temperatures is also shown. Note that the beam was always divergent, as indicated by negative Twiss α values. The sudden change in Twiss parameters below 8 kV extraction was due to collimation of highly divergent particles from a convex meniscus. A perveance match was achieved at around 13 kV when α and β were minimised: indicating a small, almost parallel beam.

6.1.2 Post-Extraction Optical Elements

Particles were transferred from the high-resolution plasma extraction simulation to the post-extraction region. The H$^-$ ion beam had an asymmetric profile due to the slit-shaped outlet aperture: it was larger vertically than horizontally. However due to a combination of electric field penetration through the puller electrode and large space-charge forces in the horizontal plane, the beam was approximately ten times more divergent horizontally than vertically. Therefore, strong horizontal focussing was needed immediately after extraction. There are several focussing options available to an accelerator designer, the most common examples being: 1. quadrupole magnet 2. solenoid magnet 3. dipole magnet with edge focussing 4. aperture lens 5. immersion lens 6. einzel lens 7. electrostatic quadrupole 8. plasma lens.

The Lorentz force law says that the focussing strength of magnetic elements increases with the charged particle velocity. This makes items 1-3 unsuitable for very low energy ion beams. Electric quadrupoles are commonly used in mass-spectrometers

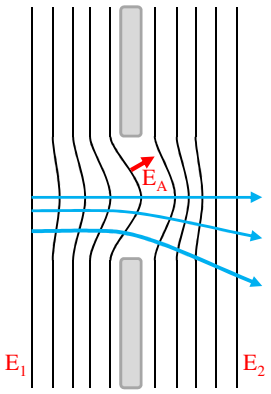

Figure 6.5: Operating principle of an aperture lens.

and in Radio-Frequency Quadrupole (RFQ) accelerators, however they likely wouldn't be able to cope with large, asymmetric beams. Plasma lenses are sometimes used in transport lines where the beam is space-charge compensated and space is not at a premium; again these requirements are not the case near extraction. Therefore only electrostatic lenses, items 4-6, were suitable for the VESPA.

A thorough mathematical description of electrostatic lenses can be found in [119]. To summarise, an aperture lens is constructed from an electrode separating electric fields of different magnitudes. A hole in the boundary allows passage of a charged particle beam, but also to some extent the electric field: whichever field is strongest will protrude through the aperture, as shown in Fig. 6.5. Depending on which side of the aperture the field protrusion is, an incoming particle beam is either focussed or defocussed, with a strength given by

$$f = \frac{4V}{E_2 - E_1} \tag{6.1.1}$$

where V is the voltage of the aperture electrode measured relative to the particle source potential and E_1 and E_2 are the electric field strengths either side of the aperture. The focussing strength is positive (i.e. focussing) if the electric field is stronger on the downstream side of the aperture. Therefore accelerated particles are focussed and decelerated particles become defocussed.

An immersion lens is an extension of the aperture lens; consisting of two apertures at different voltages V_1 and V_2, separated by a distance L. The focal strength is different for each aperture: for the first aperture it is given by

$$\frac{f_1}{L} = \frac{4\left(\sqrt{V_1/V_2} + 1\right)}{V_2/V_1 + V_1/V_2 - 2} \tag{6.1.2}$$

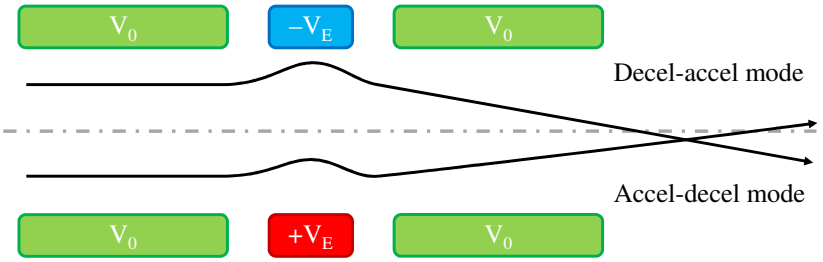

Figure 6.6: Operating principle of a cylindrically symmetric einzel lens in decel-accel mode (top) and accel-decel mode (bottom), for a negative ion beam. The outer electrodes are grounded and the centre electrode is powered. A decel-accel einzel has stronger focussing power than an accel-decel, for a given voltage.

and for the second aperture, the focal strength is given by inverting the voltages $V_1 \leftrightarrow V_2$ in Eq. 6.1.2. The overall focal strength of an immersion lens is always positive no matter which electrode is at a higher voltage. The final beam energy is equal to the voltage on the second aperture.

An einzel lens is the next extension of electrostatic aperture lenses, consisting of three electrode apertures, where the final beam energy doesn't change. The first and third electrodes are at the same potential, whereas the centre electrode may either accelerate or decelerate the ion beam, depending on its set voltage. Typically an einzel lens is located such that the outer electrodes form part of the (grounded) beamline, then only one power supply is needed for the centre electrode. This is where the name 'einzel' ('single' in German) originates: only one electrode is powered. An einzel lens where the beam is decelerated in the centre before returning to its starting energy ('decel-accel') has a stronger focussing for a given voltage. The drawback is that the expanded beam traverses non-linear edge fields near the electrode and suffers emittance growth from spherical aberrations. An accel-decel lens requires an opposite-polarity power supply with a higher output voltage and does not provide as strong focussing. It is nevertheless the preferred option as beam aberrations are reduced since the beam is squeezed closer to the axis, rather than blown up. The two modes of einzel lens operation are shown in Fig. 6.6.

6.1.3 Einzel Lens Tracking

The VESPA post-extraction system required strong focussing in the horizontal (x) plane in addition to acceleration to the 35 keV RFQ input energy. Therefore a system was designed which combined the acceleration properties of an immersion lens with

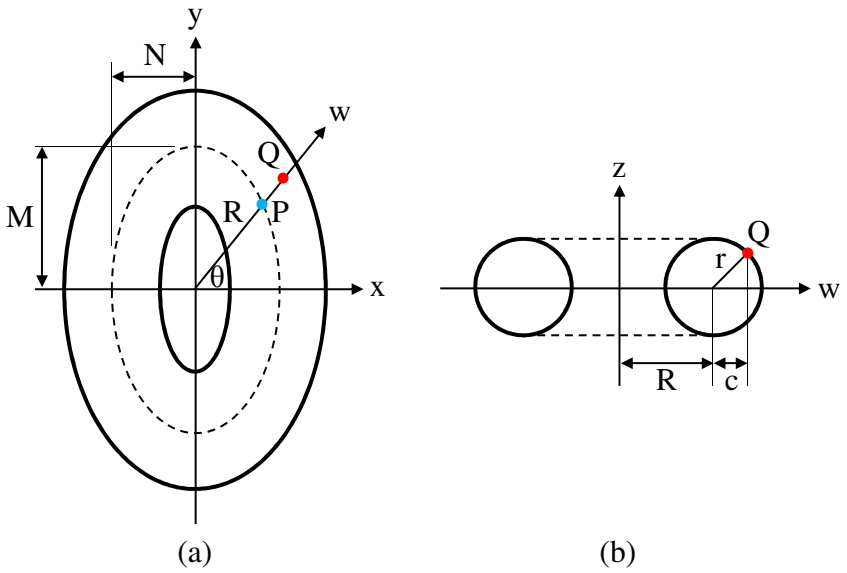

Figure 6.7: Geometry of an elliptical torus. Parameters defined in main text.

the strong focussing properties of a decel-accel einzel lens. This kind of focussing scheme is technically known as a three-aperture immersion lens (TAIL). However for simplicity, it will still be referred to as an einzel lens throughout this thesis. A novel adaptation was devised by the author whereby the einzel lens aperture had an elliptical profile to provide a different focussing strength in both planes. Since the extracted H^- beam was very divergent horizontally, the elliptical einzel's minor axis was in the x-direction to provide stronger focussing than in the y-direction.

The TAIL-einzel is an already complicated system which does not readily lend itself to simple transport matrix solutions, particularly in a region of strong space-charge with a highly divergent input beam. Adding an elliptical aperture to the einzel lens further scaled up the problem (as did adding a tilt, discussed below), so an iterative fully-3D particle tracking simulation was required. To arrive at the optimum solution, the geometry was parametrised so several simulations with different ellipse major and minor axes could be run in parallel. This being the case, parametrised 3D geometry could not efficiently be imported into IBSimu: it needed to be generated procedurally. IBSimu has a method called 'FuncSolid' which allows the programmer to write a boolean function which returns *true* if a point in 3D space lies inside the required geometry, or *false* otherwise. As long as a shape can be described analytically in cartesian coordinates – or can be built up of several smaller analytically-definable shapes – then it can be defined in this manner. The three-dimensional shape needed to describe the einzel lens was an elliptical torus, shown in Fig. 6.7.

An ellipse may be defined as a scaled circle in the (x, y) plane by

$$\frac{x^2}{N^2} + \frac{y^2}{M^2} = 1 \tag{6.1.3}$$

where M and N are the major and minor axes, respectively, of an ellipse with the longer scaling in the y-direction. Multiplying through by M^2N^2 gives

$$M^2x^2 + N^2y^2 = M^2N^2. \tag{6.1.4}$$

Factoring out some parameter R^2 on the left hand side leaves

$$R^2\left[\frac{M^2x^2}{R^2} + \frac{N^2y^2}{R^2}\right] = M^2N^2. \tag{6.1.5}$$

Finally, dividing through and taking the square root results in

$$R = \frac{MN}{\sqrt{\left(\frac{Mx}{R}\right)^2 + \left(\frac{Ny}{R}\right)^2}}. \tag{6.1.6}$$

The parameter R in equations 6.1.5 and 6.1.6 may be thought of as the 'radius' of the ellipse at some angle θ from the x-axis. Point P at coordinates (x, y) on the dashed ellipse in Fig. 6.7a satisfies $x/R = \cos\theta$ and $y/R = \sin\theta$, hence

$$R = \frac{MN}{\sqrt{(M\cos\theta)^2 + (N\cos\theta)^2}} \tag{6.1.7}$$

which is simply the equation of an ellipse in 2D polar coordinates. If a circle of radius r is centred on the dashed ellipse and revolved around the z-axis (normal to the x- and y-axes), an elliptical torus is formed. Figure 6.7b shows a cross section through said torus on the wz plane which is rotated by the angle θ from the xz plane. Point Q lies on the surface of the torus at coordinates $(x, y, z, w = c + R)$. Considering the geometry of the circular cross-section,

$$\begin{aligned} & c = \sqrt{x^2 + y^2} - R \\ \text{but:} \quad & r^2 = c^2 + z^2 \\ \text{hence:} \quad & r^2 = z^2 + \left(\sqrt{x^2 + y^2} - R\right)^2 \end{aligned} \tag{6.1.8}$$

which is the cartesian equation of a circular torus of major radius R and minor radius r. Therefore, to describe the surface of an elliptical torus, one must simply combine Eq. 6.1.8 with the polar radius R of an ellipse (Eq. 6.1.7) to give:

$$r^2 = z^2 + \left(\sqrt{x^2 + y^2} - \frac{MN}{\sqrt{(M\cos\theta)^2 + (N\cos\theta)^2}}\right)^2 \quad , \tag{6.1.9}$$

where

$$\theta = \arctan\left(\frac{y}{x}\right) \tag{6.1.10}$$

satisfies any ellipse, not just the dashed ellipse at the centre. To determine whether a point in cartesian space is inside or outside the torus geometry, an inequality may be used instead after the r^2 term. Equations 6.1.9 and 6.1.10 allowed a parametrised elliptical torus to be studied in IBSimu.

A further complication of the post-extraction system implemented on the VESPA was that the stray magnetic (B-)field from the Penning ion source deflected the H^- beam vertically, as seen in Fig. 6.3d. Volume-type H^- ion sources also suffer from this effect due to magnetic filter and/or dumping fields. However stray fields are only a few tens of mT, so are relatively simple to counteract by adding magnets downstream to bring the beam back on axis [120, 121, 122]. The VESPA's 0.2 T Penning field is much more difficult to counteract. Therefore, the ion source was instead tilted mechanically around the x-axis by a few degrees.

Three effects made determining the tilt-angle non-trivial: a) the stray B-field extended some distance past extraction, b) the einzel decelerated the H^- beam enough that it was further deflected by the B-field, even some tens of mm past extraction and c) the accelerating electric (E-)field after the einzel added further steering effects. Therefore an iterative procedure was implemented to optimise the focussing forces from the elliptical einzel geometry; the inter-electrode gap lengths to minimise sparking, and the tilt angle. The optimum, shown in Fig. 6.8, was defined as an on-axis, zero centroid-angle beam with approximately equal, small-valued α and β Twiss parameters in both x and y planes at 18 kV extraction voltage. This voltage was chosen because, although not ideal in terms of perveance or emittance, it was where the ion source operators had the most experience working. Since the einzel lens system presented a completely new operational regime, it was felt that keeping some parameters unchanged would enhance confidence in the einzel before it is further perveance-optimised at a lower extraction voltage. Equally, designing a system at the highest extraction voltage guaranteed good high voltage standoff at lower voltages.

The variation of emittance and Twiss parameters with extraction and einzel voltage is shown in Fig. 6.9. This demonstrates the flexibility of the new einzel lens system: a wide parameter space of Twiss parameters was available, depending on the voltages applied to the puller and einzel electrodes. A small, slightly divergent

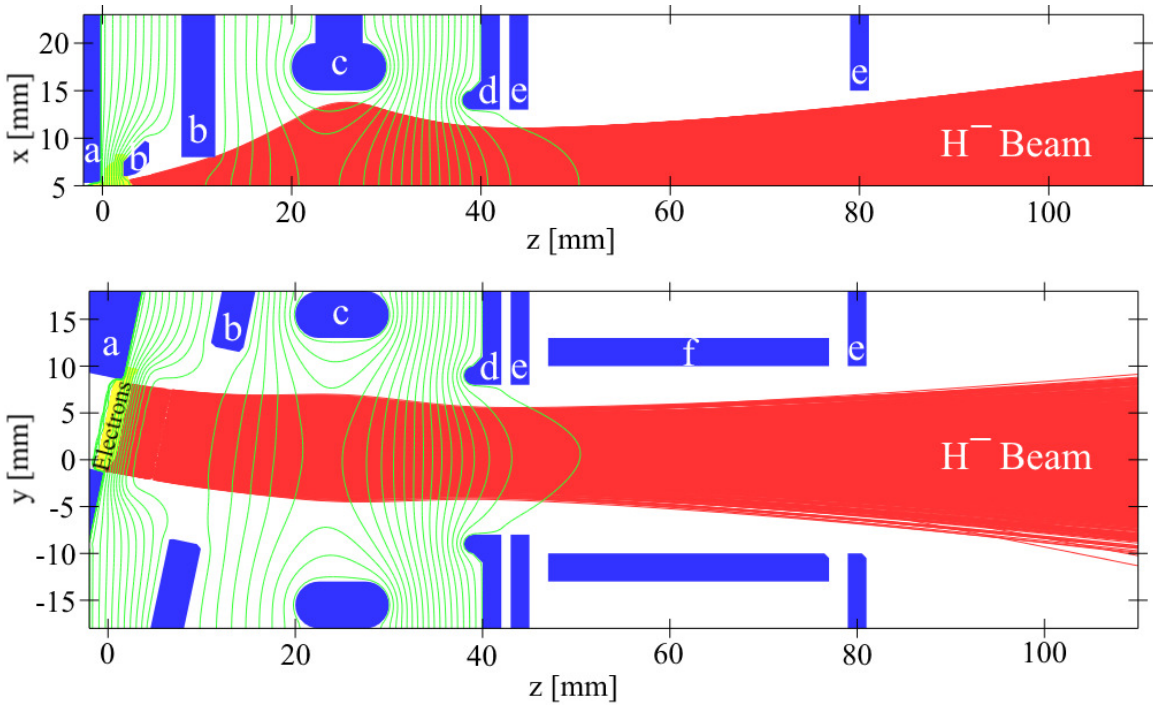

Figure 6.8: Horizontal (top) and vertical (bottom) particle tracks through the einzel lens system at 18 kV extraction voltage. The plasma (a) and puller (b) electrodes were tilted vertically by 12° with respect to the rest of the beamline. The einzel lens (c) was biased at 4 kV relative to the ion source. The beam was accelerated to 35 keV through the protection (d) and ground (e) electrodes and brought to a round profile. A pair of electrostatic chopper plates (f) were housed between the ground electrodes.

beam was produced successfully at the standard 18 kV extraction voltage, albeit with sub-optimal emittance. As discussed in Section 6.1.2, decel-accel einzel lenses are well known to cause emittance growth. Nevertheless, the solution displayed in Fig. 6.8 had significantly better performance than the output from the existing dipole magnet.

Figure 6.9 shows that the perveance-matched 13 kV beam demonstrated in figures 6.3 & 6.4 retained its low emittance through the einzel lens biased at 4 kV, but was somewhat large and divergent. This was not necessarily detrimental: for example, the ISIS solenoid LEBT was designed to accept the large, divergent beam from the existing ion source, with an RMS normalised emittance greater than 1.0 π mm mrad [123]. It is clear that the einzel lens offered many advantages to the beam transport, however other simulations were required to make it physically viable. The first of these was an electrostatic model to reduce the risk of sparking.

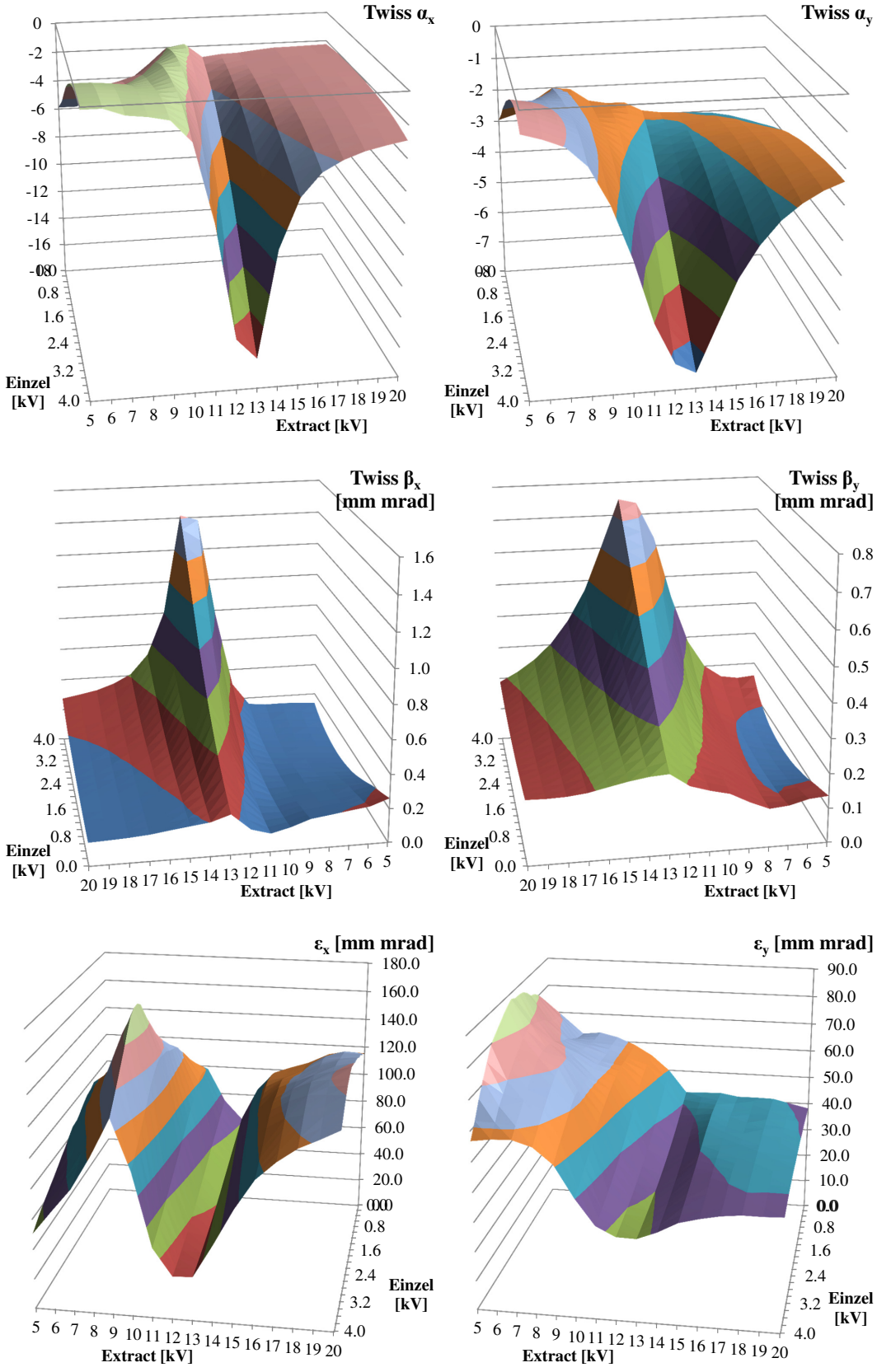

Figure 6.9: Simulated output beam Twiss parameters of the einzel lens system, as a function of extraction and einzel voltages.

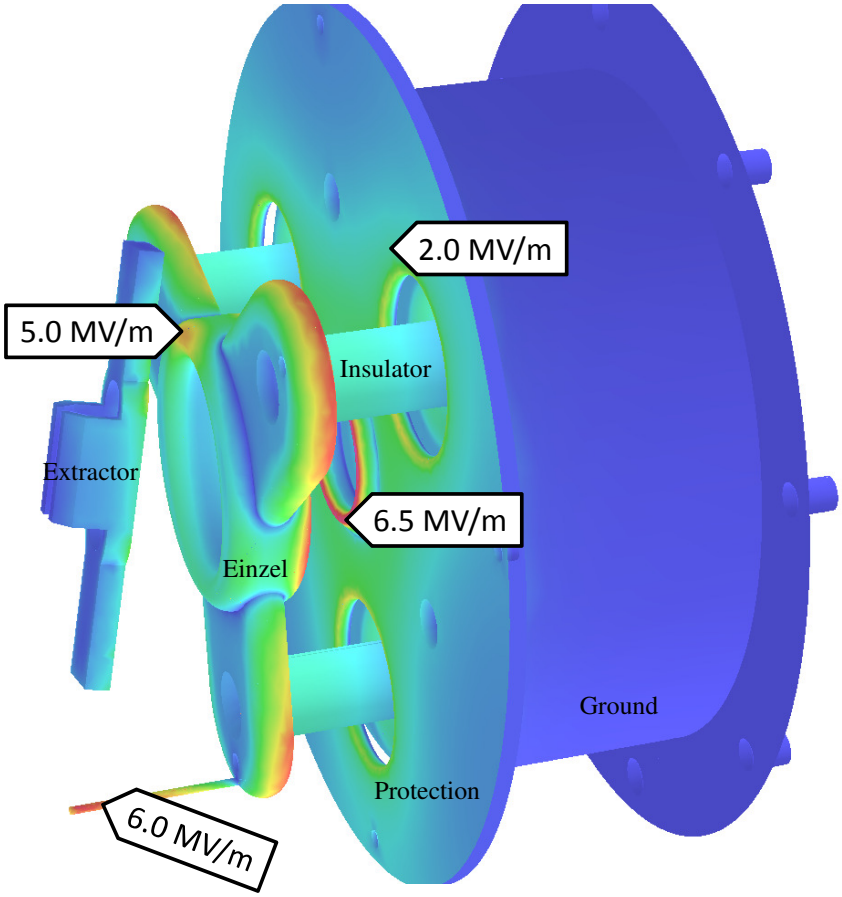

Figure 6.10: Electrostatic model of the einzel lens and other post-extraction electrodes. Coloured contours show the electric field magnitude.

6.2 High Voltage

With multiple high voltage electrodes in close proximity, it was prudent to check the high voltage performance of the geometry. The voltage at which electrodes break down in vacuum depends on a number of factors; such as the electrode material, supporting insulation, temperature, nearby magnetic fields, residual gas pressure, stray impacting particles and surface roughness. Clean, well-conditioned stainless steel in ultra-high vacuum can reach a DC electric field strength of 800 MV/m [124]. A rule-of-thumb for achievable voltage-holding in a particle accelerator RF cavity is 20 MV/m. In the high gas pressure environment surrounding an ion source, however, it pays to be even more conservative by maintaining fields below 10 MV/m. Although IBSimu calculated the electric field whilst performing particle tracking, a dedicated software package with a proven track record was deemed more suitable for accurate, large-scale electric field simulations. As such, Opera3D was used to model the einzel lens and post-extraction electrodes, and to optimise the mechanical design.

A Standard ACIS Text (SAT) geometry file was imported and a symmetry plane imposed. The finite-element mesh density was concentrated around small features which contributed to electric field enhancement. Correct permitivity values for Shapal and Macor ceramic insulators were used. As shown in Fig. 6.10, the nose on the ground electrode ensured that the electric field was concentrated in the proximity of the H^- beam, with a magnitude of 6.5 MV/m: below the prescribed limit. Note the significant field enhancement around the einzel lens connection cable, implying it was beneficial to use large-gauge wire to reduce the surface field.

The elliptical einzel lens was mounted on a tripod of insulating legs, themselves attached to the ground plane through holes in the protection electrode. As the einzel lens was biased a few kV relative to the ion source, the insulator legs needed to stand off the full 35 kV to ground. Therefore the ground electrode was designed with re-entrant holes to allow for longer legs to hold off the voltage. The protection electrode was designed as a simple disk to reduce machining costs; it was also mounted on a tripod of legs on the ground electrode. The assembly described and shown in Fig. 6.10 allowed for the use of a setting piece to ensure coaxiality of the apertures. The einzel and ground assembly was not designed to allow for cooling because the simulations showed very little beam-loss anywhere other than the puller electrode.

6.3 Thermal

A high proportion of electrons and H^- ions extracted from the plasma impacted on the puller electrode. Assuming the extraction voltage was set high enough, there was little H^- beam-loss, as previously demonstrated in Fig. 6.3. However whilst the pulsed extraction voltage was ramping up to the set-point, the H^- and electron beams were unfocussed and collimated on the puller. Therefore there was a large spike of current – and thus power – impacting the puller at the start of the extraction pulse. Electrons continued to impact and heat the puller even when the set voltage was achieved. This was because the low-mass electrons were highly magnetised by the Penning magnetic field and spiralled around the extraction gap, having multiple opportunities to hit the puller.

High voltage electrode *conditioning* due to the electron current load is of critical importance for all H^- ion sources. The electron current density, ρ_e is usually significantly higher than the negative ion current density, ρ_{H^-} and the ratio $R = {}^{\rho_e}/_{\rho_{H^-}}$

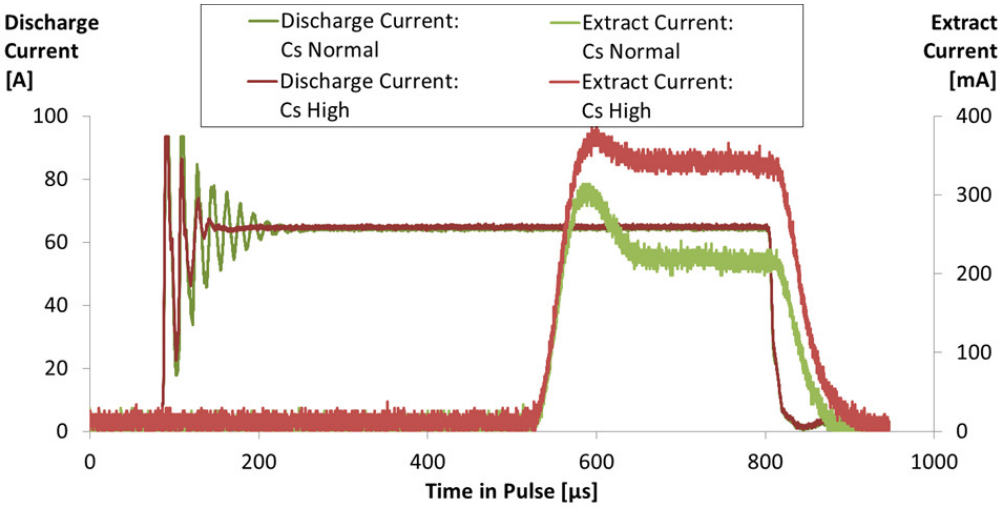

Figure 6.11: Increase in the steady-state extraction current when too much caesium is injected. The spike at the start of the extraction pulse is due to electrons impacting the puller at low extraction voltage whilst the volts are ramping up. Note also how the duration of noise at the start of the discharge pulse can be controlled with the caesium flux, as discussed in Section 4.3.1.

is very regularly discussed in the literature, precisely because of the impact on the extraction system. A higher R requires a larger extraction power supply to be able to cope with the electron current, and also significant cooling on the puller electrode due to the increased electron heat load. As discussed in Chapter 3, the addition of caesium reduces R as well as increasing the H^- production rate. As such, caesium-free volume-production H^- ion sources typically [125] have electron-to-H^- ratios $R > 10$, whereas caesiated surface-production H^- ion sources typically [126] have $R < 5$. The very large negative ion sources for the International Thermonuclear Experimental Reactor (ITER) have recently demonstrated $R < 1$ from both hydrogen and deuterium plasmas: required because of the already enormous power load of a 66 A H^- or D^- beam [104].

The Penning H^- ion source provides ample beam current for ISIS operations, so is generally optimised to reduce the extraction current load. Low extraction current is beneficial as it reduces the rate of HV breakdowns, reduces the heat load on the puller and increases the voltage achieved for a given demand voltage. In practice, to achieve a low extraction current, the hydrogen and caesium flow rates are reduced as much as possible until any further reduction would adversely affect beam output or arc noise. Example extraction current pulses are shown in Fig. 6.11.

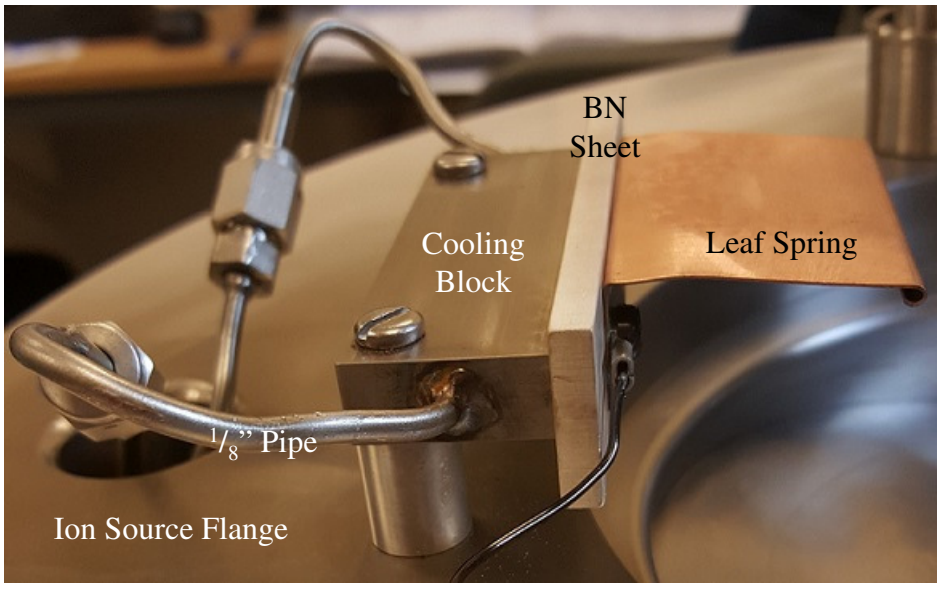

Figure 6.12: Extraction cooling block installed on the VESPA ion source flange.

The temperature of the puller electrode itself also has a strong influence on the extraction current. Caesium escaping the ion source will condense on any surface it contacts. A thin surface layer of caesium reduces the work function of the metal. A reduced work function increases the rate of electron emission from the surface. Caesium deposition is highly undesirable on electrodes as the strong electric field and enhanced emission coefficient increases the likelihood of corona discharge and eventual breakdown. Nevertheless, caesium is mandatory for efficient H^- production, so to limit its effect on HV breakdowns, electrodes should be kept hot such that the caesium is less likely to condense [127]. On the other hand, if the electrodes are *too* hot, electrons will be spontaneously emitted regardless of the presence of caesium. In addition, materials may warp or become fatigued, possibly leading to poor electrical contact or misalignment. In vacuum, the only methods of heat loss are radiative cooling, which only becomes effective at high temperatures; or conduction, which is generally poor through ceramic insulating materials. Therefore, with a high heat load and no dedicated cooling, the ion source puller electrode could become extremely hot. The puller is cooled on the ISIS source via a leaf spring making electrical contact between the puller and cold box. The cold box is held at around +5 °C, but the narrow geometry of the leaf spring gives it poor thermal conduction. Therefore the puller actually runs rather hot – desirable to prevent caesium contamination – but is nevertheless prevented from thermal runaway by the limited amount of vicarious cooling through the leaf spring.

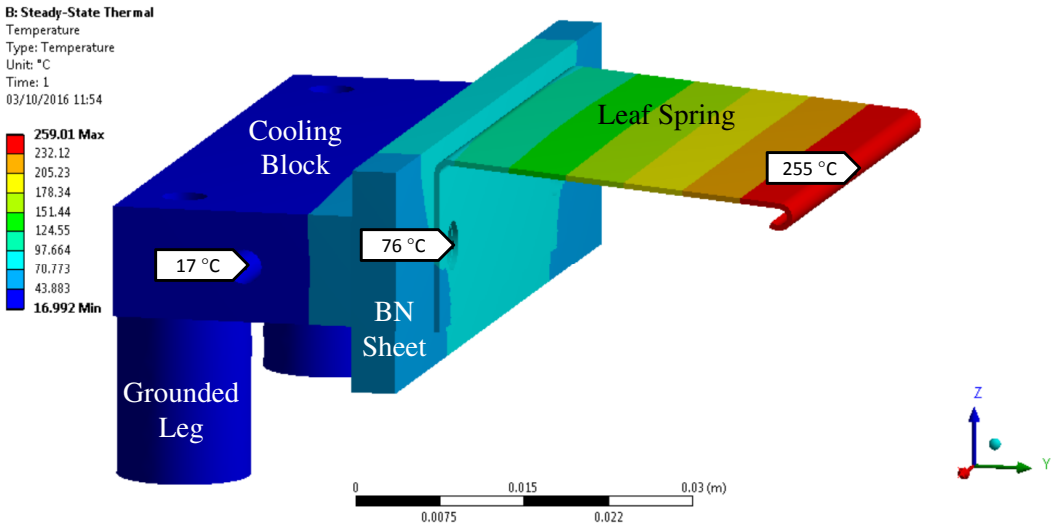

Figure 6.13: Steady state thermal model of the extraction cooling block.

During VESPA commissioning, the un-cooled puller electrode started sparking after a few hours of operation. The dissimilar metals of the puller and leaf spring have different coefficients of thermal expansion and the leaf spring was naturally under tension. The leaf spring warped and moved away from the puller over time, sparking as a small gap opened between them. This proved extraction cooling was needed.

A dedicated cooling solution was manufactured by the author. Shown in Fig. 6.12, the extraction cooling system consisted of a stainless steel block with 1/8" stainless tubes welded into a straight through-hole. Swagelok ferrules on the tubing allowed the cooling block to be detached from the ion source mounting flange. The block was bolted via aluminium legs onto the mounting flange. Therefore there was no need for an insulating break in the cooling line or de-ionised water, as the coolant was entirely at source potential. Heat from the leaf spring held at extraction potential was conducted to the cooling block via a 5 mm thick sheet of boron nitride (BN) ceramic. BN has relatively high thermal conductivity of 30 W m^{-1} K^{-1} whilst being inexpensive and easy to machine. Polyether ether ketone (PEEK) plastic screws secured the leaf spring to the cooling block, with the BN sheet sandwiched in between. The PEEK screws and BN sheet ensured the leaf spring and cooling block were isolated electrically, whereas the BN sheet connected the two thermally. The BN sheet protruded from the leaf spring and cooling block by 10 mm on all sides to increase the tracking length, preventing high voltage breakdowns in the event of the BN becoming partially conductive due to a coating of caesium.

Figure 6.13 shows that the geometry of the system was optimised in ANSYS to ensure the PEEK screws remained below 80 °C. This gave a good margin of error on avoiding the 150 °C glass transition temperature of PEEK, where mechanical failure of the screws could occur. The cooling water was safely below its boiling point. The puller electrode pressed onto the leaf spring was held at approximately 250 °C, which is very reasonable to prevent caesium accumulation. The extraction cooling block operated very well and had no failures of the Swagelok ferrules, the PEEK screws or the boron nitride sheet. The leaf spring and puller electrode were held at a safe operating temperature and the extraction current was maintained at reasonable levels to limit the rate of extraction HV breakdowns.

With a new extraction system designed through particle tracking, and the high voltage and thermal designs validated, Chapter 7 details the measured beam performance.

Chapter 7

Beam Extraction

With the sector dipole magnet removed in the VESPA set-up, a new set of focussing electrodes was designed to transport the total beam current extracted from the ion source. In order to do this, the plasma parameters measured using optical spectroscopy methods, described in Chapter 5, were used as starting conditions in a detailed particle tracking simulation in Section 6.1.1. This simulation is compared with measurements of the baseline extraction system in Section 7.1. Section 7.2 then compares the measured performance of the new einzel lens with the simulations performed in Section 6.1.3. Finally, with the beam well focussed and transportable, a novel steering and chopping scheme is demonstrated in Section 7.3.

7.1 Baseline Extraction Measurements

To measure the raw beam emerging from the puller electrode, a temporary ground electrode with a very large 80 mm aperture was installed in the gap between the puller and grounded 'spider' mounting frame. This set-up ensured no particles were lost between extraction and measurement but also did not provide any significant focussing which would affect the phase space distribution of the extracted beam. Fig. 7.1 shows the set-up and dimensions to the diagnostic devices.

7.1.1 Protection vs. Ground Electrode

Strictly, the first electrode the beam passed through was not true ground but was a few hundred volts negative. This is called the *protection electrode* and was designed to protect the extraction and einzel power supplies in the event of a high voltage breakdown. Figure 7.2 shows the principle of the protection electrode.

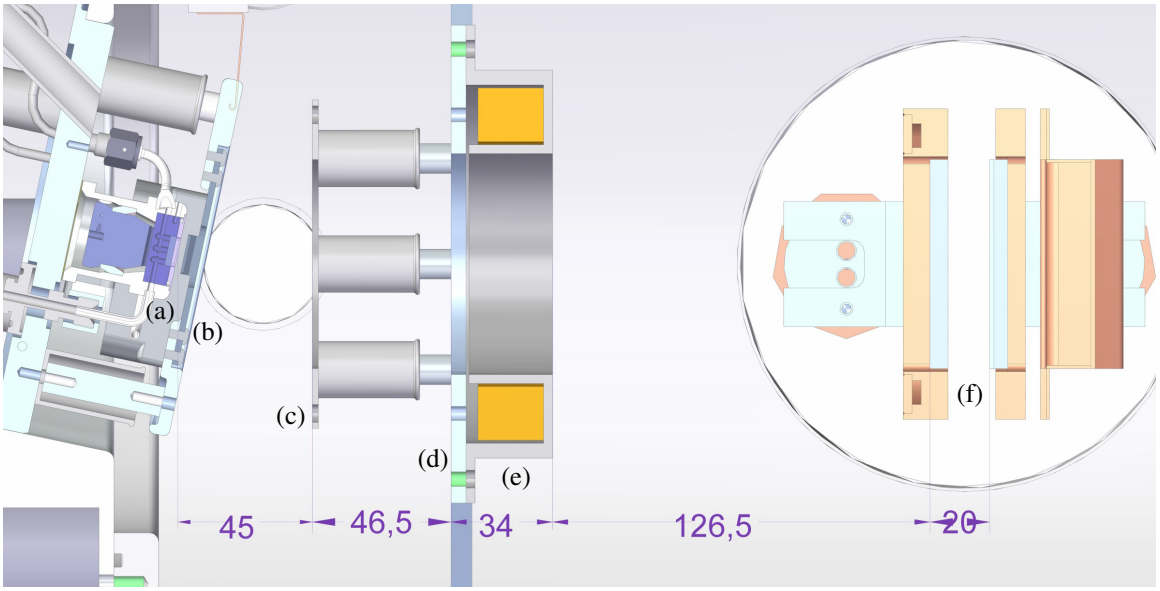

Figure 7.1: Experimental set-up of the baseline extraction measurements. The ion source (a) and puller electrode (b) were mounted at the 12° tilt determined in Section 6.1.3. A temporary ground electrode (c) was inserted between the puller and the grounded spider (d). After the spider were the toroid (e) and emittance scanners (f) to measure the extracted beam.

If no protection were installed, as in the case of Fig. 7.2a, then the extraction (puller) electrode (EE) directly faces the ground electrode (GE); the pair acting like a capacitor. In the event of a high voltage breakdown across the capacitive gap, the 1 μF reservoir capacitor inside the 35 kV power supply is momentarily shorted directly across the extraction power supply; potentially causing significant damage due to the high instantaneous current. In Fig. 7.2b, a protection electrode (PE) is inserted between the EE and GE and held at a slight negative voltage relative to the GE. Therefore the majority of the 35 kV potential difference is still between the EE and PE. In this case, though, a high voltage breakdown from the EE to the PE has the instantaneous current mitigated by a moderate series resistance. A series resistor would not help in Fig. 7.2a as stray beam current colliding with the GE would float the GE to an undefined potential, whereas it should be at true ground. The PE in Fig. 7.2b is set at a well defined voltage (and the GE held at true ground) regardless of stray beam current by adding another, higher resistance, thus creating a voltage divider. The voltage divider ratio is chosen such that the PE is only a few hundred volts away from true ground. This potential difference has negligible effect on the beam, so to all intents and purposes it can be referred to as 'ground' in subsequent beam optics discussions.

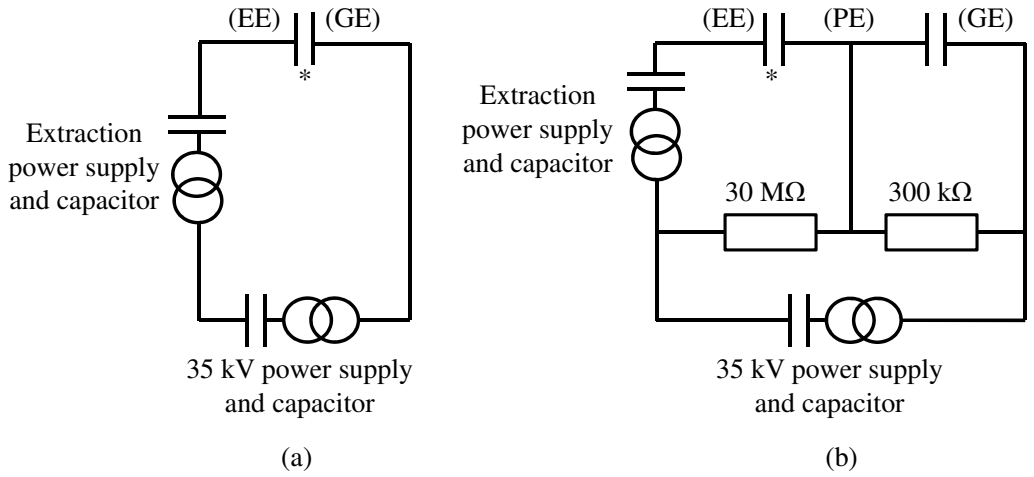

Figure 7.2: Circuit diagram of the extraction (EE) and ground (GE) electrodes directly facing each other (a) and with a protection electrode (PE) inserted in between (b). The PE is held at a defined voltage by a resistive voltage divider. The region of high voltage breakdown is indicated by *.

To characterise the ion source output, the protection and true ground electrodes had very large apertures to ensure all the beam was collected by the toroid. A simple IBSimu simulation showed that no matter how large and divergent the beam after the puller electrode, no collimation occured with the 80 mm aperture electrodes installed. Therefore, for the first time the whole H^- ion beam extracted from the ion source was measured without collimation.

7.1.2 Perveance Scans

The measured beam current is plotted in Fig. 7.3 for a range of arc plasma currents. The beam perveance $P_B = 1.7$ mA kV$^{-3/2}$ compares favourably with the theoretical perveance $P = 1.96$ mA kV$^{-3/2}$ of Eq. 3.1.16. It can be seen that, for a given arc current, the ion source perfectly followed the Child-Langmuir law – i.e. beam extraction was *space-charge limited* – up to a certain extraction voltage. Above this voltage, the ion source was *production limited* and increasing the extraction voltage was no longer an efficient method of extracting more beam: the plasma was physically not creating enough H^- ions to deliver to the puller. To achieve more beam current for a certain extraction voltage, the discharge current had to be increased so the plasma was no longer production limited. In this way, the ion source could climb higher up the perveance curve before saturating.

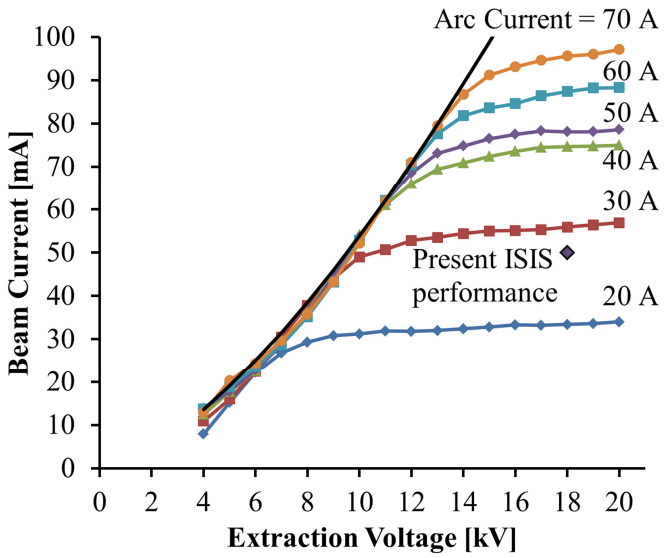

Figure 7.3: Perveance scan of the VESPA Penning H^- ion source at a range of arc currents and with no post-extraction focussing electrodes. The black curve shows the Child-Langmuir curve for a perveance of 1.7 mA $kV^{-3/2}$.

The standard ISIS set-point is marked on Fig. 7.3 to demonstrate how inefficiently it is operated: far from the ideal perveance. At 50 A arc current, approximately the same beam current could be extracted with 6 kV less on the puller electrode. The reason ISIS runs like this is because of the sector dipole magnet. The 0.2 T Penning magnetic field which sustains the plasma is generated parasitically from the sector magnet. The sector magnet is thus set to generate a field sufficient to sustain the source plasma. This results in a 0.235 T magnetic field in the main dipole gap which the beam must follow. The magnetic *rigidity* of a charged particle beam is given by

$$B\rho = 3.3356 \times 10^{-6} \frac{\beta^* \gamma^*}{\gamma^* - 1} E_K \tag{7.1.1}$$

where B is the magnetic field in T, ρ is the radius of curvature in m, β^* and γ^* are the relativistic factors and E_K is the kinetic energy in keV. It can be deduced that for an H^- beam to follow the central path of radius 80 mm inside the magnet, it must have an energy of approximately 17 keV. This explains why the source is operated in an inefficient part of the perveance curve. As an aside, because the magnitude of the Penning field is so critical for plasma stability, the beam alignment into the RFQ is not optimised by varying the sector dipole strength. Instead, the extraction voltage is varied to change the beam path round the magnet and hence its vertical position thereafter. These considerations explain why the existing ISIS ion source is operated in a peculiar manner, but which is perfectly valid from a historical perspective.

Table 7.1: Beam current at the entrance of each component in the ISIS injector

Accelerator Component	**Beam Current**
Ion source sector dipole magnet	80 mA
Low energy beam transport (LEBT)	50 mA
Radio-frequency quadrupole (RFQ)	35 mA
Linac Tank 1	34 mA
Remainder of linac	25 mA

It can be seen in Fig. 7.3 that the ion source could produce around 100 mA of beam with only a moderate increase in arc current to 70 A from the standard 55 A. This huge beam current may be useful for future accelerators such as the Front End Test Stand or an ISIS upgrade, but is far beyond what is needed presently on ISIS. The beam current delivered to the ISIS synchrotron by the linac is approximately 25 mA. Since the ion source is operated to deliver 75-80 mA, this is a terribly inefficient injector. Table 7.1 shows that the major losses come from the ion source sector magnet, the LEBT and Tank 1 of the linac.

A Medium Energy Beam Transport (MEBT) project is under-way [128] to address the loss in Tank 1, whilst the new VESPA einzel electrode can address the ion source and LEBT losses. Therefore, assuming all of these upgrades are in place and the beam-loss between the ion source and the synchrotron is reduced to a maximum of 10%, the ion source only needs to deliver around 27 mA of beam current. According to Fig. 7.3, this places the ion source comfortably on the perveance curve in the region of 7 kV puller voltage and 30 A arc current: around half the current that is used presently in operation.

7.1.3 Beam Current Stability

The extracted currents measured in Fig. 7.3 are on the face of it rather impressive, however care must be taken when discussing results measured in a laboratory setting. Ion sources have parameters which are arrived at, especially when caesium is involved. They are not like electron sources which turn on instantly, produce a constant current and do not deteriorate over time. The long-term stability of an ion source is even more important than the immediate lab result. Figure 7.4 shows how for a constant 50 A set arc current, the beam current changed over time. High beam currents were produced soon after startup, but after a 24 hour settling-in period the beam current decreased. The source parameters (primarily temperature and caesium flow rate) were adjusted

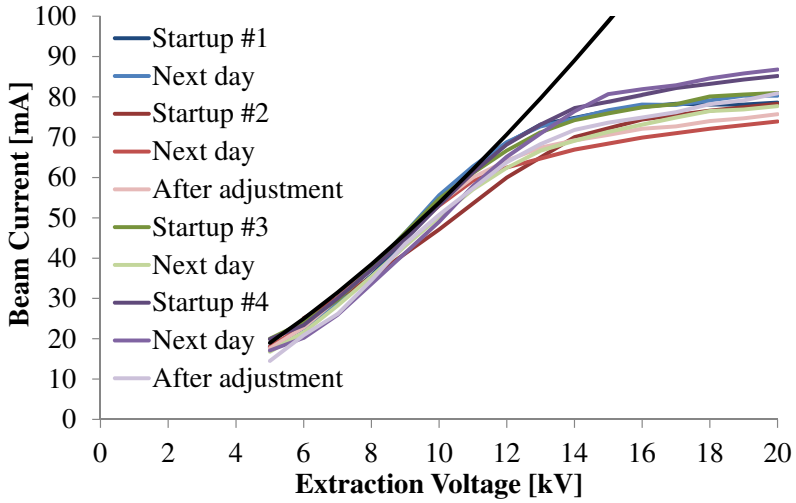

Figure 7.4: Pervance stability at a constant 50 A arc, with the beam current measured at ten different times during several days' operation and with multiple source startups. Black line is the same Child-Langmuir perveance curve shown in Fig. 7.3.

slightly to recover the beam current, but nevertheless the 'immediate' result cannot always be trusted. Temperature has an enormous effect on Penning H^- ion source stability, so if every milliamp counts, as in some facilities, then it is useful to know that the VESPA source had plenty of overhead. The ISIS operators tune the ion source most days to maintain the source performance. When the performance is no longer satisfactory for neutron production, a source change is required. If a high proportion of the total extracted beam is transported successfully using the new VESPA einzel lens, beam current should no longer be a limiting factor for ISIS operations, so source changes should become much less regular. To determine the beam transportability, the next section discusses emittance scans of the baseline extraction.

7.1.4 Emittance Scans

The emittance was measured using horizontal and vertical 'slit-slit' emittance scanners using acquisition and analysis software previously written by the author [129]. The emittance scanners had a position resolution of 38 μm and an angular resolution of 4 mrad. For the large, unfocussed beam measured in this section, 0.5 mm position steps were sufficient to measure the emittance. An example plot is shown in Fig. 7.5.

The emittance scanner centre positions were aligned accurately to the vessel datum location, therefore the peak offset was not due to the emittance hardware. Instead, because of the very small size of the ion source, a puller electrode alignment error of

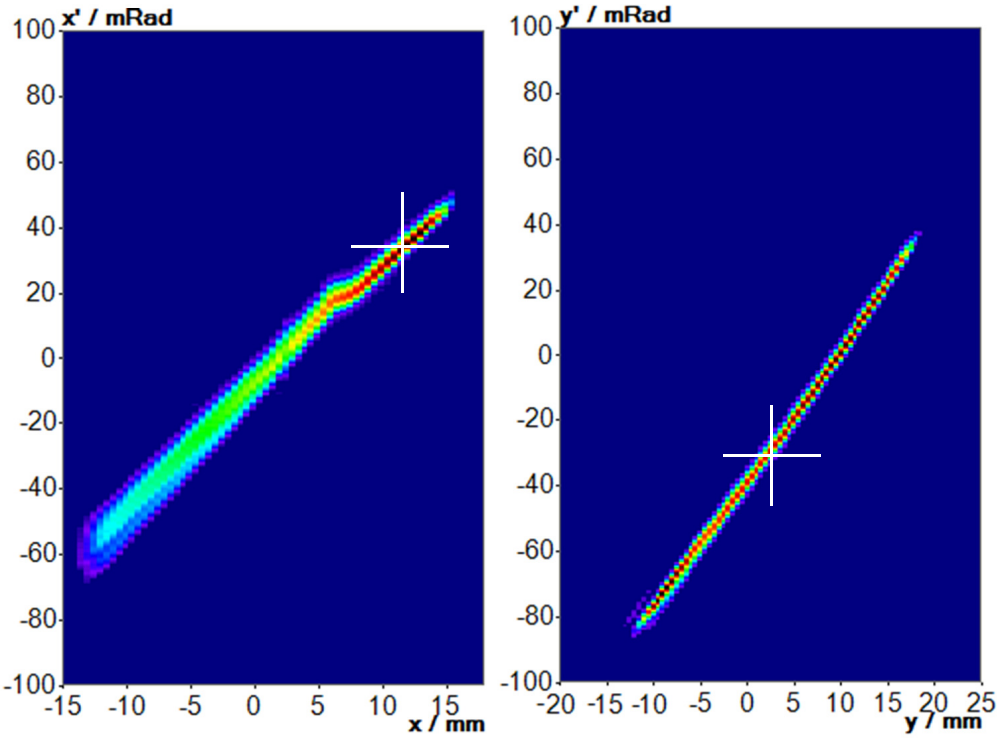

Figure 7.5: Example horizontal (left) and vertical (right) emittance plots for baseline plain diode extraction. Linear colour scale applied, whereby dark red is the maximum beam intensity. Beam centroid position marked with cross-hairs.

0.1 mm was enough to cause the 40 mrad horizontal beam angular misalignment seen in Fig. 7.5. After a drift of 250 mm to the emittance scanners, this angular offset resulted in the 10 mm position offset observed. This example shows the importance of using a microscope to align the puller electrode with the plasma outlet aperture. A microscope is used on the ISIS operational sources, but it is not yet set up to accept the different ion source flange used on the VESPA, meaning the puller had to be aligned by eye. Clearly this would be unacceptable for a source operating on a real user facility, so the microscope would have to be modified; but it was sufficient for this lab measurement campaign. The beam was off-centre vertically because the ion source was tilted by 12° around the x axis in order to achieve an on-axis beam when the new post-extraction elecrodes were installed later, as described in Section 6.1.3. Without the new electrodes installed, the beam was not given the additional vertical deflection by the einzel lens to bring it on axis.

Figure 7.6 shows how the emittance varied with extraction voltage for a range of arc currents. The horizontal emittance was fairly constant, whereas the vertical emittance decreased with extraction voltage. This is in qualitative agreement with

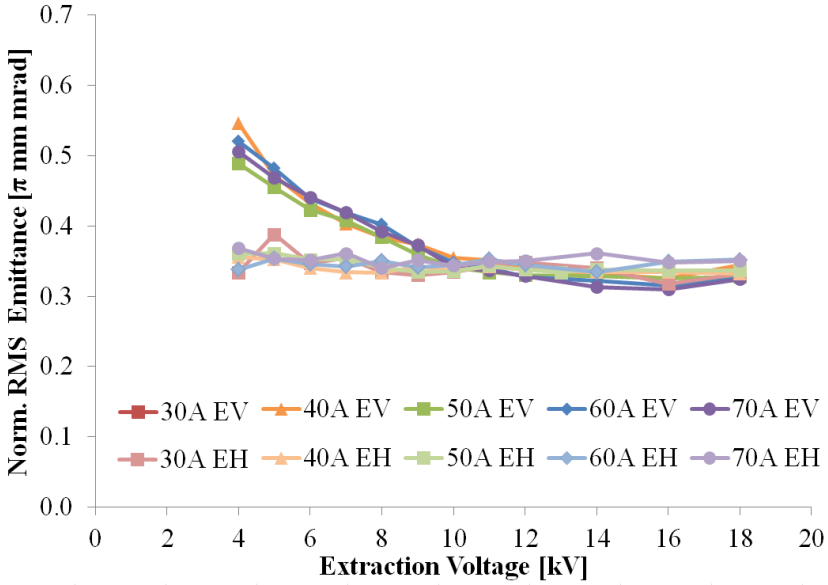

Figure 7.6: Horizontal (EH) and vertical (EV) emittance as a function of arc current and extraction voltage.

the simulation results shown in Fig. 6.4. The decreasing vertical emitance can be understood by considering that the VESPA ion source was tilted at an angle of 12° to counteract the vertical steering effect of the permanent magnet Penning field. As is discussed in Section 6.1.3, this angle was optimised to give an on-axis beam at around 17 kV extraction when the einzel lens was installed. Extraction at lower voltages caused beam deflection upwards by the magnetic field, far from the central axis. The beam became significantly smeared out, resulting in a large emittance.

With the extracted beam current and emittance measured to agree well with particle tracking simulations, the new einzel lens and other post-extraction electrodes were installed with confidence of their performance.

7.2 Einzel Electrode

7.2.1 Commissioning

As described in Section 6.1, the einzel should nominally operate at around 4 kV and should suffer minimal beam-loss. This assumes that the puller is already operating at 17 kV and the platform at 35 kV. However, during set-up the voltage needed *conditioning* so was ramped up slowly to the set point. During conditioning phases, the beam wasn't optimally focussed, so beam-loss was inevitable. Assuming in the worst case that the entire beam was dumped on the einzel, a reversible power supply

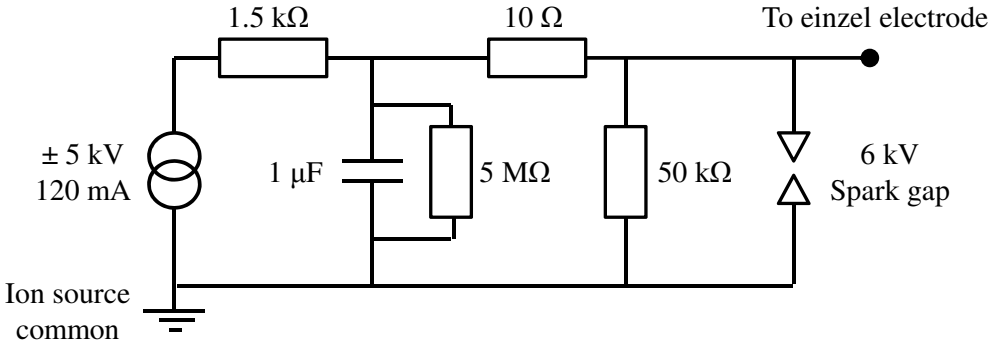

Figure 7.7: Circuit diagram of einzel electrode conditioning and protection.

was chosen to have maximum output voltage and current of ±5 kV and 120 mA, respectively. During commissioning of the einzel, it became clear that even with this current capacity, the power supply alone was insufficient to hold the set voltage. The proximity of the einzel to the puller with a pulsed voltage rate of change $^{dV}/_{dt}$ induced a large capacitive current, I on the einzel as

$$I = C\frac{dV}{dt} \tag{7.2.1}$$

where C is the capacitance between the electrodes. With the extraction power supply delivering short 17 kV pulses with ramp up and down times of approximately 20 μs, a capacitance between the puller and einzel electrodes of only 70 pF was sufficient to exceed the current capability of the power supply. Note that this was in addition to the beam current dumped on the electrode. To overcome this problem, a 1 μF reservoir capacitor was installed, along with series 1.5 kΩ and 10 Ω resistors to protect the power supply and capacitor from backlash currents when the capacitor was charged and discharged. As a personnel safety feature, a 5 MΩ bleed resistor across the capacitor terminals ensured it discharged to ground within 30 s of being powered down. A 6 kV spark gap was installed in parallel to protect the capacitor and einzel power supply in the event of a high voltage breakdown from the 35 kV power supply. The circuit is shown in Fig. 7.7.

7.2.1.1 Power Bleed Resistor

Preliminary tests with the circuit described showed that, although the reservoir capacitor successfully removed ripple from the pulsed extractor, the einzel power supply was still being pulled up by negatively charged particles hitting the electrode. This was proven by the fact that, when the polarity of the einzel power supply was reversed, it was capable of holding zero set volts and was not pulled up by the other

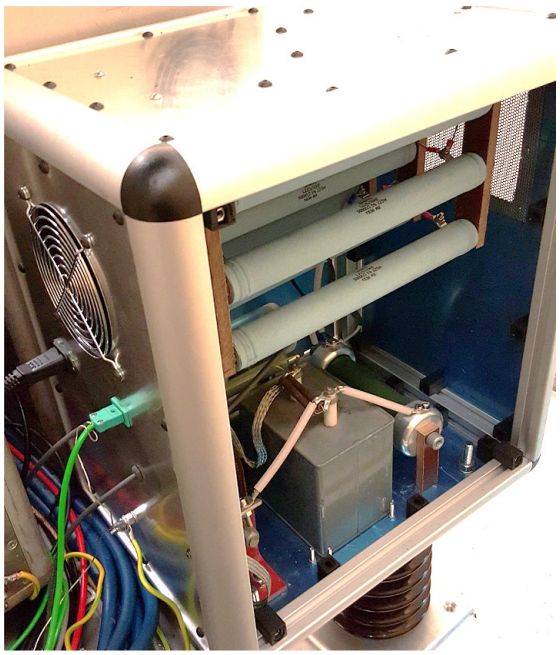

Figure 7.8: Photograph of the einzel lens high voltage circuitry.

power supplies or stray negatively charged beam particles. Therefore, ideally a four-quadrant *bipolar* power supply was needed: one which could deliver a positive voltage whilst sinking negative current. High voltage, high current bipolar power supplies are extremely rare and expensive. The alternative solution implemented by the author was a power bleed resistor network consisting of a suite of nine 50 kΩ, 225 W, 3 kV resistors in a 3 x 3 series-parallel array. Located in parallel with the spark gap, the einzel power supply sourced a constant high positive current through the resistor array which opposed the negative current of particles returning from the electrode. Only if the returning negative current exceeded the outgoing positive current would the power supply begin to float and be unable to hold the set voltage.

The 50 kΩ bleed resistor was designed to pass 100 mA of current at 5 kV: a maximum power of 500 W. This was an enormous power to dissipate over a single resistor. Instead, with the power and voltage distributed across a 3 x 3 array, this resulted in a maximum power of 55 W across each resistor: well below their 225 W rating. Generous 50 mm air gaps were left between resistors and forced air cooling was applied to remove the heat. The power bleed resistor array worked perfectly at allowing the einzel to operate at any voltage, but the drawback was its size. Coupled with the other large resistors, capacitor and spark gap, the circuit was housed in a box of similar size to the extraction capacitor, as shown in Fig. 7.8.

7.2.1.2 Reducing Spark Rate

The einzel electrode inserted between the puller and ground electrodes was in a region of high electric field. The geometry was designed in IBSimu and Opera3D as a compromise between good beam performance and minimising electric field enhancement. Nevertheless, initial commissioning showed an unacceptably high spark rate of several times per minute. This was attributed mainly to corona discharge on the einzel support legs. Although the legs were more than capable of holding off 35 kV, beam-loss was not included in the simulations. Beam-loss tends to lead to secondary electron emission from surfaces, often highlighted by insulators glowing blue with corona discharge. Corona can in turn lead to avalanche breakdown and enhanced spark rates. Sparks were also often seen on other parts of the einzel assembly. To combat sparking, the following modifications were made:

- Mounted einzel ceramic insulators on main ion source flange, so insulators only needed to stand off a few kV, rather than the whole 35 kV.
- Einzel support frame extended to move ceramic insulators and connection wire far from beam region.
- Increased gauge of connecting wires to reduce field enhancement.
- Increased gaps between puller, einzel and ground electrodes.
- Re-designed protection and ground electrodes with a conical shape to concentrate high electric field strength only where needed.
- Puller electrode mount re-designed for a thinner cross-section to increase gap to einzel, plus the addition of triple-junction shielding.

The newly designed puller, einzel and protection electrode assembly is shown in Fig. 7.9, which can be compared with the original high voltage design in Fig. 6.10. With the listed mechanical modifications, the spark rate was reduced by a factor of over 300, with high voltage breakdowns occurring once every two hours or so. This significant improvement allowed for a comprehensive measurement campaign of detailed emittance scans, which may each take up to 30 mins, depending on the resolution. However it still needs further improvement for routine ISIS operations, where only a few sparks per day can be tolerated.

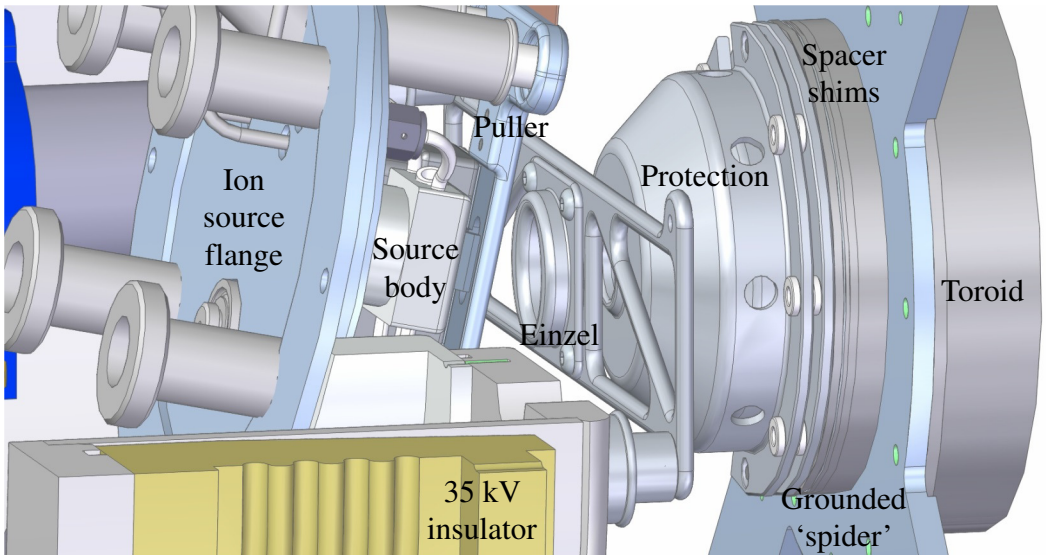

Figure 7.9: CAD model of the einzel lens modified to reduce sparking.

7.2.2 Measurements

The ion source was tuned to provide a stable, quiescent 250 μs long H^- beam pulse at 50 Hz repetition (rep.) rate. The source ran continuously at an arc current of 60 A until the end of its life after 39 days. Operating the ion source in this manner ensured stable beam and source temperatures such that the measured beam current and emittance were constant and reliable. The final beam energy was maintained at 35 keV by conditioning the high voltage carefully to the required operating level.

The einzel and extraction voltages were adjusted and the beam current and emittance were measured at each voltage setting. Figure 7.10 shows how the beam current improved as the einzel voltage was increased. This behaviour was as expected since lower einzel voltages increased the focussing strength, leading to over-focussing and beam-loss. Note that the transported H^- beam current of nearly 80 mA was exceptionally good at the 18 kV design voltage when compared with the raw extracted beam current of 85 mA in Fig. 7.3: a transport efficiency of 94%. On the other hand, significant beam-loss occurred at lower extraction voltages where the beam was steered off-axis by the Penning magnetic field and was sub-optimally focussed. Nevertheless, the einzel lens still provided sufficient beam current for ISIS linac operations at these low voltages: a much more flexible system than possible using the existing dipole magnet.

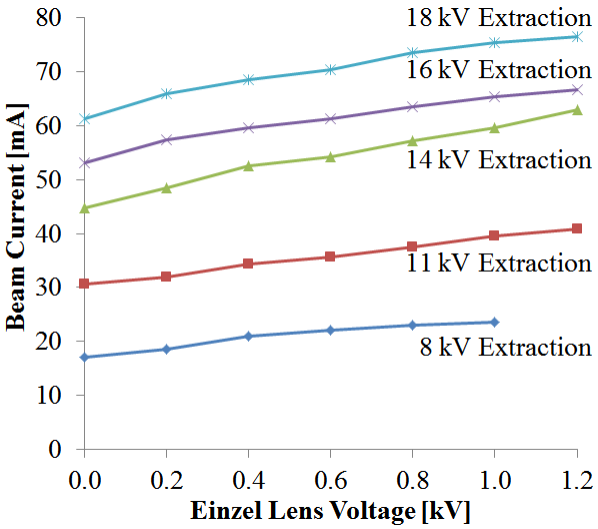

Figure 7.10: Measured transported beam current as a function of einzel voltage, for a range of extraction voltages at 60 A arc current.

The missing data point in Fig. 7.10 at 8 kV extraction and 1.2 kV einzel voltage was due to a sudden onset of sparking at that setting. IBSimu simulations confirmed that the strong vertical deflection off-axis at low extraction energy, combined with the focussing effect from the einzel lens, led to the beam being tightly focussed onto the protection electrode, suffering severe beam-loss. This would have led to significant secondary electron emission and hence high-voltage breakdowns. Interestingly, pushing through to einzel voltages above 2 kV defocussed the beam sufficiently to curtail electron emission and again bring spark rates down to acceptable levels.

Figures 7.11 and 7.12 show how the emittance varied with extraction and einzel voltage, where only a small number of measurement points are shown for clarity. The effect of the elliptical einzel aperture can be seen in Fig. 7.11, whereby the beam was strongly focussed horizontally at low einzel volts, whereas the vertical phase space varied much more subtly. The quantitative variation in emittance and phase-space orientation is more clearly seen in Fig. 7.12, which matched closely the expected performance shown in Fig. 6.9. Specifically, the beam was small (low β) and with low divergence (α close to zero) in the horizontal plane at high extraction voltages, with the drawback of higher horizontal emittance. On the other hand, extraction at lower voltages led to a greater variation of Twiss parameters with einzel voltage, which meant that the phase space orientation could be adjusted over a wide range to match into the following accelerator component.

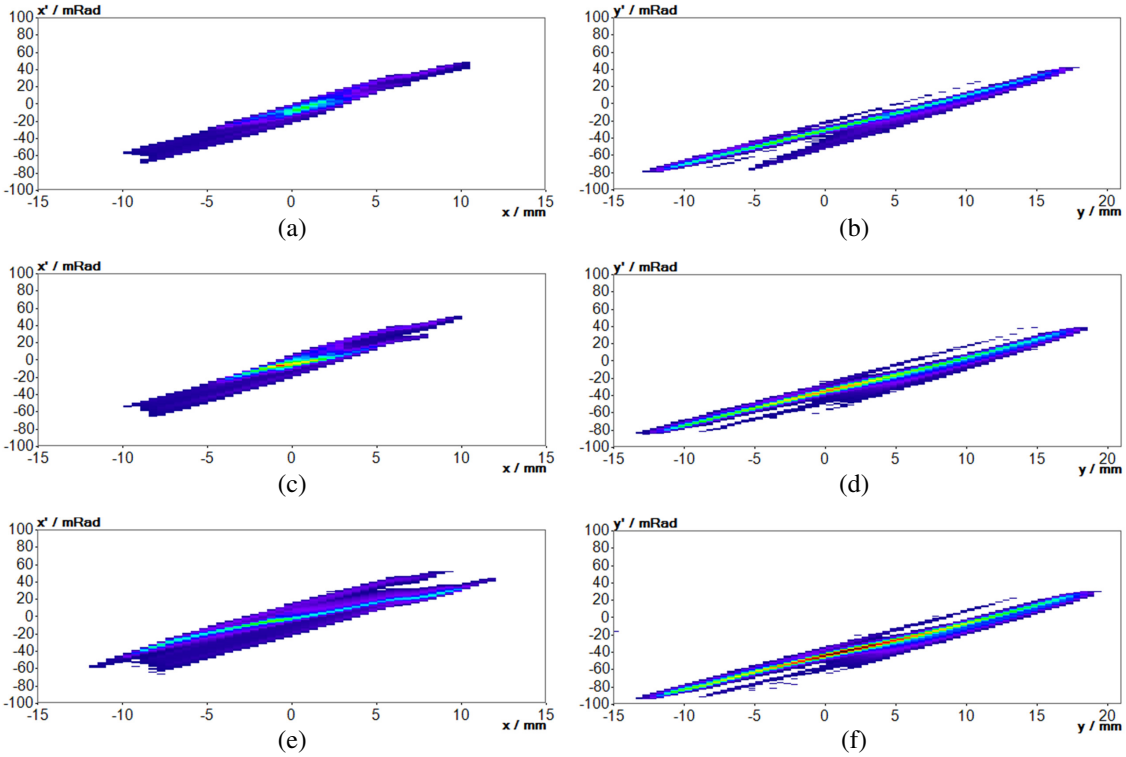

Figure 7.11: Horizontal (a, c & e) and vertical (b, d &f) emittance scans at 14 kV extraction voltage and 60 A arc current. Einzel lens set to 0.0 kV (a & b), 0.6 kV (c & d) and 1.2 kV (e & f). Colour scaling kept constant throughout to emphasise the increasing beam intensity shown in Fig. 7.10.

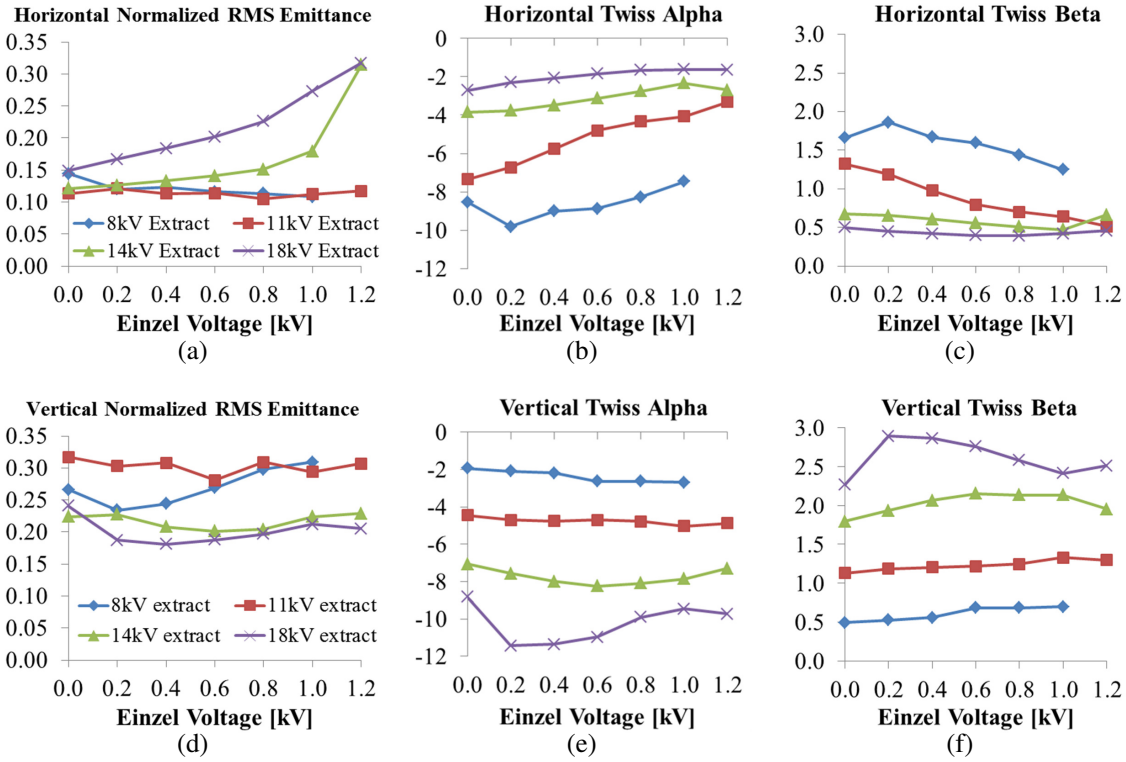

Figure 7.12: Measured emittance and Twiss parameters as a function of einzel voltage, for a range of extraction voltages at 60 A arc current.

Vertically, one must be more cautious when interpreting results. The Twiss parameters in Fig. 7.12 show a larger, more divergent beam at higher extraction voltages. However, recall that Fig. 7.10 demonstrated excellent beam transport at higher extraction energies. It turns out that, although the overall Twiss parameters appeared 'better' for the beam extracted at low energy, the beam passing through the einzel lens off-centre vertically caused the beam current density to become very non-uniform and asymmetric, leading to beam-loss. Although larger, the beam was much more Gaussian-like at high extraction energy, which is easier to transport and accelerate.

Figures 7.11b,d,f show a vertical angular offset in the beam centroid. This indicates that the 12° ion source tilt angle was too steep, and beams at higher extraction energies were pointed somewhat downward, whereas the asymmetric, lower energy beams were better centred. This being the case, more work was required to centre the beam at high extraction voltage (see Section 7.3.3) and an ion source adaptor flange with a shallower tilt angle of approximately 8° should be machined. If an approximately round beam with equal divergence in both planes were required for injection into a LEBT, Fig. 7.12 shows that operating at 11 kV extraction and 0.6 kV einzel voltage would be suitable. In this case, the beam had $\alpha_x \approx \alpha_y \approx -5$ and $\beta_x \approx \beta_y \approx 1.0$ mm mrad^{-1}, normalised RMS emittance less than 0.3 π mm mrad and a beam current of 35 mA.

7.3 Chopping and Steering

7.3.1 Design

The einzel lens worked well to focus the beam whilst preserving its emittance, however the beam was not centred perfectly on the vertical axis. The permanent magnet Penning field which confined the plasma was sufficiently strong to deflect the H^- beam somewhat. Based on the simulations described in Section 6.1, a 12° vertical tilt to the ion source should have counteracted the deflection, leading to an on-axis beam at around 18 kV extraction voltage. During the design of the VESPA, it was anticipated that the tilt may not be optimal, so flexibility was built in from the start. For example, the permanent magnets may not have exactly the same strength from one source build to the next; mechanical tolerances limit the precision to which electrodes can be assembled; not to mention the fact that the deflection by the magnets depends on the beam energy (i.e. the extraction voltage) which should be varied to suit the desired perveance.

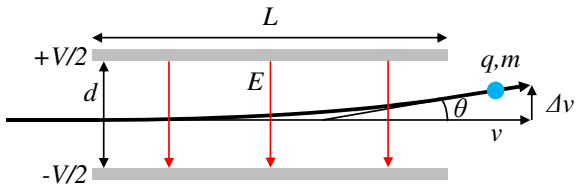

Figure 7.13: Principle of an electrostatic steerer. Parameters described in main text.

Therefore a scheme was devised by the author to enable fine-tuning of the beam's vertical position. A pair of electrostatic steering plates, shown schematically in Fig. 7.13, was housed inside the ground electrodes just before the beam current transformer toroid. The deflection angle, θ of a particle of charge q, mass m and input velocity v entering an electrostatic deflector is simple to determine by considering the force exerted by an electric field, E:

$$F = ma = Eq = \frac{Vq}{d} \tag{7.3.1}$$

with V being the potential difference between two parallel plates separated by a distance d. The acceleration in the deflecting plane, a is equal to the rate of change of velocity in the deflecting direction $a = {}^{\Delta v}/_{\Delta t}$, where Δt is the time taken for the particle to traverse through the deflector. Inserting acceleration into Eq. 7.3.1 gives

$$\Delta v = \frac{Vq\Delta t}{md} \, . \tag{7.3.2}$$

The time taken to pass between plates of length L is $\Delta t = {}^{L}/_{v}$. The angle between input and output velocities is given by $\tan\theta = {}^{\Delta v}/_{v}$. Combining equations and considering that the angle is small since $\Delta v << v$, the total deflection angle is

$$\theta = \frac{VqL}{mdv^2} \, . \tag{7.3.3}$$

Equation 7.3.3 shows that for a given deflector voltage and particle velocity, larger deflection angles can be achieved by using long plates with a small separation. On the other hand, the VESPA deflector plates needed to be positioned in a region of high space charge forces and with a beam of variable size. To avoid impingement of the H^- beam on the plates, a compromise was made with $L = 30$ mm and $d = 20$ mm. With this set-up, a 35 keV H^- beam with an angular misalignment of up to 21 mrad could be corrected with a potential difference of 1 kV between the plates. In the VESPA case, this was achieved by applying equal and opposite voltages of ± 500 V to the plates.

As well as correcting for slight beam misalignments, the deflector concept was extended to include *chopping*. Particle beams are often chopped to remove some portion of the bunch. The most common reasons to chop are to alter the bunch length [130], to clean up the rising and falling edges of a bunch [131] or to produce a train of mini-bunches which fit inside the RF 'buckets' of an accumulator ring or synchrotron [132, 133, 134, 135]. A dedicated 'fast' chopper will be installed on ISIS as part of the medium-energy beam transport (MEBT) upgrade [128]. The VESPA deflector system presented an ideal opportunity to prototype the MEBT chopper electronics.

The application of the chopper on the VESPA was to modify the beam rep. rate. During set-up of the ISIS accelerator, the machine is operated at low rep. rates such that integrated beam-loss (and subsequent radioactivation) throughout the machine is minimised. In practice, it is the rep. rate of the ion source extraction voltage pulse which is adjusted, such that beam is only produced when needed. Maintaining a high temperature of the puller electrode is crucial to reduce caesium contamination (see Section 6.3). Reducing the extraction rep. rate means the average electron power load – and hence electrode temperature – on the puller is reduced, so caesium accumulates much more readily. It is often found that the extractor suffers significant sparking after prolonged periods of low rep. rate operation due to caesium contamination; this can adversely affect the lifetime of the ion source and its ancillary equipment. Therefore, the author proposed using the VESPA deflector as a chopper to remove some H^- beam pulses, such that the remaining pulses enter the accelerator at arbitrary rep. rates. In this case, the extractor could be maintained at the normal 50 Hz rep. rate to ensure ion source stability, whilst varying the beam rep. rate via the chopper. Used in this manner, the chopper would need significant interlocking to protect the machine from unexpected 50 Hz beams should the chopper fail. For example field-monitoring pick-ups could be implemented to confirm the presence of a chopping voltage. If the voltage were not present, an interlock would trip, shutting down the extraction power supply and preventing beam being made.

To remove a beam pulse completely, it must be deflected enough such that the chopped and unchopped beams do not overlap in phase-space. Since the plates were oriented for vertical deflection to correct for vertical misalignment, the beam must be deflected by over 200 mrad to avoid overlap with the yy' emittance data presented in Fig. 7.11. Using Eq. 7.3.3, it can be shown that to achieve this deflection, ± 5 kV was required on each plate.

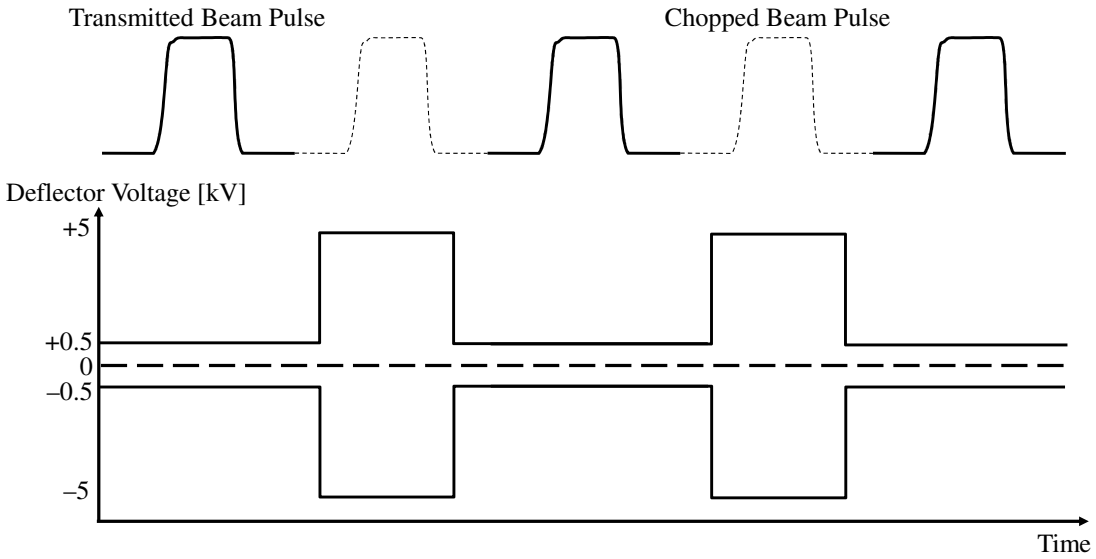

Figure 7.14: Schematic of the proposed chopping scheme. A low DC voltage is applied to both deflector plates to correct any beam misalignment. A high voltage pulse is applied when required to completely remove a beam pulse. In the given case, the chopper is set to transmit beam pulses at half the normal repetition rate.

7.3.2 Hardware

The steering and chopping scheme is demonstrated in Fig. 7.14. A relatively low voltage was applied constantly to the deflectors to fine-tune the vertical beam alignment by some tens of mrad. If a beam pulse must be removed completely, a high voltage chopper pulse was superimposed on the low-voltage base level. Steering and chopping voltages could be adjusted independently of each other. The positive and negative plates were also independent, so the user could set one to +4 kV and the other to -6 kV to achieve the same chopping electric field if desired. However to maintain symmetry and to halve the number of remote control outputs, it was assumed that the user would set equal and opposite voltages.

The deflector hardware consisted of three components: a power supply, the drive electronics and a pair of high voltage switches. A four-channel 19" rack-mounted crate manufactured by UltraVolt is shown in Fig. 7.15. It contained positive and negative, low and high voltage power supplies for the steering and chopping functions, respectively. The maximum steering and chopping voltages were ± 1 kV and ± 6 kV, respectively, to allow for overhead in case the values obtained from Eq. 7.3.3 were incorrect.

Figure 7.15: Chopper drive electronics crate (top) and UltraVolt four-channel high voltage power supply crate (bottom).

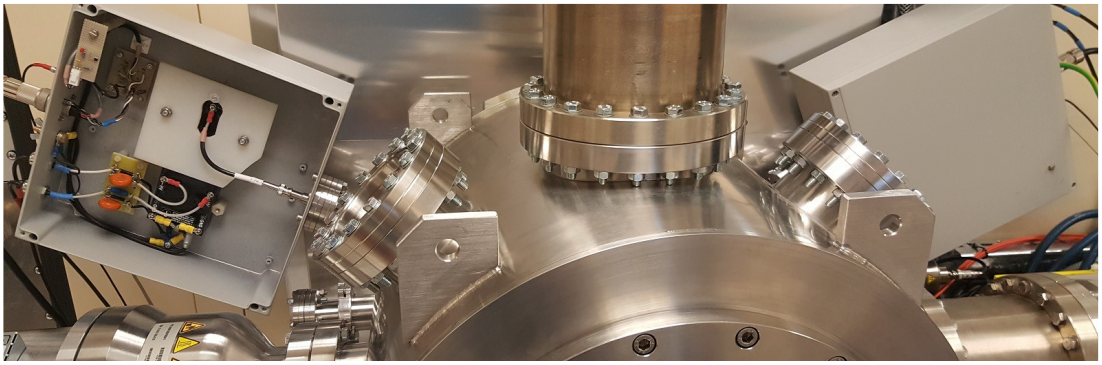

Figure 7.16: Chopper switch boxes attached to VESPA vacuum vessel. Positive box (left) is open to show internal circuitry, including the Behlke switch.

A drive electronics 19" rack-mounted crate, also shown in Fig. 7.15, was manufactured by an ISIS electrical engineer to ensure personnel interlocks were correctly implemented (ensuring, for example, that power was cut should a panel be opened). It also received timing signals from the ISIS control system and formed a TTL trigger pulse for the chopper high voltage switch. The TTL pulse was programmed with a back-up off ensuring that its pulse length could not exceed 3 ms, even in the event of ISIS control 'off' signal failing. A latching key switch completed the drive electronics, meaning that even if the interlocks and timing systems were enabled, a drive pulse wouldn't be output until a user was present to physically turn the key and enable the system. Assuming all was nominal, however, the drive electronics crate represented a 'black box' and required no further user intervention.

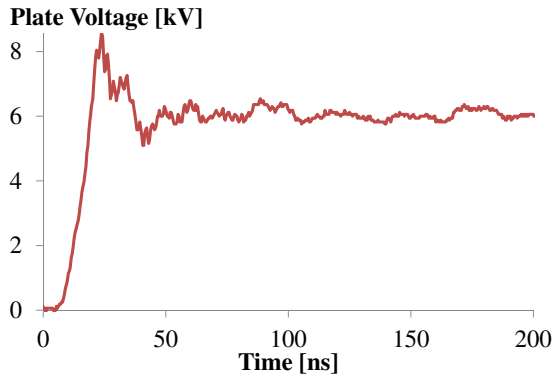

Figure 7.17: Rising edge of the voltage pulse measured on the positive chopper plate.

Fast Behlke high voltage switches formed the final component of the chopper electronics. Taking a TTL pulse from the drive circuitry and a high DC voltage from the UltraVolt crate, a Behlke switch transmitted a high voltage pulse to a chopper plate inside the vacuum vessel. The switch was housed inside an interlocked box mounted directly onto the vacuum vessel. There were two such boxes: one for the positive pulse and one for the negative pulse. The push-pull switches were specified to achieve equal rise and fall times of around 10 ns, depending on the load capacitance. The VESPA chopper plates were designed to minimise both the length along the beam direction and the voltage required to deflect the beam. This being the case, they were not designed specifically for minimum capacitance to ground, so it was expected that they would affect the chopper rise time adversely. On the other hand, cable inductance was minimised to limit further degradation of rise time by using short cables and mounting the boxes containing the switches.

Figure 7.17 shows the voltage pulse measured directly on a deflector plate inside the vacuum vessel using a high voltage probe and a fast oscilloscope. It can be seen that, despite the added load capacitance and cable inductance, the chopper rise time was still around 24 ns. The ripple at the start of the pulse was due to the internal circuitry inside the Behlke switch attempting to provide the fastest possible rise time. External components could be added if necessary to minimise the ripple, but no beam diagnostics on the VESPA had fast enough response to operate on nanosecond timescales, so no effect could be observed either way. Besides, the purpose of the VESPA chopper was to remove an entire beam pulse, so the rising edge of the chopper was somewhat irrelevant, being always before the start of the beam pulse. Rise time will, however, be important to consider in the future MEBT chopper.

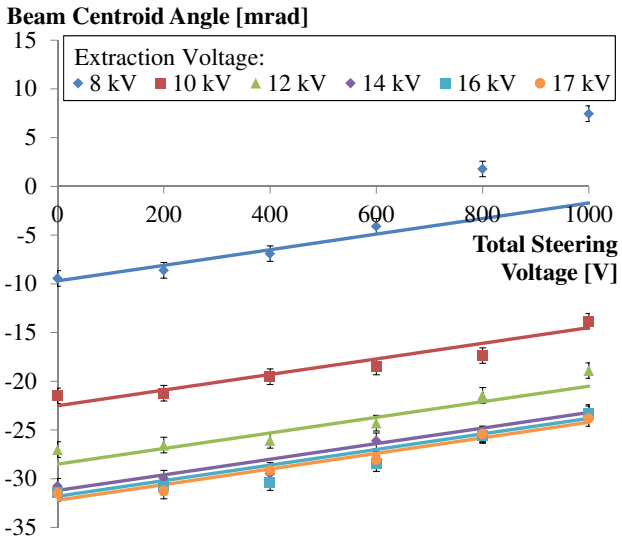

Figure 7.18: Dependence on beam centroid angle with steering voltage for a range of ion source extraction voltages. Beam centroid is defined as the centre of mass of the beam phase space. Best fit lines all have gradients of 8 mrad kV^{-1}.

7.3.3 Results

The chopper boxes were installed on the VESPA and timing signals provided from the ISIS control system. The ion source puller was maintained at 50 Hz rep. rate, whilst the chopper rep. rate was varied independently. The einzel lens was maintained at 3 kV. Figure 7.18 shows that the steering effect was linear at 8 mrad kV^{-1} and independent of the ion source extraction energy, so long as the extraction was greater than 10 kV. The einzel lens and post-extraction system was designed to operate with extraction voltages around 17 kV; within a few kV of the nominal, the beam was focussed properly by the einzel lens and passed through the steering electrodes relatively on-axis. At low extraction voltages, the beam was displaced upwards sufficiently by the einzel field that, by the time it arrived at the steerers, it was in too close proximity to the top plate and suffered a non-linear steering effect.

Although the steering angle linearity was good, the gradient was less than half of the 21 mrad kV^{-1} expected from Eq. 7.3.3. There are a number of effects which could explain this discrepancy. Firstly, the *aspect ratio* (i.e. the ratio between plate length and separation) of the steerers was somewhat small. Equation 7.3.3 assumes long plates with a uniform, purely transverse electric field throughout. Since the gap was large relative to the length of the plates, the E-field between the VESPA steerers likely had significant *end effects*, meaning it only had a relatively small region in the

middle with a uniform E-field. It could surmised that the integrated field experienced by a particle was around half that required to steer the beam to a required angle. However IBSimu simulations of the steering effect, shown in Fig. 7.20, showed a linear relation between voltage and steering angle, with a gradient of 19.6 mrad kV^{-1}. This is only 7% lower than the theoretical 21 mrad kV^{-1}, which implies that end effects only provide a marginal contribution to the low measured steering gradient.

Another source of the discrepancy may be from particles impacting the deflector plates. The transmitted beam current sometimes reduced up to 10% when operating the steerers, indicating beam-loss on the plates. The lost beam current would result in a reverse current flowing back into the power supply. Much in the same way that the einzel lens could not achieve a set voltage originally due to beam loading (see Section 7.2.1), the steering and chopping power supplies sometimes struggled to achieve a set voltage. In addition, beam-loss on the plates might also have caused secondary electron emission, whose space charge would further affect the overall steering electric field. Secondary electron emission could be included in IBSimu, and the beam space charge could be adjusted manually to replicate the effect of space charge compensation from residual gas ionisation. Alternatively, space charge compensating positive ions could be introduced artificially to a simulation, but not generated procedurally from Monte-Carlo collisions with beam particles. Similarly, poor voltage-holding due to beam-loss on the deflector plates could not be simulated. These limitations in IBSimu precluded the possibility of investigating subtle causes of low deflection angles. Secondary electron emission may have actually been observed when the measured current on the toroid sometimes *increased* around 10% when operating the steerers: a current of secondary electrons may have been added to the H^- beam current. However it is difficult to prove this, since the beam current signal may also have increased purely because the beam was being steered and hence had better transmission through the toroid. Whether the measured beam current increased or decreased depended on the extraction, einzel and steering voltages.

With the low voltage steering effect seen to work, albeit not as effectively as required, the high voltage chopper pulses were tested with beam. The chopper was designed to achieve deflections of around 200 mrad, which would separate the chopped and un-chopped beams in phase-space. The angular deflection would have led to a measurable real-space separation of 20 mm after a 100 mm drift. Therefore (apart from a small change in beam current due to beam-loss discussed above), the chopping

efficiency could not be measured using the toroid, since both chopped and un-chopped beams passed through it. One method to prove chopped beam separation would have been either multiple small Faraday cups side-by-side some distance downstream [53], or one movable Faraday cup [136]. The time and resources required to design, manufacture and test such complicated Faraday cup systems was beyond the scope of this thesis. Beam calorimeters are often used to measure beamlet separation in large Ampère-scale H^- beams for fusion applications [137, 138, 139]. Again, notwithstanding the required mechanical design effort, the small beam size and reduced temperature rise from the lower power beam would limit signal-to-noise in such a detector.

Therefore, the chopping effect was measured using the existing emittance scanners: a typical parameter scan is shown in Fig. 7.19. An emittance scan was essentially a 3D data matrix with pixel coordinates (position, angle, time). Each pixel in the displayed 2D sub-space of Fig. 7.19 was recorded from one beam pulse. Each beam pulse was sampled every 10 μs, giving the third, time dimension in the matrix; meaning one can measure how the emittance varies throughout the beam pulse. This is useful to study space-charge compensation effects in a pulsed beam, for example [140]. The chopper was pulsed at 25 Hz whilst the beam was extracted at the standard 50 Hz. Since each (position, angle) 2D pixel was gathered from one beam pulse, and every second beam pulse was deflected by the chopper, as demonstrated in Fig. 7.14, this resulted in the 'checkerboard' pattern shown in Fig. 7.19. The amount of checkerboarding (i.e. how many deflected pixels there were) was thus determined by the chopper rep. rate. With the rep. rate set at 25 Hz, one can see both the chopped and un-chopped beams quite clearly, despite only having half of the pixels displayed for each.

With the chopper set to zero volts in Fig. 7.19a, there was a clear 'tail' on the top of the un-chopped beam: a typical artifact of decel-accel einzel lenses. Note that this did not move when the chopper was on, so was truly part of the un-chopped beam. However the chopped beam did overlap and cross over the tail as the volts were increased, making the analysis more complicated. To aid with the analysis, Fig. 7.19 is labelled to indicate the displacement of notable regions of the beam: either the point of maximum intensity or of the lowest extent. The displacement of these points is plotted in Fig. 7.20, along with the expected angular deflection based on the 8 mrad kV^{-1} rate measured in Fig. 7.18. These can be compared with the theoretical deflection angle from Eq. 7.3.3 and the angles obtained from the IBSimu model.

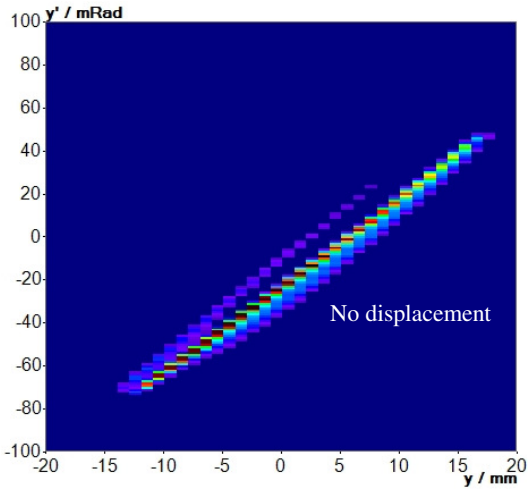

(a) Total chopping voltage = 0 kV

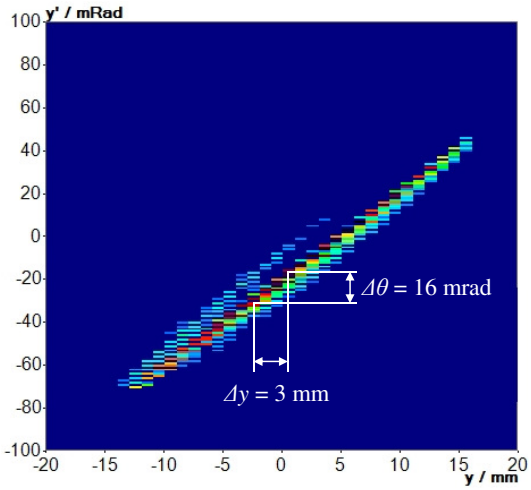

(b) Total chopping voltage = 2 kV

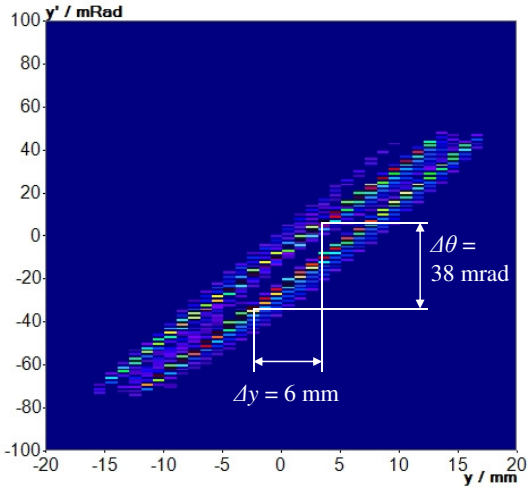

(c) Total chopping voltage = 4 kV

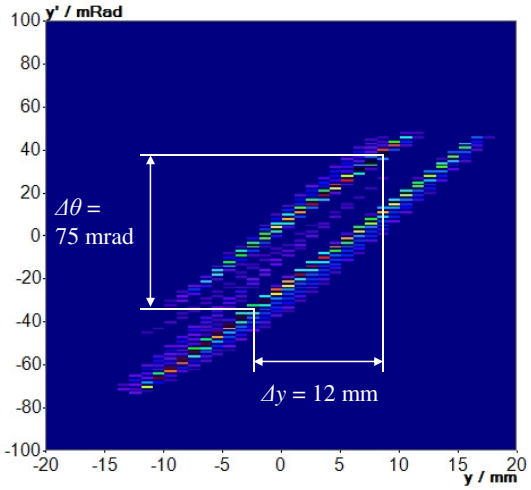

(d) Total chopping voltage = 6 kV

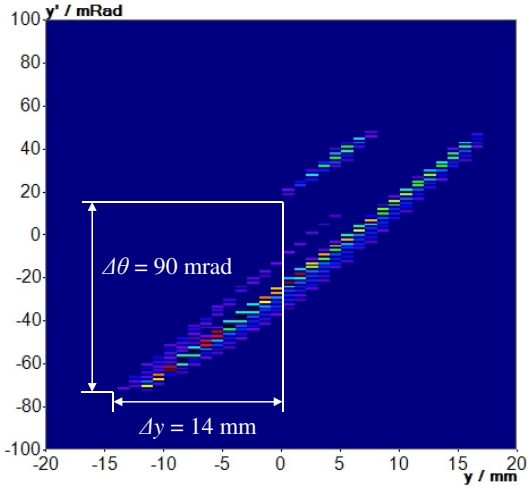

(e) Total chopping voltage = 8 kV

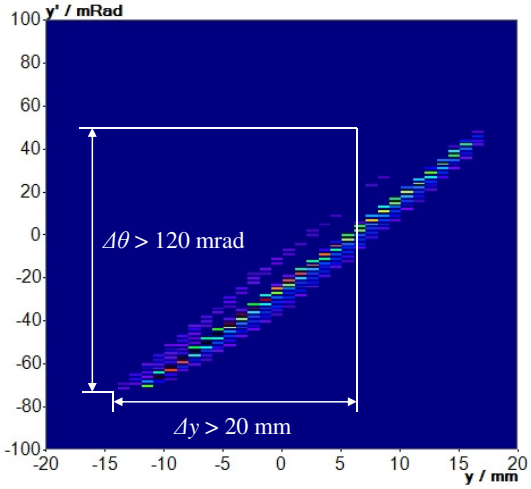

(f) Total chopping voltage = 10 kV

Figure 7.19: Vertical emittance scans of a chopped beam extracted at 14 kV and the einzel lens at 2 kV. The chopper repetition rate of 25 Hz caused the 'checkerboard' pattern in the scans, as every other beam pulse was deflected by the chopper.

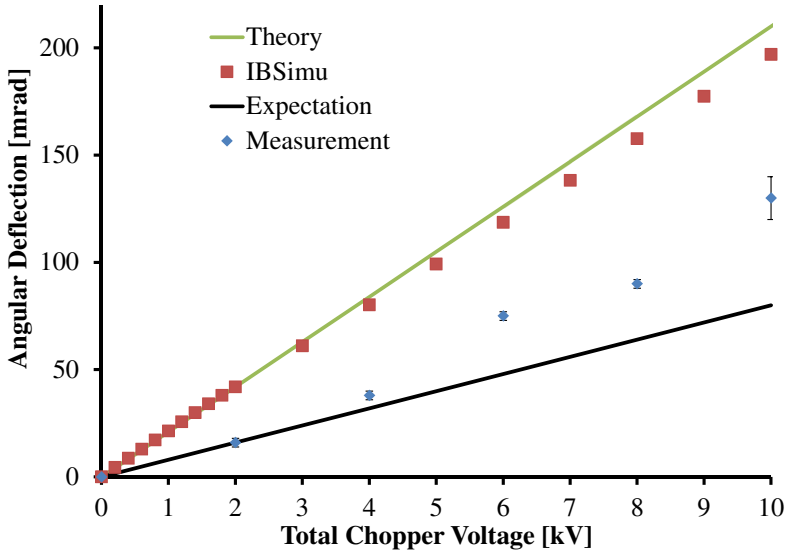

Figure 7.20: Beam centroid angular deflection as a function of the total chopping voltage applied between both deflector plates. Simulated chopping effect (red) agrees well with theoretical considerations in Eq. 7.3.3 (green), albeit with a small decrease due to end effects. Black line is an extrapolation of the 8 mrad kV^{-1} slope measured in Fig. 7.18 using the low voltage steerers. At higher chopping voltages, space-charge effects due to the proximity of the beam to the top plate caused the measured beam centroid (blue) to move away from the expected slope.

The chopper deflection continued the low-voltage linear trend displayed by the steerers. However as the chopper voltage increased above 4 kV, the angular beam deflection moved away from the expected linear value, in much the same way that the 8 kV extracted beam did under the influence of the steering voltage in Fig. 7.18. It may be concluded that the 14 kV extracted beam used in the chopper experiment underwent the same effect; in that it moved too close to the top chopper plate and was further deflected by non-linear fields. As Fig. 7.19e shows, at 8 kV chopper voltage, the chopped beam became collimated at an angle of around +50 mrad and disappeared altogether at 10 kV in Fig. 7.19f. The displacement data point in Fig. 7.20 for the 10 kV chopper voltage was estimated based on the fact that the beam became collimated at +50 mrad, so must have been deflected by at least 120 mrad to have been removed completely.

Total extinction of the beam was a surprising result. The chopper was designed to deflect the beam by >200 mrad, but nevertheless still allow it to pass through the toroid and be removed somewhere downstream before entering the LEBT beampipe. The chopped beam was indeed measured as normal by the toroid. Because of the

non-linear steering effect discussed above due to the proximity of the beam to the chopper plate and secondary electrons, the only conclusion is that some portion of the beam was lost on the chopper plate itself whilst the majority was lost on the toroid housing after being detected. IBSimu showed that up to 20% of the beam may indeed be lost on the top chopper plate, depending on the space-charge compensation and combination of extraction and einzel voltages. However this discrepancy would have been observed easily by the toroid positioned downstream of the deflector plates. Equally, the inner diameter of the toroid was four times that of the electrode apertures, so it seems unfeasible that beam could be lost on it. Regardless of where exactly the beam was removed, the chopper actually performed its job of completely chopping out the beam at the rep. rate required, so can be considered a success.

7.4 Discussion

With excellent transport afforded by the VESPA system, the beam could be generated on the ideal perveance curve, with the arc current varied to give a perfectly focussed beam. If more or less beam current was required, the extraction voltage could be varied whilst staying on the perveance curve, with the arc current adjusted to maintain focussing. At the expected operating extraction voltages greater than 14 kV, the beam position was rather insensitive to the extraction voltage, therefore a set of electrostatic steering plates was used to fine-tune the beam alignment.

Although the steerers did not have the expected deflection, the gradient was nonetheless linear and predictable, so they were a good test of the principle. The beam was directed downward slightly even when the maximum steering voltage was applied so, to bring the beam perfectly on axis, a new ion source adaptor plate should be installed with a shallower tilt angle of approximately 8°. A high voltage pulse could be applied to the steering plates at any rep. rate to chop the beam by a large angle, thus removing it entirely. The chopper worked well, as demonstrated by measuring the beam phase space with emittance scanners, however unexpected collimation led to premature beam extinction. To prove that the chopped beam was indeed removed completely, a second, independent beam current measurement should be performed downstream after the emittance scanners. A suitable toroid or Faraday cup was not available during the measurement campaign of this thesis, but will be installed in the future.

Related to the above chopping-efficiency measurement, it should be clarified where exactly the chopped beam was collimated so that un-controlled beam-loss does not cause excessive heating. For example, a 60 mA, 35 keV beam operating at 50 Hz with a pulse length of 250 μs has an average power of around 26 W. In a vacuum environment with only passive conductive and radiative cooling, this could lead to temperatures in excess of 200 °C. In particular, items such as the deflector plates, which are mounted on ceramic insulating legs with poor thermal conductivity, could reach sufficiently high temperatures to warp and fracture the ceramic. It is difficult to cool electrically-isolated electrodes (as discussed in Section 6.3), therefore prior knowledge of where beam-loss occurs would help determine the cooling power requirements.

The VESPA post-extraction electrodes worked admirably with a combination of good beam transport, low emittance, flexibility, steering, chopping and minimal sparking. However the long-term operation of the system – particularly the effect of removing the caesium trap – was required to validate it. This is the subject of Chapter 8.

Chapter 8

Long Term Operation Without a Caesium Trap

8.1 Long Term Source Stability Considerations

The extraction of a high current, low emittance, flexible H^- beam is not sufficient if it can only be produced stably for short periods of time in laboratory conditions. A successful ion source must produce quality beam for prolonged periods of time without constant tuning of set parameters. In addition, the operating conditions of the ion source should not unduly affect the rest of the accelerator; for example if high hydrogen or caesium flows are required, they could cause sparking downstream.

As such, the ISIS and VESPA ion sources are operated continuously for weeks at a time and their performances logged to monitor long term behaviour. The VESPA did not have sufficient long-term operational logs of beam production at the time of writing to give meaningful statistics, so a typical ISIS long-term log is shown in Fig. 8.1. There are several interesting features of long term operation. The arc current and extraction voltage are fixed during operation (a) since they are the primary factors determining the beam current, which should be maintained at a constant level. Immediately after turning on an ion source, it often has an unsustainably high beam current (b) due to the excess caesium flux applied to start the pulsed arc. When the caesium is reduced to normal operating levels, the beam current stabilises. The operators attempt to keep the body temperature fixed by adjusting the air cooling flow rate (c) because the beam current is very temperature-sensitive, tending to decrease when temperatures increase (d). The molybdenum anode is press-fit into the body and so should be approximately the same temperature, however differences of up to 40 °C occur between different ion sources. In the first 24 hours after a new source is

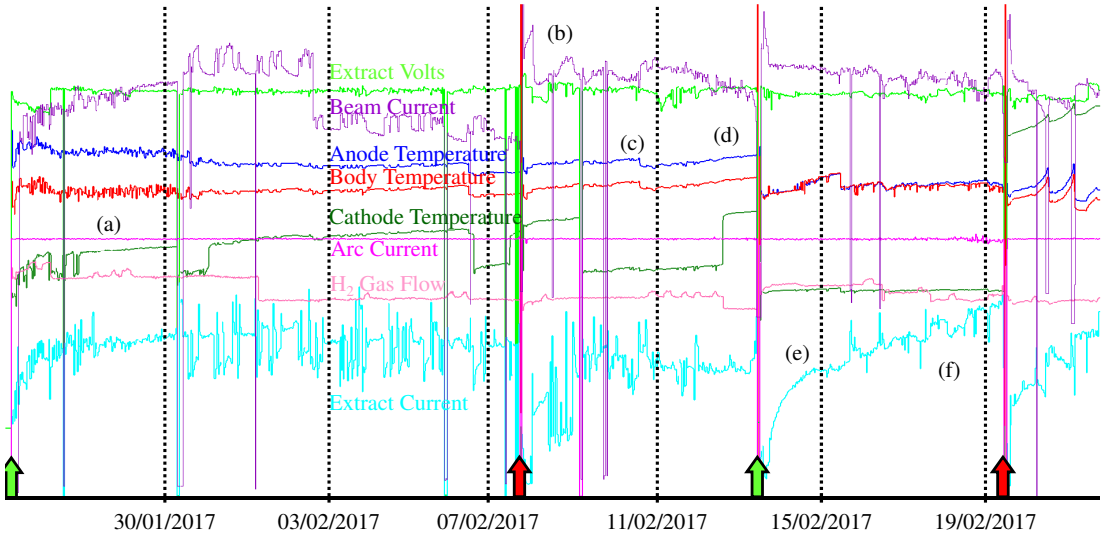

Figure 8.1: Example long-term running log of several ISIS ion sources. Installation of replacement sources marked by arrows: green and red for scheduled and unscheduled changes, respectively.

installed, the extraction current increases rapidly (e) as the plasma and puller electrodes are covered in caesium, leading to secondary electron emission. Thereafter, the extraction current stabilises and remains almost constant or has a slow increase during the source lifetime. A good indicator that an ion source failure is imminent is if the extraction current increases suddenly (f). As well as the long-term trends, there are several other factors which must be monitored and controlled by skilled operators. These include, but are not limited to, the current drawn from the 35 kV high voltage power supply; the amplitude and duration of noise or 'ringing' at the start of the arc current pulse; the refrigerator temperature of the cold box, and the shape and stability of the beam current pulse.

Ensuring that the VESPA ion source achieves the long-term stability required of ISIS is perhaps the most critical challenge. Using an elliptical einzel lens to generate a high beam current with low emittance and flexible output phase space parameters is useless if it cannot be sustained. Equally, if the new system leads to other problems such as an increased rate of high voltage breakdowns due to caesium contamination, then its practicality must be questioned. A rigorous, long-term soak-test of the VESPA is on-going for at least twelve months before it is deemed suitable for installation on ISIS. Although long-term running results are hence not available for this thesis, the impact of removing the cold box was ascertained.

8.2 Caesium Flux Measurements

8.2.1 Apparatus

A suite of vibrating mass deposition sensors was used to quantify the amount of caesium (Cs) escaping the ion source and depositing on the vacuum chamber and electrodes. Each sensor was based around measuring the resonant frequency of a quartz crystal micro-balance (QCM). Quartz is a piezoelectric crystal which deforms mechanically when an electrical potential difference is applied across it. Applying an oscillating voltage drives a resonance in the crystal in the form of a transverse shear standing wave. The resonant frequency is very stable for a given mass m of crystal at a constant temperature. Driving the crystal with a MHz oscillator, a frequency shift Δf is observed which depends on any change in mass Δm on the crystal by the Sauerbrey equation [141]:

$$\Delta f = -\frac{2f_0^2}{A\sqrt{\rho\mu}}\Delta m \tag{8.2.1}$$

where f_0, ρ and μ are the unloaded resonant frequency, the density and the shear modulus of the crystal, respectively. A is the active crystal area between the driving electrodes. Machined and calibrated to high precision, the QCMs are capable of measuring sub-Hz frequency shifts on a MHz resonance due to individual particle masses depositing on the surface.

This technology has had a wide range of applications since the 1960s, especially since the Sauerbrey equation was extended to include the effects of viscous drag in the 1980s, meaning QCMs could even be used to measure liquid interfaces [142]. Typical applications include: controlled deposition of dopants on electronic substrates or anti-reflective coating on optical lenses; controlled etch rate using laser ablation or ion beam sputtering; monitoring of humidity or petroleum vapour, and detection of protein or bacterial interactions with drugs. Therefore the detection of a high flux of Cs escaping the ion source posed no challenge to these extremely accurate sensors.

Each QCM sensor was installed on the VESPA vacuum vessel via a KF40 flange with water, air and coaxial electrical feedthroughs. The sensors were water cooled to maintain a constant crystal temperature and an air-driven pneumatic shutter at the front of each sensor ensured the crystals were exposed to the flux of particles only when required. The crystals were driven to resonance and their mass-dependent

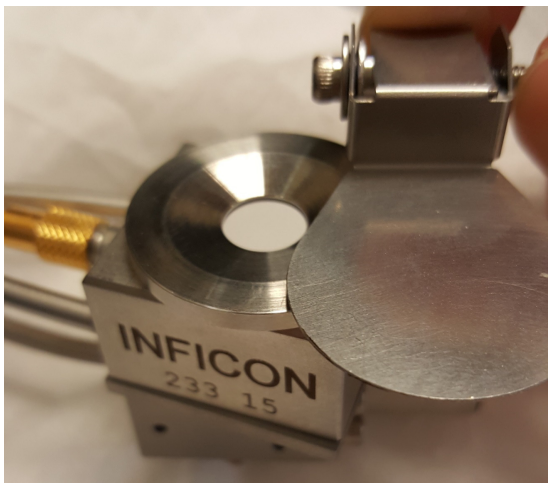

Figure 8.2: Quartz crystal microbalance sensor head with the shutter open.

frequency monitored via an in-vacuum coaxial cable connected to a nearby in-air oscillator circuit. Several types of crystal were available, each with a different electrical contact material suited for a specific application. For the high mass and high flux of Cs atoms collected, aluminium alloy crystals were chosen as the most resiliant compared to gold- or silver-coated crystals. Figure 8.2 shows the sensor head of a QCM with the shutter opened to reveal the crystal inside. The water, air and electrical connections can be seen on the left side of the photo.

Four Inficon QCM sensors were used simultaneously by mounting them on a removable diagnostics flange shown in Fig. 8.3. The sensor positions were chosen to give indicative measurements at four useful locations described in Table 8.1. Sensor 4, which was positioned on-axis as close to the ion source as possible – just downstream of the beam current toroid – measured an order of magnitude higher flux than any other sensor. This was to be expected because Cs escaping the source travelled on ballistic trajectories in a vacuum molecular flow regime. With sensor 4 having direct line of sight onto the ion source, it collected a disproportionate amount of Cs compared to the other sensors, reducing their signal-to-noise. Although a good clear signal, the high flux on sensor 4 did not inform of any unexpected physics. In fact, since it was anyway expected that the beam-focussing electrodes close to the ion source would suffer a high Cs deposition rate, and in normal operation the H^- beam would impact and potentially destroy anything on axis, sensor 4 was actually something of a hindrance. Therefore, sensor 4 was removed such that an on-axis quartz window could resume visual observations of the ion source plasma, an H^- beam could be produced safely and the remaining sensors could have improved signals.

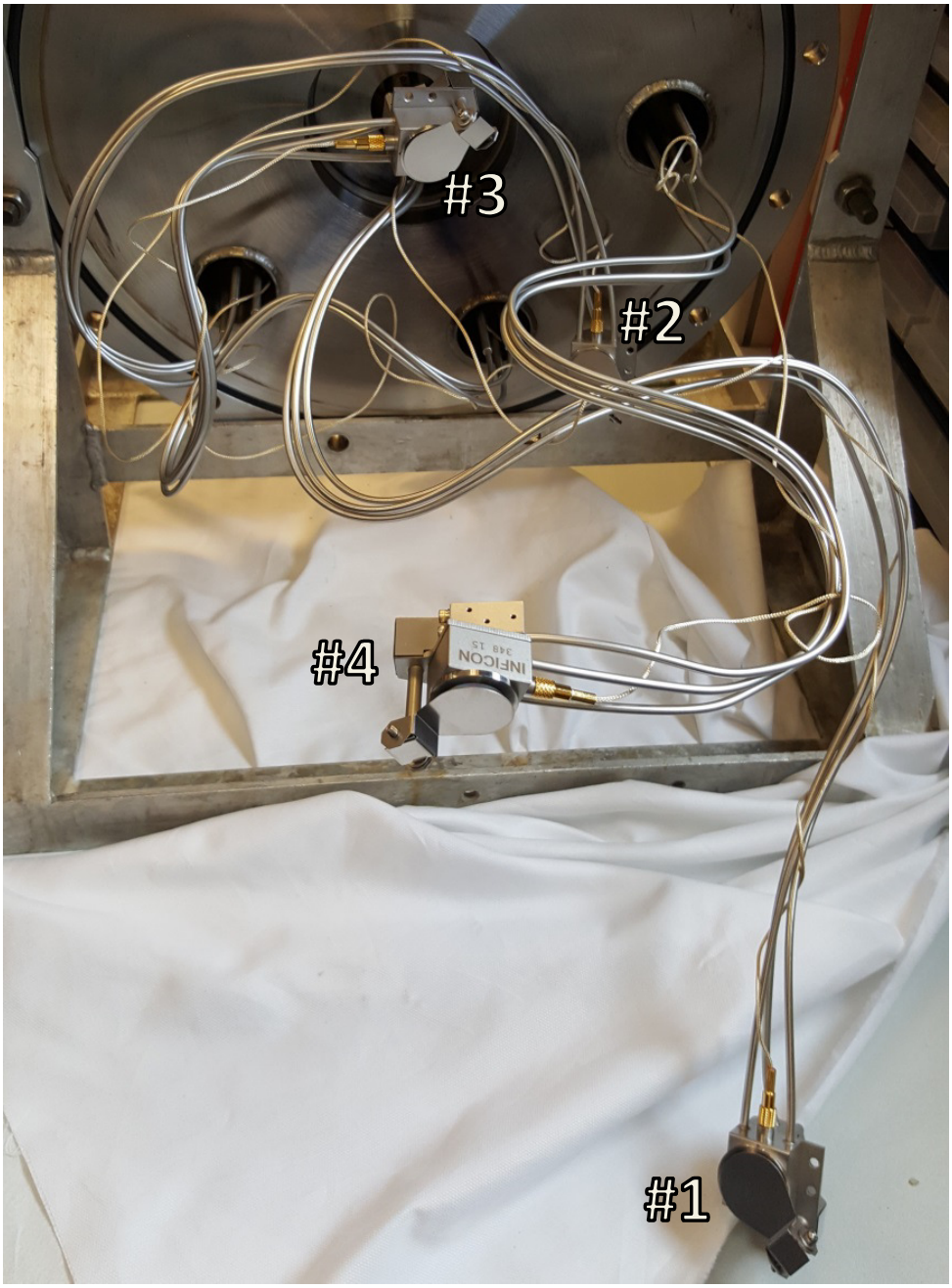

Figure 8.3: Quartz crystal microbalance sensors mounted on vacuum flange for installation on the VESPA.

Table 8.1: QCM positions inside vacuum vessel

Sensor Number	**Longitudinal Distance from Source**	**Radial Distance from Centre-line**	**Indicates Cs Flux at**
1	0 mm	260 mm	HV insulator
2	330 mm	260 mm	Vessel wall
3	450 mm	60 mm	LEBT entry
4	125 mm	0 mm	Toroid

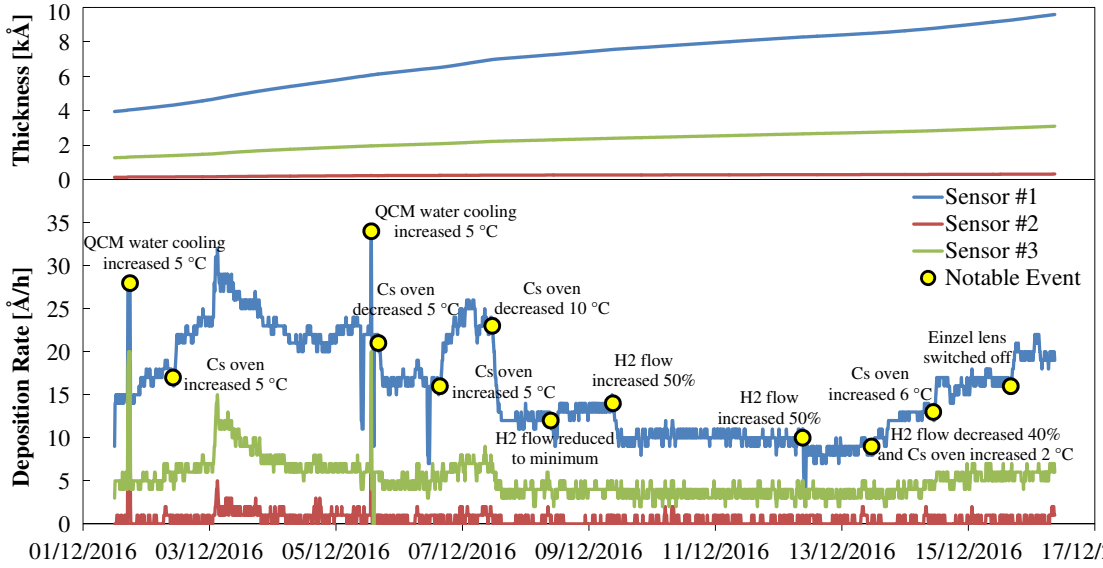

Figure 8.4: The raw measurement of deposited layer thickness on the QCM sensors is shown in the top graph. The time-derivative is shown at the bottom, with notable changes to the ion source operating parameters highlighted.

8.2.2 Measurements Without a Caesium Trap

A typical long-term Cs flux measurement is shown in Fig. 8.4. The sensors and associated electronics directly measured the deposited thickness on the quartz crystal through Eq. 8.2.1. However a plot of the thickness over time is quite unhelpful, as it simply consists of an increasing line, albeit with subtly changing gradient. Therefore, the deposition rate was calculated from the time-derivative of measured thickness. The rate is much more informative of the Cs processes occuring inside the ion source and vacuum vessel, giving a clear indication of whether the Cs flux has changed. Alterations to the VESPA ion source operating parameters are highlighted in Fig. 8.4 over a two week period. There are several effects of note; for example the QCMs were extremely sensitive to changes in their cooling water temperature, but after an initial change they settled back down again. Therefore, the measurements were stable and insensitive to the absolute cooling temperature, as long as that temperature remained constant. This factor is revisited in Section 8.2.3, with important consequences.

The Cs oven temperature was changed in large, discrete steps and the deposition rate allowed to stabilise. It can be seen that the change in Cs flux was distinguished easily by the QCMs, with the deposition rate taking approximately two hours to ramp up or down to the new level. The cause of the long delay is highly interesting. When a new temperature was entered into the control system, the oven heaters took

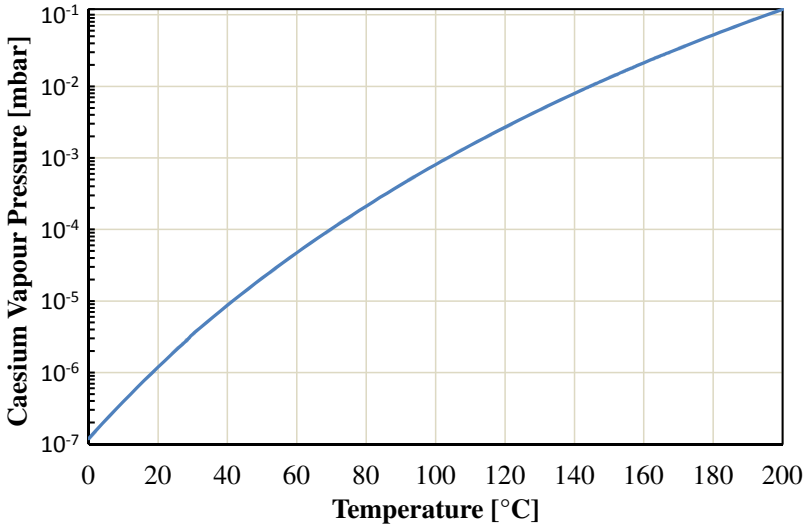

Figure 8.5: Caesium vapour pressure as a function of temperature.

approximately ten seconds to respond and stabilise. The ion source plasma responded to changes in Cs flow on timescales of one to twenty minutes, depending on how large the alteration. This was how long the Cs partial pressure took to stabilise inside the plasma and on the cathode surfaces, so was also presumably how long it took for Cs to escape the outlet aperture. The additional hour-long response by the QCMs was likely the time required for the Cs to re-distribute around the vacuum vessel. This implies that the QCMs did not simply measure the Cs particles flowing directly out of the ion source, as this would happen on much quicker timescales. Instead, Cs continually adsorbed onto and desorbed from the vessel interior, creating a background residual gas pressure surrounding the QCMs. This continual indirect background Cs flux was what the QCMs detected. Assuming the vessel and QCM temperatures were constant (meaning a steady wall and sensor desorption rate), changes in the detected deposition thickness hence came from the change of Cs vapour inside – and thus Cs flux escaping – the ion source. The vapour pressure, p of a metallic element, measured in Pascals, is given by [143]

$$\log(p) = 5.006 + A + BT^{-1} + C\log T + DT^{-3} \tag{8.2.2}$$

where T is the temperature in Kelvin and A, B, C, D are coefficients specific to each element. For solid caesium, $A = 4.711$ and $B = -3999$, whereas liquid caesium has $A = 4.165$ and $B = -3830$. $C = D = 0$ for both solid and liquid caesium. The vapour pressure of Cs is plotted using practical units in Fig. 8.5. It can be seen that the background pressure would decrease by an order of magnitude if the vacuum

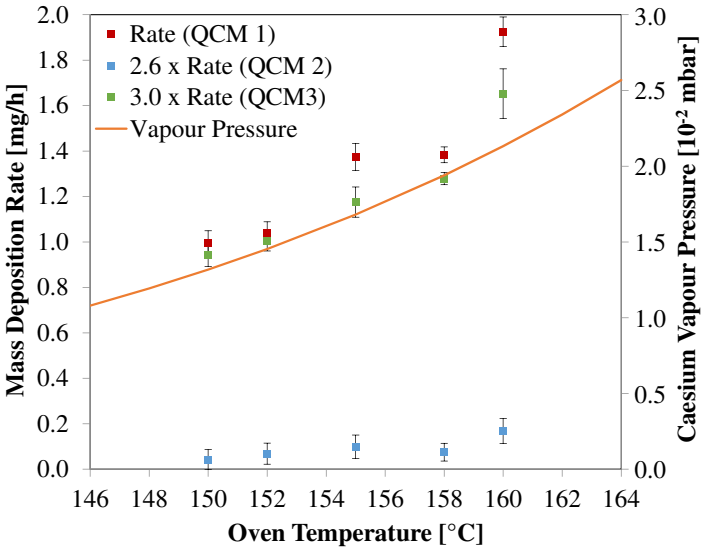

Figure 8.6: Caesium deposition rate on three quartz crystal microbalance sensors as a function of the ion source oven temperature. The caesium vapour pressure calculated using Eq. 8.2.2 is also shown to guide the eye.

vessel walls were cooled from room temperature down to around 0 °C. Considering how sensitive the QCMs were to cooling temperature variations in Fig. 8.4, this would reduce significantly the amount of Cs depositing on unwanted locations such as high voltage electrodes and the RFQ downstream of the ion source vacuum vessel. Therefore a future project could be to build a cold trap into the vessel walls to accumulate caesium. This could be located far from the ion source and shaped like a cup so that condensed Cs would not melt and run off the trap upon letting up the vacuum to remove the ion source.

Based on the analysis of background Cs vapour pressure, it can be assumed that, on average far from the ion source, the flux was uniform around a hemisphere centred on the ion source. This is as opposed to the flux being concentrated on axis and following a cosine-like distribution away from the central axis. This being the case, the deposition rates measured by the sensors should follow the inverse square law:

$$D_{QCM1}\, R_{QCM1}^2 = D_{QCM2}\, R_{QCM2}^2 = D_{QCM3}\, R_{QCM3}^2 \tag{8.2.3}$$

where D_{QCM} is the deposition rate on each QCM sensor (1, 2 or 3) and R_{QCM} is the total distance between the ion source and a sensor. Calculating the total distance from the values in Table 8.1, it can be calculated that $D_{QCM1} = 2.6 D_{QCM2} = 3.0 D_{QCM3}$. Furthermore, the density ρ of caesium is 1.93 kg/m^3 and the exposed quartz crystal radius r was measured to be 4 mm, so the mass deposition rate $\dot{m}_{QCM}$ on a sensor

was simply $\dot{m}_{QCM} = \rho\pi r^2 D_{QCM}$. Assuming uniform mass deposition on a hemisphere centred on the ion source, the average mass deposition rate on the vessel interior $\dot{m}$ may then be calculated through the ratio of sensor and hemisphere surface areas:

$$\dot{m} = \frac{2\pi R_{QCM}^2}{\pi r^2}\dot{m}_{QCM} = 2\pi R_{QCM}^2\ \rho\ D_{QCM}, \tag{8.2.4}$$

where D_{QCM} has the geometric scale factor calculated in Eq. 8.2.3. Using these scaling factors, the dependence on caesium mass deposition rate with oven temperature is shown in Fig. 8.6. It can be seen that the scaling of QCM sensor 3 was in excellent agreement with the assumption of a uniform Cs pressure distribution in the vacuum vessel, whereas QCM 2 did not scale correctly. The reason for this was likely the post-extraction 'spider' assembly shadowing QCM 2 from the majority of the Cs flux. It can also be seen that the deposition rate closely followed the expected Cs vapour pressure calculated from Eq. 8.2.2. The exception was the measurement at 160 °C; despite being given the same >20 hour settling time as the others, that particular measurement still fluctuated somewhat. This demonstrated that the QCM detectors were not suitable for quick, instantaneous measurements of ion source performance, but did give valuable insight of long-term trends.

In operation on ISIS, the ion source requires gradually higher oven temperatures throughout its life as the Cs is used up. Long-term experience with the ion source has shown that, on average, a 5 g ampoule of Cs is consumed in 50 days. This equates to approximately 0.1 g per day, or 4 mg/h. The Cs deposition rates shown in Fig. 8.6 agree with this estimate to within 50%, which is quite reasonable considering the assumption made of uniform distribution over the hemisphere. The discrepancy likely comes from the fact that as the caesium is depleted, the oven temperature is increased to 170-180 °C. Extrapolating from the data in Fig. 8.6, this would indeed give a mass deposition rate of around 4 mg/h. Also, a large amount of Cs impacted directly on the immediate vicinity of the ion source, for example the extraction, einzel and ground electrodes; remained inside the ion source itself, or was removed by the vacuum pumps. Therefore, taking all these effects into account, the agreement between measured Cs consumption rates using the QCMs and evidence from spent ampoules is impressive. Use of the QCMs will continue in future measurement campaigns over several weeks' operation. These measurements will determine whether the deposition rate decreases as the Cs supply diminishes; or whether the rate *increases* due to the need for higher oven temperatures as supply diminishes.

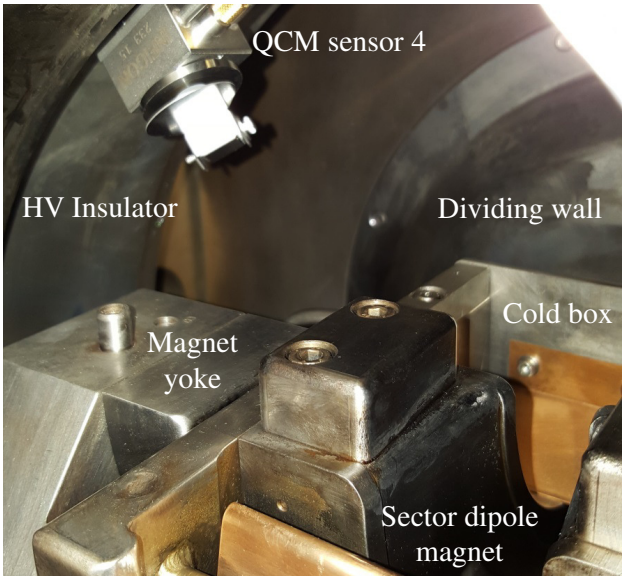

Figure 8.7: Photo of QCM sensor 4 installed inside the ion source volume of the ISDR, such that it measured caesium escaping the top of the cold box.

8.2.3 Measurements With a Caesium Trap

The QCMs were also used to measure the caesium deposition rate on the Ion Source Development Rig (ISDR) [144]. The ISDR is a replica of the ISIS operational ion source, including a cold box to trap Cs vapour. Therefore it provided a useful check to quantify the effect of removing the Cs trap on the VESPA. The ISDR incorporates differential vacuum pumping, whereby the immediate volume surrounding the ion source is evacuated by one pump, whilst the remaining downstream volume in the vacuum vessel is evacuated with a second pump. The two volumes are separated with an internal dividing wall: only the cold box output orifice connects the two volumes. A beam current transformer toroid is mounted on the dividing wall. Differential pumping removes hydrogen efficiently in operation, ensuring a good vacuum is achieved downstream of the ion source. The dividing wall made caesium measurements with the QCMs more difficult to arrange, since the majority of Cs would be contained within the ion source volume of the vessel. Sensors 1, 2 & 3 were installed in the downstream volume: sensor 1 was located by the toroid and pointed into the cold box orifice; sensor 2 was on the side wall of the vessel; sensor 3 was on axis by the vessel's end flange. Sensor 4 was installed inside the ion source volume of the vacuum vessel, positioned next to the HV insulator such that it could view inside the top of the cold box, as shown in Fig. 8.7. By comparing sensors 1 and 4, the amount of Cs flux escaping the cold box from two different directions could be measured.

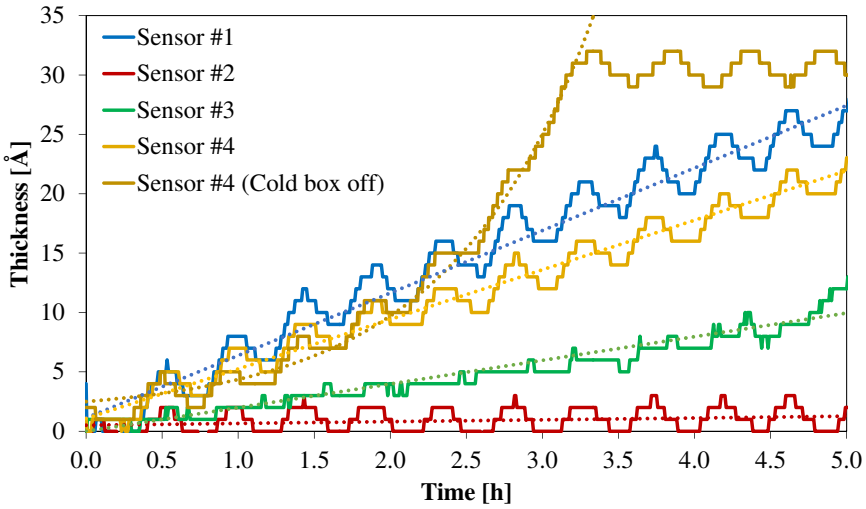

Figure 8.8: Caesium deposition thickness measured on the ISDR with and without the use of a cold box to trap the caesium.

The four QCM sensors were cooled with the ISDR water chiller in the same manner as for the VESPA measurements. Unfortunately, the convoluted pipework required for sensor 4 affected the temperature stability. This resulted in much more ripple on the measured thickness signals from all four QCMs, as can be seen in Fig. 8.8. Although the measured thickness increased with the same overall linear trends seen on the VESPA in Fig. 8.4, taking a time derivative to calculate the deposition rates was more difficult with such noisy data. Equally, because of limited measurement time available on the ISDR, the accumulation of long-term statistics over several days – which would have helped reduce errors in the rate calculations – could not be achieved. Note, for example, that the vertical thickness scale in Fig. 8.8 is measured in Å, whereas measurements over several weeks in Fig. 8.4 allowed a kÅ scale, further reducing noise. Nevertheless, best-fit lines to the data in Fig. 8.8 allowed estimates of deposition rate. With these estimates, meaningful comparisons between the VESPA and ISDR are summarised in Table 8.2. As discussed in Section 8.2.1, the direct line-of-sight view into the VESPA ion source using sensor 4 positioned by the toroid

Table 8.2: Caesium flux comparison between VESPA and ISDR.

Location	**VESPA**	**ISDR**
Toroid	120 Å/h	5.3 Å/h
HV Insulator	10.4 Å/h	4.2 Å/h
Vessel mid-wall	0.2 Å/h	0.2 Å/h
Vessel end-wall	3.6 Å/h	2.0 Å/h

led to an order of magnitude higher signal, which is why it was removed. Compared to the measurement at the toroid on the ISDR, this shows just how effective the cold box and 90° bending magnet are at trapping Cs vapour. However, elsewhere in the vessel, the results are surprisingly similar, with less than a factor of two increase in Cs flux on the vessel walls far from the ion source without the use of a cold box. Indeed, even considering the cold box itself, almost the same amount of Cs escaped out the top as from its output orifice.

For completeness, Fig. 8.8 also shows the effect of operating the ISDR with the cold box switched off. In this case, neutral Cs atoms would still travel on ballistic trajectories vertically down from the ion source aperture and be intercepted at the bottom of the cold box. However the Cs would not then condense onto the uncooled box and would instead be free to reflect off. Additionally, recall that the cold box provides parasitic cooling of the puller electrode (see Section 6.3); with the cooling switched off, the puller and cold box increased quickly in temperature, meaning any Cs already condensed on the cold box evaporated off. This can be seen by the exponential increase of Cs flux measured escaping the cold box in Fig. 8.8. When it became apparent the temperatures and extraction current were reaching dangerous levels, the cold box refrigerator was switched on. However it was already too hot for the refrigerant circuit to cope with, so the entire ion source had to be turned off and allowed to cooled down. This point can be seen at approximately 3.3 hours into the dataset.

8.3 Discussion

The long-term stability of an ion source is just as important as its headline beam current and emittance parameters. Therefore a year-long trial of VESPA operation is underway to determine whether it is suitable for installation on ISIS. In the meantime, measurements of the caesium flux using QCM sensors quantified the effect of removing the cold box and replacing it with a more efficient beam transport system. Measurements showed an order of magnitude higher Cs flux in the immediate vicinity of the ion source electrodes, but very similar Cs deposition rates elsewhere in the vacuum vessel. Therefore it may be argued that the primary benefit of the cold box is reducing the Cs flux onto the HV electrodes downstream of the ion source extractor. This was indeed its purpose when the Penning ion source was first installed on ISIS, because the H^- used to be accelerated to 665 keV by a Cockcroft-Walton voltage

multiplier stack. Emitting a high Cs flux onto the 665 kV electrodes would have been catastrophic for the voltage holding. Since the Cockcroft-Walton has been replaced by an RFQ, the required withstand voltage near the ion source is only 35 kV, which is much easier to maintain, despite a higher Cs flux. The measured vessel-wall deposition rates in Table 8.2 were very similar with and without the cold box. This means the Cs vapour making its way out of the vessel and into the downstream LEBT and RFQ would be comparable to the present case, meaning the VESPA is a suitable candidate for installation on ISIS.

The measured Cs deposition rates were very temperature sensitive, as seen by the exponential increase when the cold box was allowed to heat up, and when the QCM water cooling was varied. In addition, the Cs distribution was shown to be uniform around the vessel, indicating that there was a continual redistribution of Cs around the vessel, leading to a background vapour pressure. Therefore, a suitable extension to the project would be to install a cold trap somewhere inside the vacuum vessel, far from the ion beam transport system. This cold trap could be powered by a Peltier [145] cooler, which is much simpler with no moving parts or possible fluid leak paths compared to the present refrigerant circuit of the ISIS cold box. The Peltier should be firmly attached to the vessel wall such that its 'hot side' would conduct heat away to the laboratory, whilst its 'cold side' would maintain a temperature around 0 °C. Caesium particles moving continually around the vacuum vessel would eventually impact the cold trap and condense. Therefore the background Cs vapour pressure would slowly reduce over time, and higher vessel cleanliness would be achieved. The Peltier should be inside a cup- or bowl-shaped piece of aluminium so that Cs condensed inside would not melt and run off when the vacuum is let up. Using a remotely-located cold trap would give all the benefits of the existing cold box on ISIS, but would not interfere with the beam transport system.

Chapter 9

Conclusions and Outlook

The work presented in this thesis covers a wide range of different topics necessary for the successful design, construction, commissioning and operation of a modern high power, efficient H^- ion source. As such, extensive discussions were presented on the mechanical and electrical design; plasma and beam commissioning strategy; plasma optical spectroscopy measurements; particle tracking, electrostatic and thermal simulations; beam extraction and transport measurements, and caesium flux measurements. Primarily, though, this work demonstrates that a Penning H^- ion source can be operated in a completely different regime, whereby beam focussing is accomplished using an einzel lens rather than a combined-function sector dipole magnet. Moreover, the einzel lens demonstrated in this thesis is the first one ever used with an elliptical aperture, giving different focussing strengths in both transverse planes.

The practical aspects of constructing a new ion source test area were discussed, with emphasis on a new test Vessel for Extraction and Source Plasma Analyses (VESPA). Collating all of these practical considerations into one body of work provides a useful reference for any researcher considering building their own ion source test stand. The work includes the successful design and construction of a new temperature monitoring and control crate. This crate was simpler, less expensive, more easily maintained, more rugged and had greater functionality than the existing crates used on ISIS. The importance of a compact yet thoughtfully spaced-out working area and vacuum vessel design were emphasised, as well as the need for high vacuum pumping speeds. During plasma commissioning, a high frequency oscilloscope was used to investigate the possible causes of arc noise. It was discovered that low-frequency overtones were suppressed for higher arc currents and for higher caesium flow rates. Similarly, the bandwidth of high frequency components was reduced. In general, the noise reduction was caused by an increased plasma density, and for the first time this

work begins to explain why. The low-frequency ringing at very low arc currents was caused by resonant traversal of caesium atoms between the cathode jaws. At higher plasma densities, more collisions occurred so the caesium energy distribution smeared out. This negated the resonant effect of a large amount of caesium particles sputtered at a certain energy making their way across the plasma to the opposite cathode unimpeded, arriving there at the same time. Increasing the hydrogen or caesium flow rates, or reducing the magnetic field strength had the same effect of reducing the noise for the same reason. Based also on frequency calculations, it seems reasonable to conclude that the low frequency noise issues experienced on the Penning ion source plasma were related generally to the caesium plasma density. Other than the strategies used presently on ISIS to remove arc noise – adjusting the hydrogen and caesium flow rates, or the cathode temperature – these frequency measurements suggest two other methods: (1) The plasma volume could be increased, thus increasing the likelihood of particle collisions which smear out resonant effects. This is the strategy being investigated in parallel with the present VESPA studies, so time will tell if the noise is reduced. (2) If the sputter rate of caesium from the cathode could be reduced, then resonant effects leading to noise would be suppressed. To achieve this, a lower cathode voltage would be needed, meaning less energy would be available for sputtering.

Optical emission spectroscopy measurements were performed for the first time at ISIS. Similar detailed measurements were made at Los Alamos and Novosibirsk on their Penning ion sources, however the use of modern collisional-radiative (CR) plasma models in this thesis allowed a greater understanding of the non-Maxwellian temperature distributions found in such high density plasmas. Argon was injected into the VESPA ion source to make use of the CR models, but it was found to be highly disruptive to the source operation due to enhanced caesium sputtering rates. A fast vacuum pressure measurement system was devised to estimate the pulsed hydrogen pressure profile inside the tiny Penning plasma. Finally, the absolute optical emission intensity was determined using a calibrated measurement system. Combining these three new developments, the first accurate measurements of a Penning ion source plasma were performed. It was found that the electron temperature of 3 eV was fairly independent of arc current; whereas the atomic temperature linearly increased and showed signs of becoming higher than the electron temperature at higher arc currents. Several theories were put forward to explain the unexpectedly high atomic temperature, including plasma turbulence and hydrogen desorption from the

cathode by high energy positive ions. The plasma density was measured to be around 10^{19} m^{-3} and considerations of the Fulcher spectrum showed a high molecular hydrogen dissociation degree of 70%. These values are an order of magnitude higher than in volume-type ion source plasmas, which shows how high a power density the Penning ion source truly has.

The measured plasma parameters were used as inputs to an accurate three-dimensional particle tracking simulation. It was found that the standard 18 kV extraction voltage used on ISIS is sub-optimal and 13 kV would be a better setting for a perveance-matched plasma meniscus. A new post-extraction system was designed to replace the existing dipole magnet inside its 'cold box'. A novel einzel lens with an elliptical aperture was implemented successfully to focus the asymmetric beam in both planes, bringing it to a round profile with low emittance. As well as excellent particle transmission, the system was designed for high reliability by performing electrostatic and thermal simulations, whereby the extraction electrode temperature was controlled with a simple cooling block incorporating boron-nitride ceramic. To power the einzel lens, a robust high-voltage circuit was manufactured which incorporated a high power bleed resistor to ensure voltage stability and a spark gap to protect the system.

H^- beam measurements showed that the ion source produced 80-90 mA of beam current at standard settings, validating the hypothesis that significant beam-loss occurs on the ISIS dipole magnet, since only 50-55 mA is measured after the cold box. It was shown that if perfect beam transport could be achieved all the way from the ion source to the ISIS synchrotron, then the ion source arc and extraction power supplies could operate at half their normal settings and still deliver sufficient beam. The elliptical einzel lens system transported 80 mA of beam current successfully with minimal beam-loss and a normalised RMS emittance of 0.2 π mm mrad in both planes. It was a flexible system which could deliver a wide variety of beam phase-space orientations into the following accelerator component. A chopping system was also incorporated which achieved a rise time of 24 ns to 6 kV and which deflected the beam successfully by over 120 mrad at any pulse repetition rate. The elliptical einzel lens is an important addition to the arsenal of beam focussing options, which would be useful for the control of other types of asymmetric beam. For example, a common complaint with an ECR ion source is that its hexapole magnetic cusp field confines the plasma in such a way that the extracted beam often has a triform or 'Mercedes logo' profile. As

such, there is a vertical asymmetry in real-space, which could be corrected using an elliptical einzel lens.

The long term stability of the VESPA system was considered, especially the impact of removing the caesium-trapping cold box. A suite of quartz crystal microbalances (QCMs) was used to measure the caesium flux at various locations inside the vacuum vessel. It was found that far from the ion source, a uniform distribution of caesium was deposited on the vessel walls, which followed a simple inverse-square distance relationship. Moreover, although the deposition rate was high on the accelerating electrodes, there was little difference downstream whether a cold box was used or not. Therefore no ill effects on the low energy beam transport (LEBT) or radio frequency quadrupole (RFQ) can be expected with beam extracted on axis directly from the ion source. Looking at the broader context of H^- ion source R&D, this thesis has added to the recent experience with Fermilab's magnetron, by including a Penning source to the roster of high power, high duty-factor surface-plasma ion sources operating with direct beam extraction. The addition of a non-intrusive QCM measurement of caesium contamination around the nearby vacuum environment is of great interest throughout the international community and would be a suitable diagnostic tool for any ion source utilising caesium. For example, the H^- ion sources to be used at ITER and other fusion devices will have to operate long-term with megavolt-level voltage-holding capability. The ability to quantify caesium usage and how it affects spark rates will be critical for this application.

In summary, this thesis has shown that a high power Penning H^- ion source can be operated efficiently using a novel elliptical einzel lens and no caesium trap. A wide variety of new power supplies, control systems and diagnostics was also demonstrated which overhaul and modernise this venerable yet powerful ion source; ensuring it will continue to provide quality H^- ion beams for ISIS operations for many years to come.

Bibliography

[1] Helmut Wiedemann. *Particle Accelerator Physics*. Springer, Cham, Switzerland, 4th edition, 2015.

[2] Robert W. Hamm and Marianne E. Hamm. *Industrial Accelerators and their Applications*. World Scientific Publishing Co. Pte. Ltd, London, United Kingdom, 2012.

[3] S. R. Lawrie and D. C. Faircloth. Design study of a test vessel to investigate the ISIS H^- penning ion source plasma. *AIP Conference Proceedings*, 1515:440–447, 2013.

[4] S. R. Lawrie, D. C. Faircloth, A. P. Letchford, M. Perkins, M. Whitehead, and T. Wood. Installing the VESPA H^- ion source test stand at RAL. In *Proceedings of the International Particle Accelerator Conference*, Dresden, Germany, 2014.

[5] S. R. Lawrie, D. C. Faircloth, A. P. Letchford, M. Perkins, M. Whitehead, T. Wood, C. Gabor, and J. Back. Development of the front end test stand and vessel for extraction and source plasma analyses negative hydrogen ion sources at the Rutherford Appleton Laboratory. *Review of Scientific Instruments*, 85(02B127), 2014.

[6] S. R. Lawrie, D. C. Faircloth, A. P. Letchford, M. Whitehead, and T. Wood. Detailed beam and plasma measurements on the vessel for extraction and source plasma analyses (VESPA) penning H^- ion source. *Review of Scientific Instruments*, 87(02B122), 2016.

[7] S. R. Lawrie, D. C. Faircloth, A. P. Letchford, M. Perkins, M. Whitehead, and T. Wood. First beam measurements on the vessel for extraction and source plasma analyses (VESPA) at the Rutherford Appleton laboratory (RAL). *AIP Conference Proceedings*, 1655(030011), 2015.

[8] National Electrostatics Corp. www.pelletron.com, October 2014.

[9] H. von Jagwitz-Biegnitz, D. Faircloth, R. G. Selway, P. Beasley, S. Gomann-Levchuk, and O. Heid. System integration of the demonstration Siemens electrostatic accelerator. In *Proceedings of the International Particle Accelerator Conference*, Dresden, Germany, 2014.

[10] R. Hemsworth, H. Decamps, J. Graceffa, B. Schunke, M. Tanaka, M. Dremel, A. Tanga, H.P.L. De Esch, F. Geli, J. Milnes, T. Inoue, D. Marcuzzi, P. Sonato, and P. Zaccaria. Status of the ITER heating neutral beam system. *Nuclear Fusion*, 49(045006), 2009.

[11] P. J. Bryant and K. Johnsen. *The Principles of Circular Accelerators and Storage Rings*. Cambridge University Press, Cambridge, United Kingdom, 1993.

[12] L. Arnaudon *et al.* Linac4 technical design report. Technical Report AB-2006-84 ABP/RF, CERN, 2006.

[13] S. Holmes, P. Derwent, V. Lebedev, S. Mishra, D. Mitchell, and V. P. Yakovlev. PIP-II status and strategy. In *Proceedings of the International Particle Accelerator Conference*, Richmond, USA, 2015.

[14] Science and Technology Facilities Council. Neutron scattering: Materials research for modern life. ISIS Internal Brochure, 2012.

[15] Institut Laue-Langevin. ILL Annual Report 2015, 2015.

[16] F. P. An et. al. A side-by-side comparison of Daya Bay antineutrino detectors. *Nuclear Instruments and Methods inPhysics Research A*, 685:78–97, 2012.

[17] M. S. Onegin. Investigation of the possibilities of heavy actinide isotopes production in highflux reactor PIK. In *Proceedings of the Super Heavy Elements Symposium*, Texas, USA, 2015.

[18] H. Nifenecker, O. Meplan, and S. David. *Accelerator Driven Subcritical Reactors*. CRC Press, 2003.

[19] M. G. White, F. C. Schoemaker, and G. K. O'Neill. A 3 Bev high intensity proton-synchrotron. In *CERN Symposium on High Energy Accelerators and the Physics of Mesons*, pages 525–529, Geneva, Switzerland, 1956.

[20] S. West, J. W. Gray, M. G. Glover, L. A. van Lieshout, K. Papp, and K. Pointner. Replacement of the ISIS White-circuit choke. In *Proceedings of the European Particle Accelerator Conference*, Genoa, Italy, 2008.

[21] Jack Bittencourt. *Fundamentals of Plasma Physics*. Springer Science + Business Media, LLC, 3rd edition, 2004.

[22] H. G. Dehmelt. Stored-ion spectroscopy. *Advances in Laser Spectroscopy*, A:153–187, 1983.

[23] H. Tawara, Y. Itikawa, H. Nishimura, and M. Yoshino. Cross sections and related data for electron collisions with hydrogen molecules and molecular ions. *J. Phys. Chem. Ref. Data*, 19(3):617–636, 1990.

[24] R. J. Goldston and P. H. Rutherford. *Introduction to Plasma Physics*. Taylor & Francis, New York, New York, 1995.

[25] C. D. Child. Discharge from hot CaO. *Physical Review (Series 1)*, 32(492), 1911.

[26] I. Langmuir. The effect of space charge and residual gases on thermionic currents in high vacuum. *Physical Review*, 2:450–486, 1913.

[27] R. Keller A. P. Letchford R. W. Thomae M. P. Stockli, R. F. Welton and J. W. G. Thomason. Accurate estimation of the RMS emittance from single current amplifier data. *AIP Conference Proceedings*, 639, 2002.

[28] R. Geller. *Electron Cyclotron Resonance Ion Sources and ECR Plasmas*. Taylor & Francis, New York, New York, 1995.

[29] B. deB. Darwent. *Bond Dissociation Energies in Simple Molecules*. US National Bureau of Standards, 1970.

[30] T. Anderson, H. K. Haugen, and H. Hotop. Binding energies in atomic negative ions. *Journal of Physics and Chemistry Reference Data*, 28(1511), 1999.

[31] M. Bacal and M. Wada. Negative hydrogen ion production mechanisms. *Applied Physics Reviews*, 2(021305), 2015.

[32] B. Rasser, J. N. M. van Wunnik, and J. Los. Theoretical models of the negative ionization of hydrogen on clean tungsten, cesiated tungsten and cesium surface at low energies. *Surface Science*, 118:697–710, 1982.

[33] H. B. Michaelson. The work function of the elements and its periodicity. *Journal of Applied Physics*, 48(11):4125–4131, 1977.

[34] S. H. Chou, J. Voss, I. Bargatin, A. Vojvodic, R. T. Howe, and F. Abild-Pedersen. Orbital-overlap model for minimal work functions of cesiated metal surfaces. *Journal of Physics: Condensed Matter*, 24(44):5007–5015, 2012.

[35] R. G. Wilson. Electron and ion emission from polycrystalline surfaces of Nb, Mo, Ta, W, Re, Os and Ir in cesium vapor. *Journal of Applied Physics*, 37(11):4729–4733, 1966.

[36] D. A. Gorodetsky, Yu. P. Melnik, V. A. Usenko, A. A. Yasko, and V. I. Yarigin. Cesium on molybdenum(110). *Surface Science*, 315:51–61, 1994.

[37] R. Friedl and U. Fantz. Temperature dependence of the work function of caesiated materials under ion source conditions. *AIP Conference Proceedings*, 1655(020004).

[38] Yu. I. Belchenko, G. I. Dimov, and V. G. Dudnikov. A powerful injector of neutrals with a surface-plasma source of negative ions. *Nuclear Fusion*, 14(1), 1974.

[39] O. Tarvainen, T. Kalvas, J. Komppula, H. Koivisto, E. Geros, J. Stelzer, G. Rouleau, K. F. Johnson, and J. Carmichael. Effect of ion escape velocity and conversion surface material on H^- production. *AIP Conference Proceedings*, 1390:113–122.

[40] J. S. Vogel. H^- formation by neutral resonant ionisation of H(n=2) atoms. *AIP Conference Proceedings*, 1655(020015), 2015.

[41] U. Kurutz and U. Fantz. Investigations on caesium-free alternatives for H^- formation at ion source relevant parameters. *AIP Conference Proceedings*, 1655(020005), 2015.

[42] J. Peters. Negative ion sources for high energy accelerators. *Review of Scientific Instruments*, 71(2):1069–1074.

[43] D. P. Moehs, J. Peters, and J. Sherman. Negative ion sources for accelerators. *IEEE Transactions on Plasma Science*, 33(6), 2005.

[44] Dehnel Particle Accelerator Components and Engineering Inc. www.d-pace.com/products_hionfilament.html, March 2015.

[45] T. Kuo, D. Yuan, K. Jayamanna, M. McDonald, R. Baartman, W. Z. Gelbart, N. Stevenson, P. Schmor, and G. Dutto. Further development for the TRIUMF H^-/D^- multicusp source. *Review of Scientific Instruments*, 69:959–961, 1998.

[46] T. Kalvas, O. Tarvainen, J. Komppula, H. Koivisto, J. Tuunanen, D. Potkins, T. Stewart, and M. P. Dehnel. A CW radiofrequency ion source for production of negative hydrogen ion beams for cyclotrons. *AIP Conference Proceedings*, 1655(030015), 2015.

[47] R. Gobin, K. Benmeziane, O. Delferrière, R. Ferdinand, F. Harrault, and J. D. Sherman. The CAE/Saclay 2.45 GHz microwave ion source for H^- ion production. *AIP Conference Proceedings*, 639:177–183, 2002.

[48] I. S. Hong, H. D. Jung, Y. S. Park, and Y. S. Hwang. Status of an RF negative hydrogen ion source using transformer coupled plasma source. *AIP Conference Proceedings*, 639:61–66, 2002.

[49] R. F. Welton, V. G. Dudnikov, K. R. Gawne, B. X. Han, S. N. Murray, T. R. Pennisi, R. T. Roseberry, M. Santana, M. P. Stockli, and M. W. Turvey. H^- radio frequency source development at the Spallation Neutron Source. *Review of Scientific Instruments*, 83(02B725), 2012.

[50] M. Wada, T. Kasuya, T. Kenmotsu, S. Maeno, T. Nishida, K. Shinto, and H. Yamaoka. Extraction of negative hydrogen ions from a compact 14 GHz microwave ion source. *Review of Scientific Instruments*, 83(02B716), 2012.

[51] J. Zacks, I. Turner, I. Day, K. Flinders, B. Crowley, and R. McAdams. Update on developments at SNIF. *AIP Conference Proceedings*, 1655(030012), 2015.

[52] S. X. Peng, T. Zhang, H. T. Ren, A. L. Zhang, Y. Xu, J. F. Zhang, Z. Y. Guo, and J. E. Chen. Duty factor variation possibility from 1% to 100% with PKU microwave driven Cs-free volume H^- sources. *Review of Scientific Instruments*, 87(02B125), 2016.

[53] J. Peters. The new DESY RF-driven multicusp ion source. *AIP Conference Proceedings*, 1097:171–180, 2009.

[54] J. Lettry, D. Aguglia, J. Alessi, P. Andersson, S. Bertolo, S. Briefi, A. Butterworth, Y. Coutron, A. Dallocchio, N. David, E. Chaudet, D. Faircloth, U. Fantz, D. A. Fink, M. Garlasche, A. Grudiev, R. Guida, J. Hansen,

M. Haase, A. Hatayama, A. Jones, I. Koszar, J.-B. Lallement, A. M. Lombardi, C. Machado, C. Mastrostefano, S. Mathot, S. Mattei, P. Moyret, D. Nisbet, K. Nishida, M. ONeil, M. Paoluzzi, R. Scrivens, T. Shibata, D. Steyaert, N. Thaus, and G. Voulgarakis. Linac4 H^- ion sources. *Review of Scientific Instruments*, 87(02B139), 2016.

[55] M. P. Stockli, B. Han, S. N. Murray, T. R. Pennisi, C. Piller, M. Santana, and R. Welton. Recent performance of and plasma outage studies with the SNS H^- source. *Review of Scientific Instruments*, 87(02B140), 2016.

[56] H. Oguri, K. Ohkoshi, K. Ikegami, A. Takagi, H. Asano, A. Ueno, and T. Shibata. Status of the RF-driven H^- ion source for J-PARC linac. *Review of Scientific Instruments*, 87(02B138), 2016.

[57] R. Keller, O. Tarvainen, E. Chacon-Golcher, E. G. Geros, K. F. Johnson, G. Rouleau, J. E. Stelzer, and T. J. Zaugg. H^- ion source development for the LANSCE accelerator systems. *AIP Conference Proceedings*, 1097:161–170.

[58] J. G. Alessi. Performance of the magnetron H^- ion source on the BNL 200 Mev linac. *AIP Conference Proceedings*, 642:279–286, 2002.

[59] D. S. Bollinger, J. Lackey, J. Larson, and K. Triplett. A new solid state extractor pulser for the FNAL magnetron ion source. *Review of Scientific Instruments*, 87(02B902), 2016.

[60] J. W. G. Thomason and R. Sidlow. ISIS ion source operational experience. In *Proceedings of the European Particle Accelerator Conference*, Vienna, Austria, 2000.

[61] P. W. Allison. A direct extraction H^- ion source. *IEEE Transactions on Nuclear Science*, NS-24(3):1594–1596, 1977.

[62] V. Dudnikov. Surface-plasma source of negative ions with a penning discharge. In *Proceedings of the 4th All-Union Conference on Charged Particle Accelerators*, Moscow, Russia, 1974.

[63] I. Bustinduy, D. Fernandez, D. de Cos, J. Feuchtwanger, S. Lawrie, D. Faircloth, C. Plostinar, A. Letchford, F. J. Bermejo, V. Etxebarria, J. Portilla, J. Jugo, J. Lucas, S. Jolly, M. Eguiraun, J. Alonso, R. Enparantza, and M. Larranaga.

First simulation tests for the Bilbao accelerator ion source test stand. In *Proceedings of the International Particle Accelerator Conference*, Kyoto, Japan, 2010.

[64] S. Liu, T. Huang, H. Ouyang, F. Zhao, Y. Xiao, Y. Lv, X. Cao, K. Xue, J. Zhang, T. Xu, F. Li, Y Lu, G. Li, L. Yang, and Y. Li. Status of the CSNS H^- ion source. *Chinese Physics C*, 39(5), 2015.

[65] D. C. Faircloth, M. O. Whitehead, T. Wood, A. P. Letchford, and M. E. Westall. Multi-beamlet study of beam transport in the ISIS H^- ion source analysing magnet. In *Proceedings of the European Particle Accelerator Conference*, Genoa, Italy, 2008.

[66] S. R. Lawrie, D. C. Faircloth, A. P. Letchford, J. K. Pozimski, M. Westall, M. O. Whitehead, and T. Wood. Modifications to the analysing magnet in the ISIS Penning ion source. In *Proceedings of the European Particle Accelerator Conference*, Genoa, Italy, 2008.

[67] S. R. Lawrie, D. C. Faircloth, A. P. Letchford, M. Westall, M. O. Whitehead, T. Wood, and J. Pozimski. Redesign of the analysing magnet in the ISIS H^- Penning ion source. *AIP Conference Proceedings*, 1097:253–262, 2009.

[68] D. S. Bollinger. Installation and commissioning of the new Fermi national accelerator laboratory H^- magnetron. *Review of Scientific Instruments*, 85(02B121), 2014.

[69] Saudi Basic Industries Corporation (Sabic). www.sabic-ip.com, June 2017.

[70] Quadrant Group. www.quadrantplastics.com, June 2017.

[71] D. C. Faircloth, R. Sidlow, M. O. Whitehead, and T. Wood. Separating the Penning and analyzing fields in the ISIS H^- ion source. In *Proceedings of the Particle Accelerator Conference*, Knoxville, USA, 2013.

[72] S. K. Mukherjee, D. Cheng, M. A. Leitner, K. N. Leung, P. A. Luft, R. A. Gough, R. Keller, and M. D. Williams. Mechanical design of the prototype H^- ion source for the Spallation Neutron Source. In *Proceedings of the Particle Accelerator Conference*, New York, USA, 1999.

[73] J. D. Sherman, W. B. Ingalls, G. Rouleau, , Jr. H. V. Smith, J. Thomason, R. Sidlow, R. Ferdinand, and R. Gobin. Review of scaled penning H^- surface plasma source with slit emitters for high duty factor linacs. In *Proceedings of the European Particle Accelerator Conference*, Paris, France, 2002.

[74] T. Rutter, D. Faircloth, D. Turner, and S. Lawrie. The mechanical design and simulation of a scaled H^- penning ion source. *Review of Scientific Instruments*, 87(02B131), 2015.

[75] D. C. Faircloth, M. Perkins, and S. R. Lawrie. A new long pulse high voltage extraction power supply for FETS. In *Proceedings of the International Particle Accelerator Conference*, Shanghai, China, 2013.

[76] G. E. Derevyankin and V. G. Dudnikov. Production of high brightness H^- beams in surface plasma sources. *AIP Conference Proceedings*, 111(1):376–397, 1984.

[77] V. Dudnikov, D. Bollinger, D. Faircloth, and S. Lawrie. Potential for improving of the compact surface plasma sources. *AIP Conference Proceedings*, 1515:369–378, 2013.

[78] T. J. M. Boyd and J. J. Sanderson. *The Physics of Plasmas*. Cambridge University Press, Cambridge, UK, 2003.

[79] Peter Strehl. *Beam Instrumentation and Diagnostics*. Springer-Verleg, Berlin, Germany, 2006.

[80] I. H. Hutchinson. *Principles of Plasma Diagnostics*. Cambridge University Press, Cambridge, United Kingdom, 2nd edition, 2002.

[81] U. Fantz. Basics of plasma spectroscopy. *Plasma Sources Science and Technology*, 15:S137–S147, 2006.

[82] Hans R. Griem. *Principles of Plasma Spectroscopy*. Cambridge University Press, Cambridge, United Kingdom, 1997.

[83] Hans R. Griem. *Spectral Line Broadening By Plasmas*. Academic Press, Inc, New York, New York, 1974.

[84] F. Mandl. *Quantum Mechanics*. Wiley, Chichester, United Kingdom, 1992.

[85] G. Herzberg. *Atomic Spectra and Atomic Structure.* Dover Publications, Mineola, New York, 1945.

[86] U. Fantz and B. Heger. Spectroscopic diagnostics of the vibrational population in the ground state of H_2 and D_2 molecules. *Plasma Physics of Controlled Fusion*, 40:2023–2032, 1998.

[87] S. Svanberg. *Atomic and Molecular Spectroscopy – Basic Aspects and Practical Applications.* Springer-Verlag, Berlin, Germany, 1992.

[88] D. R. Farley, D. P. Stotler, D. P. Lundberg, and S. A. Cohen. Modeling of hydrogen ground state rotational and vibrational temperatures in kinetic plasmas. *Journal of Quantitative Spectroscopy and Radiative Transfer*, 112(5), 2011.

[89] Z. Gavare, G. Revalde, and A. Skudra. Plasma temperature determination of hydrogen containing high-frequency electrodeless lamps by intensity distribution measurements of hydrogen molecular band. *International Journal of Spectroscopy*, 2010(804506), 2009.

[90] T. Shikama, S. Kado, Y. Kuwahara, K. Kurihara, F. Scotti, and S. Tanaka. Fulcher-α band spectra in mixed hydrogen isotope plasmas. *Plasma and Fusion Research: Regular Articles*, 2(S1045), 2007.

[91] G. Lj. Majstorović. Spectroscopic study of hydrogen rotational, vibrational and translational temperatures in a hollow cathode glow discharge. *Journal of Physics: Conference Series*, 133(012022), 2008.

[92] Joseph Reader, Charles H. Corliss, W. L. Wiese, and G. A. Martin. *Wavelengths and Transition Probabilities for Atoms and Atomic Ions.* National Bureau of Standards, U.S. Government Printing Office, Washington, 1980.

[93] T. Fujimoto. *Plasma Spectroscopy.* Clarendon Press, Oxford, United Kingdom, 2004.

[94] U. Fantz, H. Falter, P. Franzen, D. Wünderlich, M. Berger, A. Lorenz, W. Kraus, P. McNeely, R. Riedl, and E. Speth. Spectroscopy – a powerful diagnostic tool in source development. *Nuclear Fusion*, 46:S297–S306, 2006.

[95] H. P. Summers. *ADAS User Manual.* Glasgow, UK, 2nd edition. http://www.adas.ac.uk/manual.php.

[96] R. Keller and H. V. Smith. Spectroscopic measurements on an H^- ion source discharge. *IEEE Transactions on Nuclear Science*, NS-32(5), 1985.

[97] H. V. Smith, P. Allison, and R. Keller. Spectroscopic investigation of H^- and D^- ion source plasmas. *AIP Conference Proceedings*, 158:181–193, 1987.

[98] H. V. Smith, P. Allison, and J. D. Schneider. Spatial distributions of the emitting species in a Penning surface-plasma source. *Review of Scientific Instruments*, 62(2307):659–661, 1991.

[99] S. Briefi, October 2015. Private Communication.

[100] J. F. Ziegler, M. D. Ziegler, and J. P. Biersack. SRIM – the stopping and range of ions in matter (2010). *Nuclear Instrumenrs and Methods in Physics: B*, 268:1818–1823, 2010.

[101] Yu. I. Belchenko and V. I. Davydenko. Cesium in hydrogen negative ion sources. *Review of Scientific Instruments*, 77(03B702), 2006.

[102] D. C. Faircloth, S. R. Lawrie, A. P. Letchford, C. Gabor, M. Whitehead, T. Wood, and M. Perkins. Latest results from the front end test stand high performance H^- ion source at RAL. *AIP Conference Proceedings*, 1390(205), 2011.

[103] D. C. Faircloth, S. R. Lawrie, H. Pereira Da Costa, and V. Dudnikov. Operational and theoretical temperature considerations in a penning surface plasma source. *AIP Conference Proceedings*, 1655(030013), 2015.

[104] U. Fantz, P. Franzen, W. Kraus, L. Schiesko, C. Wimmer, and D. Wünderlich. Size scaling of negative hydrogen ion sources for fusion. *AIP Conference Proceedings*, 1655(040001), 2015.

[105] Bernhard Wolf. *Handbook of Ion Sources*. CRC Press, Boca Raton, Florida, 2nd edition, 1995.

[106] V. V. Antsiferov, V. V. Beskorovaynyy, A. M. Maximov, P. G. Sova, L. P. Skripal, Yu. I. Belchenko, and G. E. Derevyankin. Spectroscopic study of hydrogen-cesium discharge plasma of surface-plasma ion sources. *AIP Conference Proceedings*, 210:427–449, 1990.

[107] A. Yoshizawa, S. I. Itoh, and K. Itoh. *Plasma and Fluid Turbulence Theory and Modelling*. IOP Publishing, London, United Kingdom, 2003.

[108] D. Wünderlich, S. Dietrich, and U. Fantz. Application of a collisional radiative model to atomic hydrogen for diagnostic purposes. *Journal of Quantitative Spectroscopy and Radiative Transfer*, 110:62–71, 2009.

[109] U. Fantz and D. Wünderlich. A novel diagnostic technique for $H^-(D^-)$ densities in negative hydrogen ion sources. *New Journal of Physics*, 8(301), 2006.

[110] D. C. Faircloth, S. R. Lawrie, A. P. Letchford, C. Gabor, M. Perkins, M. Whitehead, T. Wood, O. Tarvainen, J. Komppula, T. Kalvas, V. Dudnikov, H. Pereira, Z. Izaola, and J. Simkin. Developing the RAL front end test stand to deliver a 60 mA, 50 Hz, 2 ms H^- beam. *AIP Conference Proceedings*, 1515:359–368, 2013.

[111] J. Komppula, August 2015. Private Communication.

[112] J. O. Hirschfelder, C. F. Curtiss, and R. B. Bird. *Molecular Theory of Gases and Liquids*. Wiley, New York, New York, 1964.

[113] R. K. Janev, D. Reiter, and U. Samm. Collision processes in low-temperature hydrogen plasmas. *Berichte des Forschungszentrums*, Institute für Plasmaphysik, Jülich, 2003.

[114] A. Bondi. van der Waals volumes and radii. *Journal of Phyiscal Chemistry*, 68(3), 1964.

[115] K. Behringer and U. Fantz. The influence of opacity on hydrogen excited-state population and applications to low-temperature plasmas. *New Journal of Physics*, 2(23):1–19, 2000.

[116] F. Paschen. Ueber die zum funkenübergang in luft, wasserstoff und kohlensüure bei verschiedenen drucken erforderliche potentialdifferenz. *Annalen der Physik*, 273(5):69–75, 1889.

[117] T. Kalvas, O. Tarvainen, T. Ropponenand O. Steczkiewicz, J. Ärje, and H. Clark. IBSIMU: A three-dimensional simulation software for charged particle optics. *Review of Scientific Instruments*, 81(02B703), 2010.

[118] Cobham Technical Services. www.operafea.com, October 2016.

[119] H. Liebl. *Applied Charged Particle Optics*. Springer, Berlin, Germany, 2008.

[120] Ø. Midttun, T. Kalvas, M. Kronberger, J. Lettry, H. Pereira, and R. Scrivens. A magnetised einzel lens electron dump for the Linac4 H^- ion source. *AIP Conference Proceedings*, 1515:481–490, 2013.

[121] T. Kalvas, O. Tarvainen, J. Komppula, M. Laitinen, T. Sajavaara, H. Koivisto, A. Jokinen, and M. P. Dehnel. Recent negative ion source activity at JYFL. *AIP Conference Proceedings*, 1515:349–358, 2013.

[122] C. Baltador, P. Veltri, P. Agostinetti, G. Chitarin, and G. Serianni. Multi-beamlet investigation of the deflection compensation methods of SPIDER beamlets. *Review of Scientific Instruments*, 87(02B141), 2016.

[123] A. Letchford, September 2016. Private Communication.

[124] A. Descoeudres, T. Ramsvik, S. Calatroni, M. Taborelli, and W. Wuensch. DC breakdown conditioning and breakdown rate of metals and metallic alloys under ultrahigh vacuum. *Physical Review Special Topics - Accelerators and Beams*, 12(032001), 2009.

[125] M. Bacal, M. Sasao, M. Wada, and R. McAdams. Roles of a plasma grid in a negative hydrogen ion source. *AIP Conference Proceedings*, 1655(020001), 2015.

[126] J. Lettry, D. Aguglia, J. Alessi, P. Andersson, S. Bertolo, A. Butterworth, Y. Coutron, A. Dallocchio, N. David, E. Chaudet, D. Fink, J. Gil-Flores, M. Garlasche, A. Grudiev, R. Guida, J. Hansen, M. Haase, A. Hatayama, A. Jones, I. Koszar, T. Lehn, C. Machado, C. Mastrostefano, S. Mathot, S. Mattei, Ø. Midttun, P. Moyret, D. Nisbet, K. Nishida, M. ONeil, M. Paoluzzi, J. Sanchez Alvarez, R. Scrivens, T. Shibata, D. Steyaert, N. Thaus, and A. Zalenski. CERN's Linac4 H^- sources: Status and operational results. *AIP Conference Proceedings*, 1655(030005), 2015.

[127] Yu. I. Belchenko, A. I. Gorbovsky, A. A. Ivanov, S. G. Konstantinov, A. L. Sanin, I. V. Shikhovtsev, and M. A. Tiunov. Multiaperture negative ion source. *AIP Conference Proceedings*, 1515:167–176, 2013.

[128] T. Wood, D. C. Faircloth, S. R. Lawrie, A. P. Letchford, M. O. Whitehead, T. Pike, and M. Perkins. The ISIS pre-injector reconfiguration. *Review of Scientific Instruments*, 87(02B121), 2016.

[129] S. R. Lawrie, D. C. Faircloth, and A. P. Letchford. Improving the ISIS emittance scanner software. In *Proceedings of the European Particle Accelerator Conference*, Genoa, Italy, 2008.

[130] C. Warsop. Low intensity and injection studies on the ISIS synchrotron. In *Proceedings of the European Particle Accelerator Conference*, London, UK, 1994.

[131] R. Miyamoto, B. Cheymol, R. De Prisco, M. Eshraqui, A. Ponton, E. Sargsyan, I. Bustinduy, and H. D. Thomsen. Dynamics of bunches partially chopped with the MEBT chopper in the ESS linac. Technical Report ESS/AD/0054, ESS, 2014.

[132] M. Clarke-Gayther. A two stage fast beam chopper for next generation high power proton drivers. In *Proceedings of the International Particle Accelerator Conference*, San Sebastian, Spain, 2011.

[133] J. B. Lallement, A. Lombardi, E. Sargsyan, M. Hori, and K. Hanke. Measurement strategy for the CERN Linac4 chopper-line. In *Proceedings of the Advanced Beam Dynamics Workshop on High Intensity, High Brightness Hadron Beams*, Tsukuba, Japan, 2004.

[134] A. Aleksandrov and C. Deibele. Experimental study of the SNS MEBT chopper performance. In *Proceedings of the International Particle Accelerator Conference*, Kyoto, Japan, 2010.

[135] T. Kato, M. Ikegami, and S. Wang. Beam study with RF choppers in the MEBT of the J-Parc proton linac. In *Proceedings of the Particle Accelerator Conference*, Oregon, USA, 2003.

[136] G. Abdrashitov, Yu. Belchenko, A. Dranichnikov, A. Ivanov, A. Gorbovsky, V. Kapitonov, V. Kolmogorov, A. Kondakov, S. Konstantinov, A. Sanin, A. Selivanov, P. Selivanov, I. Shikhovtsev, O. Sotnikov, N. Stupishin, M. Tiunov, M. Binderbauer, S. Putvinski, A. Smirnov, and L. Sevier. Negative ion production in the RF multiaperture surface-plasma source. *AIP Conference Proceedings*, 1655(040002), 2015.

[137] H. de Esch, L. Svensson, T. Inoue, M. Taniguchi, N. Umeda, M. Kashiwagi, and G. Fubiani. Results of the SINGAP neutral beam accelerator experiment at JAEA. *AIP Conference Proceedings*, 1097:353–363, 2009.

[138] U. Fantz, B. Heinemann, D.Wünderlich, R. Reidl, W. Kraus, and F. Bonomo. Towards 20 A negative hydrogen ion beams for up to 1 h: Achievements of the ELISE test facility. *Review of Scientific Instruments*, 87(02B307), 2016.

[139] C. Hu, Y. Xie, Y. Xie, S. Liu, Y. Xu, L. Liang, C. Jiang, J. Li, and Z. Liu. Performance of positive ion based high power ion source of EAST neutral beam injector. *Review of Scientific Instruments*, 87(02B301), 2016.

[140] J. Pozimski, P. Savage, S. Alsari, A. Letchford, and D. Faircloth. Investigation of space charge compensation at FETS. In *Proceedings of the International Particle Accelerator Conference*, Shanghai, China, 2013.

[141] G. Sauerbrey. Verwendung von schwingquarzen zur wägung dünner schichten und zur mikrowägung. *Zeitschrift für Physik*, 155:206–222, 1959.

[142] K. K. Kanazawa and J. G. Gordon. Frequency of a quartz microbalance in contact with liquid. *Analytical Chemistry*, 57:1770–1771, 1985.

[143] C. B. Alcock, V. P. Itkin, and M. K. Horrigan. Vapor pressure equations for the metallic elements. *Canadian Metallurgical Quarterly*, 23(3):309–313, 1984.

[144] J. W. G. Thomason, R. Sidlow, and M. O. Whitehead. Performance of the H^- ion source development rig at RAL. In *Proceedings of the European Particle Accelerator Conference*, Paris, France, 2002.

[145] J. C. Peltier. Nouvelles expériences sur la caloricité des courants électriques. *Annales de Chimie et de Physique*, 56:371–386, 1834.